# Declaration

I, Virginia Morris certify that this is my own work and I have not obtained a degree in this University or elsewhere in the basis of this PhD thesis.

---

Virginia Morris BSc

# Acknowledgements

I would first like to say a sincere thank you to my supervisor Prof. Michael Morris for providing me with this great opportunity. I am extremely grateful for his enthusiasm, expertise, support and understanding throughout my PhD and his ability to always approach things from a different angle.

I would like to thank everyone past and present in the materials chemistry group in UCC. To Lab 343 for showing me the ropes, entertaining me throughout my first few years and for producing such a great working environment in which one could do nothing but serious science. To Richard Farrell, Eoin Brennan, Rory Rice, Mark Copley, Jacqui Cusack, Frank Dillion, Barbara Kosmala, Tom Fitzgerald, Louise Barry, Aoife Burke, Aoife Sexton, Kaixue Wang, Nikolay PetKov, Peter Fleming, John Hanrahan, John O'Callaghan, Joe Tobin and Colm O'Mahony for much needed help and support and for many enjoyable days.

I would like to thank all of those in the Chemistry department both technical and administrative, and in particular Chrissie, for always providing me with both glassware and a friendly face.

A very sincere thank you to my colleagues in Analog Devices, without whose support and encouragement, I would not have undertaken this task. In particular to Denis Doyle, Matt Flanagan and Simon Newcomb, for having such belief in my ability, I am forever grateful.

A big thank you to my wonderful friends for many nights out and laughs and who provided great love and support when I needed it most. I'm not going to mention names (that may get me in trouble!) but you know who you are and thanks a million.
A huge thank you to my families, the Morris' and the Kellehers: Mum, Dad, Lavinia,

Gareth, Dearbháile, Ciarán, Micheál and Cheryl for all the love and support over the years. I couldn't have done it without ye and I'm sure I drove ye to distraction with my stressed out phone calls. I owe you all a lot, but thank you all so much for everything. To Mary, John, Linda, Paul, Mags, Norma, Luke, and Niall, thank you for your love and support throughout the years. Mum you can stop praying now for the time being, St. Jude may need a rest! And I can't write this and not give a big mention to my wonderful nieces and nephews Keelin Ruairi, Thomas, Hannah, Olivia, Dara and Erin, ye were always a welcome distraction.

Finally, to my best friend and husband, John for always believing in me and supporting me in everything I do. Without you by my side, I could not have completed this. You are my rock and always will be.

Thank You

**Dedicated to my husband, John**

# Abstract

Cerium dioxide (ceria) nanoparticles have been the subject of intense academic and industrial interest. Ceria has a host of applications but academic interest largely stems from their use in the modern automotive catalyst but it is also of interest because of many other application areas notably as the abrasive in chemical-mechanical planarisation of silicon substrates. Recently, ceria has been the focus of research investigating health effects of nanoparticles. Importantly, the role of non-stoichiometry in ceria nanoparticles is implicated in their biochemistry. Ceria has well understood non-stoichiometry based around the ease of formation of anion vacancies and these can form ordered superstructures based around the fluorite lattice structure exhibited by ceria. The anion vacancies are associated with localised or small polaron states formed by the electrons that remain after oxygen desorption. In simple terms these electrons combine with $Ce^{4+}$ states to form $Ce^{3+}$ states whose larger ionic radii is associated with a lattice expansion compared to stoichiometric $CeO_2$. This is a very simplistic explanation and greater defect chemistry complexity is suggested by more recent work. Various authors have shown that vacancies are mobile and may result in vacancy clustering.

Ceria nanoparticles are of particular interest because of the high activity and surface area of small particulates. The sensitivity of the cerium electronic band structure to environment would suggest that changes in the properties of ceria particles at nanoscale dimensions might be expected. Notably many authors report a lattice expansion with reducing particle size (largely confined to sub-10 nm particles). Most authors assign increased lattice dimensions to the presence of a surface stable $Ce_2O_3$ type layer at low nanoparticle dimensions. However, our understanding of oxide nanoparticles is limited and their full and quantitative characterisation offers serious challenges. In a series of chemical preparations by ourselves we see little evidence of a consistent model emerging to explain lattice parameter changes with

nanoparticle size. Based on these results and a review of the literature it is worthwhile asking if a model of surface enhanced defect concentration is consistent with known cerium/cerium oxide chemistries, whether this is applicable to a range of different synthesis methods and if a more consistent description is possible.

In Chapter one the science of cerium oxide is outlined including the crystal structure, defect chemistry and different oxidation states available. The uses and applications of cerium oxide are also discussed as well as modelling of the lattice parameter and the doping of the ceria lattice.

Chapter two describes both the synthesis techniques and the analytical methods employed to execute this research.

Chapter three focuses on high surface area ceria nano-particles and how these have been prepared using a citrate sol-gel precipitation method. Changes to the particle size have been made by calcining the ceria powders at different temperatures. X-ray diffraction methods were used to determine their lattice parameters. The particles sizes were also assessed using transmission electron microscopy (TEM), scanning electron microscopy (SEM), and BET, and, the lattice parameter was found to decrease with decreasing particle size. The results are discussed in light of the role played by surface tension effects.

Chapter four describes the morphological and structural characterization of crystalline $CeO_2$ nanoparticles prepared by forward and reverse precipitation techniques and compares these by powder x-ray diffraction (PXRD), nitrogen adsorption (BET) and high resolution transmission electron microscopy (HRTEM) analysis. The two routes give quite different materials although in both cases the products are essentially highly crystalline, dense particulates. It was found that the reverse precipitation technique gave the smallest crystallites with the narrowest size dispersion. This route also gave as-synthesised materials with higher surface areas. HRTEM

confirmed the observations made from PXRD data and showed that the two methods resulted in quite different morphologies and surface chemistries. The forward route gives products with significantly greater densities of $Ce^{3+}$ species compared to the reverse route. Data are explained using known precipitation chemistry and kinetic effects.

Chapter five centres on the addition of terbia to ceria and has been investigated using XRD, XRF, XPS and TEM. Good solid solutions were formed across the entire composition range and there was no evidence for the formation of mixed phases or surface segregation over either the composition or temperature range investigated. Both $Tb^{3+}$ and $Tb^{4+}$ ions exist within the solution and the ratios of these cations are consistent with the addition of $Tb_8O_{15}$ to the fluorite ceria structure across a wide range of compositions. Local regions of anion vacancy ordering may be visible for small crystallites. There is no evidence of significant $Ce^{3+}$ ion concentrations formed at the surface or in the bulk by the addition of terbia. The lattice parameter of these materials was seen to decrease with decreasing crystallite size. This is consistent with increased surface tension effects at small dimension.

Chapter six reviews size related lattice parameter changes and surface defects in ceria nanocrystals. Ceria ($CeO_2$) has many important applications, notably in catalysis. Many of its uses rely on generating nanodimensioned particles. Ceria has important redox chemistry where $Ce^{4+}$ cations can be reversibly reduced to $Ce^{3+}$ cations and associated anion vacancies. The significantly larger size of $Ce^{3+}$ (compared with $Ce^{4+}$) has been shown to result in lattice expansion. Many authors have observed lattice expansion in nanodimensioned crystals (nanocrystals), and these have been attributed to the presence of stabilized $Ce^{3+}$ -anion vacancy combinations in these systems. Experimental results presented here show (i) that significant, but complex changes in the lattice parameter with size can occur in 2-500 nm crystallites, (ii) that there is a definitive relationship between defect chemistry and the lattice parameter in ceria nanocrystals, and (iii) that the stabilizing mechanism for the $Ce^{3+}$ -anion vacancy

defects at the surface of ceria nanocrystals is determined by the size, the surface status, and the analysis conditions. In this work, both lattice expansion and a more unusual lattice contraction in ultrafine nanocrystals are observed. The lattice deformations seen can be defined as a function of both the anion vacancy (hydroxyl) concentration in the nanocrystal and the intensity of the additional pressure imposed by the surface tension on the crystal. The expansion of lattice parameters in ceria nanocrystals is attributed to a number of factors, most notably, the presence of any hydroxyl moieties in the materials. Thus, a very careful understanding of the synthesis combined with characterization is required to understand the surface chemistry of ceria nanocrystals.

# Table of Contents

# 1 Chapter One - An introduction to $CeO_2$ – Structure, chemistry and applications

## 1.1 Cerium Oxide

Ceria (and doped ceria (Ce)) materials has become one of the most important class of ceramic materials with a host of applications. $CeO_2$ has a number of important and varied catalysis uses (most notably as an important component of the three way automotive catalyst (TWC)), [1], as an ionic conductor [2], as a gas sensor [3] and as an electrolyte material of solid oxide fuel cells [4]. Ceria thin films exhibit exceptional electronic properties such as optical transparency, high refractive index (*n*) and high direct current (dc) dielectric constant (*k*). Therefore, it is an attractive material for the gate oxide in CMOS technology, where high-*k* dielectrics are required.

Cerium dioxide in the nanoparticulate form has been the centre of intense academic and industrial research because of its' redox chemistry. Ceria has well understood non-stoichiometry centred around the ease of formation of anion vacancies [5] and these form ordered superstructures based around the cubic fluorite lattice structure exhibited by ceria [6]. The anion vacancies are associated with localised or small polaron states formed by the electrons that remain after oxygen desorption. In more simple terms, electrons formed during $O_2$ removal as $O_2$ (g) combine with $Ce^{4+}$ states to form $Ce^{3+}$ states, whose larger ionic radii is associated with a lattice expansion compared to stoichiometric $CeO_2$ [5]. This is a very simplistic explanation and greater defect chemistry complexity is suggested in literature. Morris *et al.* [7], Esch *et al.* [8] and Namia and co-workers [9] have shown that vacancies are mobile and may result in vacancy clustering.

Ceria nanoparticles are of particular interest because of the high catalytic activity and surface area of small particulates, as well as better sinterability, for example, by

comparison with coarse grained bulk materials [10]. The sensitivity of the cerium electronic band structure to the environment would suggest that changes in the properties of ceria particles at the nanoscale dimensions might be expected. The change in lattice constant of ionic crystallites with decreasing nanoparticle size is an important issue that is not fully understood [11] and Tsunekawa *et al.* report lattice expansion with decreasing particle size for several nanosized $CeO_2$ particle preparations [12]. There are numerous chemical methods for the production of nano-dimensioned particles of ceria. These include precipitation, sol-gel techniques, micellar controlled (nanoreactors) and oxidation. Most syntheses of ceria nanoparticles aim to provide spherical particles of high surface area, which are either non-agglomerated or weakly agglomerated. However, each preparation method will produce materials with different defect densities and morphologies and it is difficult to relate any changes to variations in particle dimensions.

The understanding of oxide nanoparticles is limited and their full and quantitative characterisation offers serious challenges. The work reported herein is a careful study of a series of chemical preparations together with morphological characterization of both undoped and doped ceria ($CeO_2/La_2O_3$ and $CeO_2/TbO_x$) systems, which provides further evidence for complex defect arrangements in these materials. Based on these results and a review of literature it is worthwhile asking if a model of surface enhanced defect concentration is consistent with known cerium/cerium oxide chemistries, whether this is applicable to a range of different synthesis methods and if a more consistent description is possible?

## 1.2 Nanoparticles

The word nano represents a fraction that indicates one billionth of a unit quantity. Nanoscience is redefining the understanding of matter at an extraordinary pace every day. Nanoparticles of carbon black soot have always existed and are a polluting by-product of burning fossil fuels. Some of the most promising early research into

nanomaterials was conducted in the early eighties by a research group led by Richard Smalley at Rice University. They found that 60 carbon atoms could arrange themselves symmetrically in the shape of a stitched soccer ball one nanometre in diameter. They named the structure a "fullerene" after the geodesic dome designer Buckminster Fuller. Somio Iijma later discovered that the elongated version of these fullerenes, carbon nanotubes, were 100 times stronger than steel despite being only 1/6 its weight [13, 14]. These fullerenes are currently being investigated as free-radical scavengers and as an antioxidant against neurodegenerative disorders such as Parkinson's and Alzheimer's diseases – this illustrates the versatility of nanomaterials and the impetus behind realizing and researching their potential.

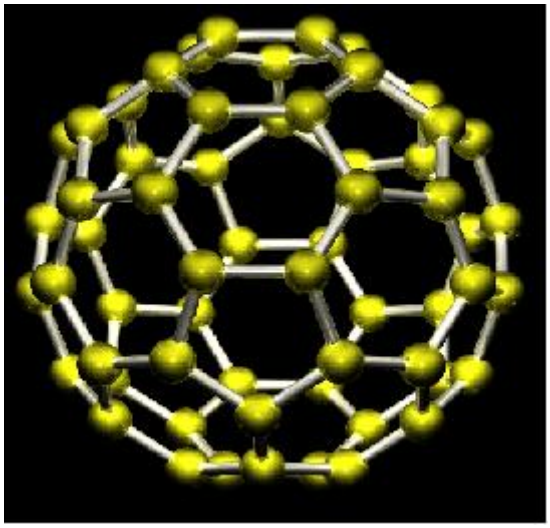

**Figure 1.1** Structure of Buckminsterfullerene

The significantly different physical properties of nanomaterials have been ascribed to their characteristic structural features which lie in between that of isolated atoms and the bulk macroscopic materials [15]. "Quantum confinement", is the result of changes in the electronic band structure deriving from the ultra-small length scale. In very simple terms, the electron delocalization seen in bulk solids that results in bands, is not observed and electrons lie in discrete orbitals, so that a very small nanoparticle has a band structure resembling an atom. The sometimes exceptional electronic, mechanical, optical and magnetic properties of nanoscale materials can all be attributed to the changes in the total energy and structure of the system. In the free

electron model the energies of the electronic states and the spacing between energy levels, both vary as a function of $L^{-2}$, with L being the dimension in that direction [16]. At the nanoscale dimensions the normally collective electronic properties of the solid become severely distorted and the electrons at this length scale tend to follow the "particle in a box" model. Note, that the higher order calculations are often required to account for band structure [16]. The electronic states in nanomaterials are more like those found in the localized molecular bonds than the bonds formed in macroscopic solids. The main implication of such confinement is the change in the system total energy and, hence, the overall thermodynamic stability. The chemical reactivity, being a function of the system structure and the occupation of the outermost energy levels, will be significantly affected at such a length scale, causing a corresponding change in the physical properties.

As well as the electronic effect, small dimensions can control the surface properties. There is a huge surface area per gram of nanoparticulate material. This is imperative for it's catalytic uses, as only the surface atoms are directly involved in catalysis. The activity of a catalyst is proportional to the number of sites present. Therefore, the greater the surface area, the more adsorption and reaction sites are available and the greater the conversion. Also, because of their minute size and large surface area, nanoparticles tend to become electrically charged and thus chemically more reactive making them ideal catalysts. A smoke particle is 1,000 nm and is easily suspended in air, so, being so small, one might expect problems with working with nanoparticles [17]. However, electrostatic forces cause the particles to clump together to form an easily handled powder.

Chemical properties, mechanical properties, electrical and magnetic properties can all alter with respect to the bulk material. A good example of this is $Fe_2O_3$, maghemite; in bulk form it is used in disc drives and cassettes as a recording medium because of its magnetic properties. However, in nanoparticulate form, these properties become "superparamagnetic", and as a result has led to new applications in MRI and magnetocaloric refrigeration [18].

Optically, the properties can change also, as mentioned above. An example of this is in sunscreens in which zinc oxide or titanium dioxide was used traditionally in opaque,

white macroparticle form. Nanoparticles most ubiquitous use to date is possibly in UV-resistant cosmetics and sunscreens, which now contain titanium dioxide nanoparticles, which are transparent. The opaque, white particles work by physically blocking or reflecting the harmful UV radiation. However, the question has arisen as to whether these nanoparticles of titanium dioxide are chemically the same as the macroparticles of titanium dioxide, with the exception of being transparent [13].

The importance of nanoparticles cannot be underestimated. Optical, chemical, mechanical, magnetic and electrical properties can be controlled by engineering the size, morphology and composition of the particles. These properties of the nanoparticles can then be exploited and combined to allow industries to re-engineer and enhance existing products and to develop novel and innovative products that function at unprecedented levels.

## 1.3 Flourite Crystal Structure of Ceria

Ceria is white crystalline solid that adopts a yellow tinge when slightly impure. A unit cell of ceria consists of a cubic array of oxygen atoms as a framework for the metal atoms which occupy alternate cubes [19]. This is called the fluorite structure, which is named after the mineral form of calcium fluoride, $CaF_2$, and is illustrated in Figure 1. It is described as a face centred cubic (f.c.c.) unit cell with the space group *Fm3m*, and a lattice constant, a = 0.541134 nm. In this structure, each cerium cation occupies the face-centred positions and is coordinated by eight equivalent nearest neighbour oxygen anions. The oxygen anions themselves occupy the tetrahedral positions in the lattice and are coordinated by four cations [20]. Under reducing conditions and at high temperatures the ceria structure is known to form a series of independent, oxygen deficient non-stoichiometric $CeO_{2-x}$ oxide structures (with $0 \leq x \leq 0.5$) [21, 22, 23]. At lower temperatures, however, ceria has a tendency to form discrete compositions. The reductive properties of ceria which readily forms oxygen deficient non-stoichiometric phases is due to its ability to release bulk oxygen and so form a large amount of anion vacancies. The “reduced” structures still retain the fluorite structure, i.e. there is no

obvious gross phase transformation to a thermodynamically stable structural entity, and can be readily reconverted to $CeO_2$ by exposure to an oxidising environment [24, 25, 26]. Despite numerous detailed mechanistic arguments which often clash in detail, it is clear that the high lability of ceria to lattice oxygen is one of the main contributors to its important practical properties.

It is these redox capabilities that give ceria an almost unique place in the catalysis industry as an oxygen storage medium and the reason behind the increased number of studies to investigate the relationship between the structural and catalytic properties of fluorite ceria and ceria based mixed oxide systems. As the catalytic behaviour of ceria can be modified by the addition of dopants or incorporation of different elements into the lattice, the need for more detailed structural analysis is increasing. This will be further illustrated in discussions below.

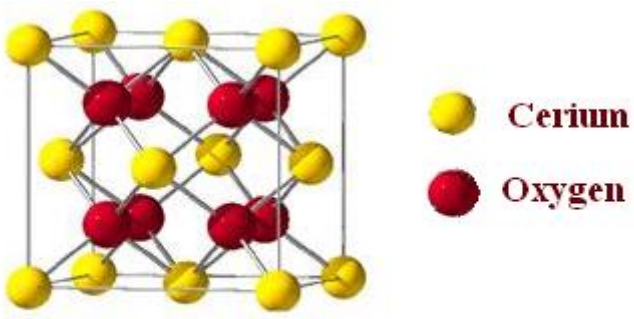


**Figure 1.2** The face centred cubic cell of fluorite ceria.

## 1.4 Redox Properties of Ceria

### 1.4.1 Reduction reactions

The reduction of ceria has been extensively studied due to its importance in the catalysis industry. The reaction of ceria with hydrogen [27, 28] and carbon monoxide

[29, 30] have yielded the most important insights into the structural chemistry of the reductive cycle of ceria. From studies [23-26] completed using TPR (Temperature Programmed Reduction) and XRD, a kinetic model for the reduction of ceria comprising of four main steps has been proposed. This can be summarised below (as discussed by Trovarelli) [14]:

1. Dissociation of chemisorbed $H_2$ to form hydroxyl groups at the surface.
2. Formation of anionic vacancies and reduction of neighbouring cations.
3. Desorption of water by recombination of hydrogen and hydroxyl groups.
4. Diffusion of surface anionic vacancies into the bulk material.

When ceria is supported on other oxides such as silica and alumina the reductive behaviour is modified depending on the extent of interaction between the two oxides. Similarly, by introducing dopant ions into the bulk ceria lattice the reductive tendencies can be modified to suit a particular purpose. Smaller $4^+$ cations such as Zr and Hf when introduced into the lattice results in a defective fluorite structure with increased oxygen mobility. The reducibility of these solid solutions is strongly dependent on the structure of the material. For example an increase in reducibility is seen for $Ce^{4+}$ / $Tb^{4+}$ in Ce-Tb-La solid solutions [31], for Pr in Ce-Pr mixed oxides [32] and for $Ce^{4+}$ in ceria / titania mixed oxides. However, in contrast to the former examples, the increase in the latter case is due to the formation of a stable $CeTiO_3$ compound and not due to more favourable energetics for $Ce^{3+}$ formation in the fluorite lattice [33].

### 1.4.2 Oxidation reactions

Oxidation reactions account for the majority of uses of ceria containing materials in catalysis. The redox properties of ceria and the high lability of lattice oxygen are among the most important factors which contribute to the catalytic reactivity of ceria

in oxidation reactions. Although ceria has proven its worth in total oxidation reactions [29, 34], its ability to catalyse selective or partial oxidations is poor. However, the catalytic behaviour can be modified by the addition of dopants or incorporation of different elements into the lattice. This in turn allows for the "fine tuning" of the catalyst and even opens reaction pathways that can lead to partial oxidation products. Generally, the best catalysts are multi-component systems comprising of ceria and a metal dopant; in such catalyst systems, ceria provides for the unique capability of promoting oxidation reactions.

## 1.5 Commercial Uses of Ceria Nanoparticles

### 1.5.1 Automotive Catalysis

Since the beginning of the 1980's the use of $CeO_2$ in automotive pollution control has become so prevalent that, today, it represents the most important application of this lanthanide oxide [35]. The development of TWCs was dictated by the need to simultaneously convert the hydrocarbons (HCs), CO and $NO_x$ present in the exhaust gases of spark-ignited internal combustion engines to $H_2O$, $CO_2$ and $N_2$ respectively.

TWC catalyst formulation consists primarily of noble metals and metal oxides, dispersed either, on the surface of alumina pellets, or on an alumina washcoat, anchored to a monolithic ceramic substrate, as shown in Fig. 1.3. The monolith is designed to be both impact and thermal shock resistant. This is very important since the converter may experience a 500K increase in temperature after ignition, in a short time interval. The monolith has to retain the catalyst throughout this temperature increase, and so has a low thermal expansion coefficient. A high surface area alumina support is deposited onto the monolith by a technique known as "washcoating", i.e. slurry deposition. The whole catalyst monolith is then impregnated with a solution of salts of the main active metals, Pt, Pd, and Rh.

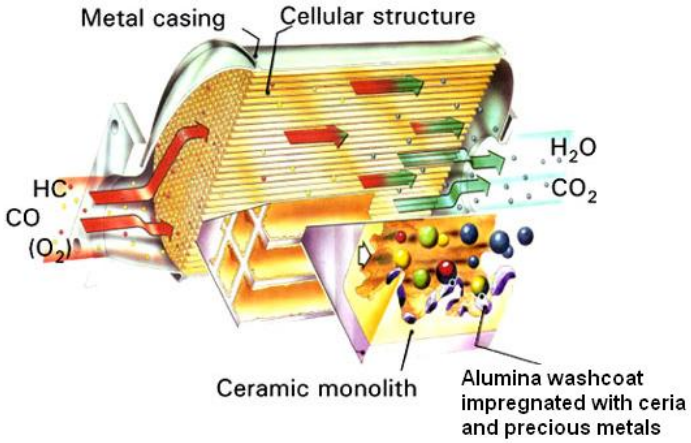


**Figure 1.3** Cross-section of a car catalyst with views of the washcoat and active phase. [36]

Highest conversion of the pollutants is obtained when the air-to-fuel (A/F) ratio is ~ 14.6, a range known as the "window", over which conversion of each pollutant does not fall below a required value. However, in reality, the catalyst is exposed to constantly varying feedstream compositions, going alternately from rich exhaust stoichiometry (deficient $O_2$) to lean stoichiometry (excess $O_2$), which severely decrease the efficiency of the TWC.

Incorporation of ceria into the TWCs has numerous advantages, the most significant being its ability to be easily and reversibly reduced to several $CeO_{2-x}$ stoichiometries, when it is exposed to $O_2$ deficient atmospheres, due to the $Ce^{3+}/Ce^{4+}$ redox couple. The following equations are examples of the possible reactions that may take place in the exhaust feedstream:

i. $CeO_2 + xCO \rightarrow CeO_{2-x} + xCO_2$

(Oxidation of CO–takes lattice oxygen)

ii. $CeO_2 + C_xH_y \rightarrow CeO_{2-(2x+0.5y)} + xCO_2 + 0.5yH_2O$

(Oxidation of hydrocarbons with more lattice oxygen)

iii. $CeO_2 + xH_2 \rightarrow CeO_{2-x} + xH_2O$

(Possible because hydrocarbons can form $H_2$ over Pt and Pd)

iv. $CeO_{2-x} + xNO \rightarrow CeO_2 + 0.5xN_2$

(Reduction, NO is giving $O_2$ back to Ce)

v. $CeO_{2-x} + xH_2O \rightarrow CeO_2 + xH_2$ (Reduction of water)

vi. $CeO_{2-x} + 0.5xO_2 \rightarrow CeO_2$ (Oxidation)

Ceria has the ability to donate its oxygen for the removal of CO and hydrocarbons during the oxygen deficient portion of the cycle (reactions i-iii), while adsorbing and storing oxygen from $O_2$, NO and $H_2O$ during excursion into the lean part of the cycle, (reactions iv-vi), thus enlarging the "window" of operation. This extraordinary oxygen storage capacity (OSC) of ceria, first reported by Gandhi *et al*. [37] in 1976, is as a result of a unique and delicate balance between several factors [38, 39]:

- Structural – phase formation.
- Kinetic – rate of redox of $Ce^{+4/+3}$.
- Textural – presence of surface cerium sites.

The use of cerium oxide in the catalysis industry is growing primarily due to the wider use of automobile exhaust emission control. The variety of catalytic systems which can benefit from the use of ceria will also increase and might provide further systems as oxidation and combustion catalysts [33, 34]. Their total oxidation capabilities, which rely heavily on the efficiency of the Ce redox couple and on their high ion transport properties, could provide interesting materials for use in several catalytic processes for environmental applications. For optimization and control of these materials, a better understanding of the structural relationship of nanoparticulate ceria and ceria based mixed oxide systems may provide the necessary tools to design complex multi component systems.

### 1.5.2 Ceria as an electrolyte for solid oxide fuel cells

William Grove developed the first fuel cell in 1839. However, it is only today that they are truly emerging as alternative electrochemical energy sources, using

hydrocarbon-based fuels to deliver clean, quiet and potentially renewable energy. One of the distinct advantages of fuel cells is that the absence of combustion eliminates harmful emissions.

A fuel cell has three main components; the anode, the cathode and the electrolyte. The cathode receives oxygen from the air and the anode receives hydrogen (and carbon monoxide if the $H_2$ is derived from a hydrocarbon source). The electrolyte separating the cathode and anode conducts oxygen anions from the cathode to the anode, where the ions combine with hydrogen to produce water. The remaining electrons at the anode are then returned to the electron-deficient cathode via an external load, producing a flow of electricity. Heat is also produced due to the electrochemical process and resistance in the electrolyte [40].

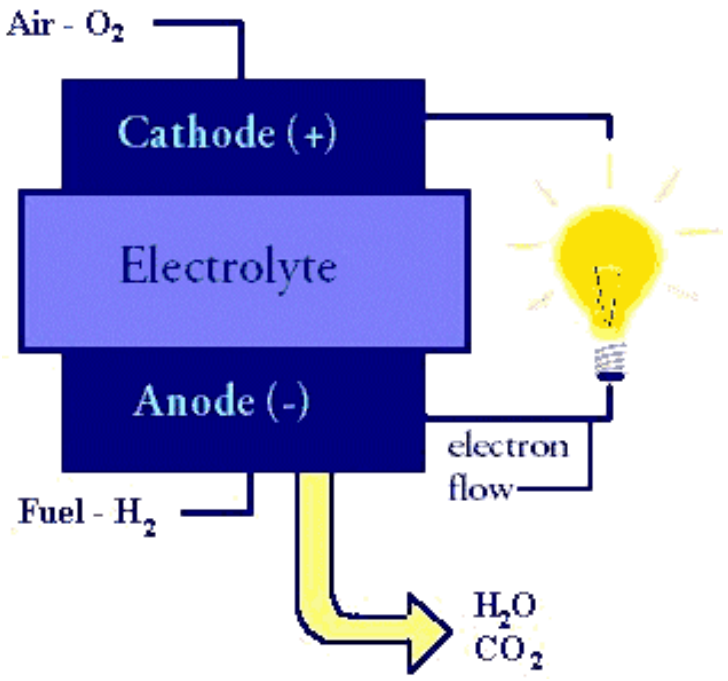


**Figure 1.4** Diagram of fuel cell operation.

The most important component in an electrochemical cell is the electrolyte, which is an ionically conducting membrane that separates 2 electrodes. Current electrolytic materials are doped-zirconia based systems that operate at temperatures of over 900°C.

A typical zirconia electrolyte is ytrria stabilised zirconia (YSZ) which exhibits high oxygen anion conductivity at high temperatures and is stable under reducing conditions. Replacing YSZ with an intermediate temperature (IT) oxide ion conductor would increase efficiency and longevity of the cell, along with reducing material and fabrication costs [41]. However, despite immense research, it has proved difficult to find an oxide that fits the criteria. Nonetheless, in recent times, doped ceria has been suggested as an alternative electrolyte for fuel cells. Like doped zirconia, doped ceria nanopowder displays high oxide ion conductivity and exhibits the same fluorite structure. In fact the oxide ion conductivity of ceria demonstrates superior performance in that it is approximately an order of magnitude greater than that of the conventional solid oxide fuel cell electrolytes, YSZ. Again, oxygen mobility is greatest in a cubic lattice, as compared to the limiting geometries of tetragonal and monoclinic lattices [42,43, 44]. The larger lattice parameter in nanocrystalline ceria implies the migration enthalpy of an oxygen vacancy is smaller resulting in a higher ionic conductivity and more efficient fuel cells [45, 46]. It would be essential to dope ceria due to its poor mechanical strength and high electrical conductivity. In the thesis to follow, it is hoped to present an in-depth analysis of the structural chemistry of undoped and doped ceria as part of this process.

## 1.6 General Lanthanide Chemistry

### 1.6.1 The Elements

The term lanthanide, is the least confusing description of the elements with atomic numbers [47, 48, 49, 50, 51, 52, 53, 54, 55, 56, 57, 58, 59, 60, 5]. Indeed,

historically this group of elements has been named “rare earths (RE)”, “the cerium group” and the “light earths”. It has now become common practice that the term “rare earths” describes the elements from cerium to luethium. It is not particularly applicable since, in truth, they are not rare and do not have earth-like properties. Even so, there is still no universal agreement about the position of leutetium, i.e. whether the lanthanides are made up of the elements lanthanum to leutetium or cerium to leutetium, since theory and practical measurements suggest La has no f electrons but practically it is always included. Despite the fact that yttrium lies outside the above mentioned range it is still classed as a rare earth due to the similarities in oxidation state and physical properties to lanthanum.

In reality, the lanthanides comprise the largest naturally occurring group in the periodic table. Table 1.1 illustrates the natural abundance of the lanthanide elements. Cerium is in fact the twenty sixth most abundant element. Only promethium-147 can actually be described as rare with only traces being found in uranium cores and is more usually classed as a contaminant (a decay product) in waste uranium fuels. Over 100 naturally occurring lanthanide containing minerals have been discovered to date. However, only two are of commercial importance; those being monazite ~ (La, Th, Ln phosphate) and bastnaesite (La, Ln fluorocarbonate).

**Table 1.1:** Natural abundance's of the lanthanide elements (ppm) in the earth's crust [61].

| **Element** | **Abundance** | **Element** | **Abundance** |
|---|---|---|---|
| La | 35 | Tb | 1.2 |
| Ce | 66 | Dy | 4.5 |
| Pr | 9.1 | Ho | 1.44 |
| Nd | 40 | Er | 3.5 |
| Pm | $4.1 \times 10^{-20}$ | Tm | 0.5 |
| Sm | 7.0 | Yb | 3.1 |
| Eu | 2.2 | Lu | 0.8 |
| Gd | 6.1 | | |

### 1.6.2 Oxidation States

The lanthanide elements are highly electropositive since the sum of the first three ionisation enthalpies for all the elements is relatively low. Their chemistry is dominated by the 3+ oxidation state. The elements readily form this trivalent cation in the form of oxides, aqueous ions and complexes. Variations do exist, however, especially in the chemistry of cerium in which the 4+ cation is often the most thermodynamically stable form. This four-valent state is not confined to cerium. Other elements can exist in this manner in solids, for example, $TbO_2$ and $Pr_2$. Here, the extra energy to remove the fourth electron is a result of the extra lattice stability of the fluorite structure that is formed. The reduction of the halides ($LnX_3$), with the excess metal (Ln) can access not only $LnX_2$ but also further reduce species in which metal-metal interactions are probable.

It was originally considered that the formation of empty, half filled or filled f orbitals

was the driving force behind the generation of $2^+$ and $4^+$ states. This explanation seems quite improbable since Sm and Tm give the divalent cations having configurations $f^6$ and $f^{13}$ but do not exist as the monovalent cation. Pr and Nd cations give $4^+$ cations with $f^4$ and $f^2$ configurations but no $5^+$ or $6^+$ species. What is more likely is that existence of a particular oxidation state is governed partly by its ionisation enthalpies [62, 63], enthalpies of sublimation, lattice energies etc. [64] and prediction of stabilities can only be made on the basis of detailed calculations.

Table 1.2 shows the trend of ionic radii of the trivalent lanthanides in 6-coordination. It can be seen that a gradual decrease occurs over the latter half of the series but the first elements suffer a large contraction. The f electrons poorly shield nuclear charge and as a result there is a concomitant reduction in cation radius with increasing atomic number. This reduction, termed the "lanthanide contraction", is most apparent for the first few members of the period. It should be noted also that there is a slight discontinuity at the spherically symmetrical $Gd^{3+}$ ($4f^7$) ion. Some of the elements do, however, tend to exist in more than one oxidation state. In this thesis, the structural changes which result in oxidation state transitions are studied for the elements La, Ce and Tb.

**Table 1.2:** Ionic radii of $Ln^{3+}$ cations in 6 fold co-ordination.

| | Radius/pm[7] | | Radius/pm[7] | | Radius/pm[7] |
|---|---|---|---|---|---|
| $La^{3+}$ | 106.1 | $Sm^{3+}$ | 96.4 | $Ho^{3+}$ | 89.4 |
| $Ce^{3+}$ | 103.4 | $Eu^{3+}$ | 95.0 | $Er^{3+}$ | 88.1 |
| $Pr^{3+}$ | 101.3 | $Gd^{3+}$ | 93.8 | $Tm^{3+}$ | 86.9 |
| $Nd^{3+}$ | 99.5 | $Tb^{3+}$ | 92.3 | $Yb^{3+}$ | 85.8 |
| $Pm^{3+}$ | 97.9 | $Dy^{3+}$ | 90.8 | $Lu^{3+}$ | 84.8 |

## 1.7 Modelling of the Lattice Parameter

The present work was initiated to investigate the role of dopant ion size and concentration on the lattice parameter of ceria. For such a lattice parameter study, it is desirable that

a) dopant oxides cover a wide range of cation radii and
b) the material exhibit a solid solution over a wide range of compositions.

Trivalent rare-earth oxides were chosen as dopants because they have extensive solubility in ceria [65, 66]. The change in ionic radii with coordination number (CN) was first noted by Goldschmidt, Shannon, and Prewitt [67, 68], who obtained an empirical set of effective ionic radii from the enormous amount of data with consideration of the valence, coordination number and the spin of ions. They are now broadly used in crystallographic studies of oxides.

In a perfect fluorite structure, the coordination numbers (CN) of oxygen ions and cerium ions are 4 and 8 respectively. Even though the octahedral packing of oxygen ions with respect to cerium ions does not yield the ideal ionic radii ratio, ($r_{Ce4+}$ /$r_{O2-}$ = 0.97/1.38 ≈ 0.7 < ideal ratio = 0.732), it is known that the fluorite structure is stable and can dissolve a high concentration of an aliovalent dopant. The lattice parameter, a, is given for an ideal fluorite structure by:

$$a = 4/\sqrt{3}\ (r_{cation} + r_{anion}) \qquad \text{Eq(1.1)}$$

As rare-earth oxides are introduced in ceria, the following defect reaction is known to occur predominantly upon formation of a solid solution [69].

$$x MO_{1.5} + (1 - x)CeO_2 \rightarrow x M_{Ce} + 0.5x V_{\ddot{O}} + (1 - x)Ce_{Ce} + (2 - 0.5x)O_O \qquad \text{Eq(1.2)}$$

This reaction implies that as $x$ moles of $MO_{1.5}$ are added, $Ce^{4+}$ sites are filled with $x$ moles of dopant cations $M^{3+}$ and $1 - x$ moles host cations $Ce^{4+}$ and, in the same way, $O^{2-}$ sites are occupied by $0.5x$ moles of oxygen vacancies and $2 - 0.5x$ moles of host anions $O^{2-}$.

A postulate based on this defect reaction suggests that the four different species $M_{Ce}$, $V_O$, $Ce_{Ce}$, $O_O$ are the only ones that take part in the formation of $MO_{1.5} - CeO_2$ solid solutions (the participation of impurities is neglected) and the ionic sizes of these species would determine the lattice parameter of the unit cell. In other words, the ionic radii of the cerium ion ($r_{Ce}$), the dopant ion ($r_M$), the oxygen ion ($r_O$) and the oxygen vacancy ($r_{Vo}$) determine the lattice parameter of the unit cell. This assumes that a unique value of an oxygen vacancy can be assigned for a given solid over a range of compositions of interest.

## 1.8 Defect Chemistry of Cerium oxide

The significance of this section has become apparent in recent years due to the increased catalytic and ionic conductivity performance in certain oxides especially ceria when doped with lanthanide sesqui-oxides [53, 54]. The defect chemistry of ceria is relatively well established. It is generally thought that as a trivalent cation is added to the lattice, it is charge compensated for by the presence of anion vacancies. These are associated with the dopant cations and randomly distributed on anion sites within the fluorite lattice. In particular, whilst this may be the thermodynamically most important defect mechanism, other defect systems are possible as minority species [70] and experimental evidence for interstitial oxygen defects has been found for nanoparticles of ceria [71]. Intrinsic defects may be present because of thermal disorder or can be created by the reaction between the solid and the surrounding atmosphere. Extrinsic defects are formed by impurities or by the introduction of aliovalent dopants. Defects in ceria can be either intrinsic or extrinsic. There are three

possible thermally generated intrinsic disorder reactions in ceria that do not involve exchange with the gas phase. These defects are of the Schottky Equation (Eq. 1.3) and Frenkel Equation (Eq. 1.4 and 1.5) types [20]. These defects are defined as follows:

- A Schottky Defect is when an atom leaves its original site and migrates to the surface of the crystal
- A Frenkel Defect is when an atom transfers from an original lattice site and resides at an interstitial position, a position not normally occupied by the atom.

These types of defects can be represented using the Kroger and Vink defect notation:

$$Ce_{Ce} + 2\ O_O \leftrightarrow V''''_{Ce} + 2\ V_O + CeO_2 \qquad \text{Eq(1.3)}$$

$$Ce_{Ce} \leftrightarrow Ce_i^{\cdots} + V''''_{Ce} \qquad \text{Eq(1.4)}$$

$$O_O \leftrightarrow O_i'' + V_{\ddot{O}} \qquad \text{Eq(1.5)}$$

$Ce_{Ce}$ - cerium at a cerium site

$O_O$ - oxygen at an oxygen site

$V_O$ - a vacancy at an oxygen site

$Ce_i^{\cdots}$ - the number of electrons

V'''' represents positive charge.

These lead to the formation of pairs of oxygen vacancies and oxygen interstitial positions. In the case of exposure to a reducing gaseous atmosphere, this leads to a high concentration of such defects. Upon reduction, ceria has an excess of metal compared to its anion content; its cation/anion ratio is greater than 0.5. There are two principle ways to accommodate this variation in composition. In the first case, oxygen vacancies are assumed to compensate the holes formed on reduction of $Ce^{4+}$ to $Ce^{3+}$. When oxygen is removed, the crystal will end up with an overall positive charge and two electrons for each oxygen ion moved need to be introduced in order to keep the crystal neutral. The presence of anion vacancies is accompanied by an increase in the

lattice parameter of $CeO_2$. This is because of the larger sizes of $Ce^{3+}$ compared to $Ce^{4+}$. This lattice expansion will be dealt with in detail in later chapters.

## 1.9 Doping of the Ceria Lattice

As stated previously the performance of ceria can be enhanced by doping this oxide with a second metal (M = Zr, Ca, Cu, Au, Pt, Tb, La etc) [72, 73, 74]. Mixed oxides maintain fluorite type structures, particularly the cation sublattice, up to a high level of doping. The doping element in many cases enhances the thermal stability of the support system or favours the transport of oxygen (conversion between $Ce^{3+}$ and $Ce^{4+}$ oxidation states). In some situations, doped ceria nanoparticles become very active catalysts for reactions such as the water-gas shift or the destruction of $SO_2$ [20, 73]. This effect is achieved by doping with noble metals such as Cu, Au, or Pt, and the phenomenon is not fully understood [75, 76, 77]. However, these properties of ceria-based systems are mainly driven by two physiochemical phenomena: the local M-O ordering and distance and the way the systems achieve charge neutrality, which in the case of ceria is mainly through the presence of oxygen vacancies.

For technological applications at high temperature, one wants a dopant agent that introduces a reasonable amount of O vacancies in the lattice of ceria and produces a mixed-metal oxide that has a high thermal stability [78]. The compromise between these two properties depends on a significant number of variables. Doping with Tb and other lanthanides as Pr may be a solution to this complex problem [79, 80, 81]. In the case of Tb, which will be discussed in greater detail herein, the relative stabilities of $Tb^{3+}$ and $Tb^{4+}$ states favour the formation of O vacancies in $Ce_{1-x}Tb_xO_2$. This makes Tb-doped ceria nanoparticles special for applications in automotive catalysts.

Despite the plethora of studies carried out in this defect system much of the

understanding of the solid state chemistry/physics has originated from theoretical studies and little detailed experimental evidence has been provided. In the results described within, further efforts to understand this complex system have been made.

# 2 Chapter Two – Experimental Techniques

## 2.1 Experimental

The properties of materials are structure-sensitive. Structure, in most circumstances, is defined by the lowest energy arrangement or arrangements of atoms or molecules. The structure obtained is determined by preparation, composition, heat treatment, and processing. Thus, it is necessary to characterise both composition and microstructure at the highest levels of resolution possible, in order to understand behaviour of materials and to facilitate the design of new or improved materials. Such characterisation requires advanced and sophisticated methods of analysis using microscopic, diffraction and spectrographic techniques. The various preparative approaches used in this project are now explained, along with the background and conditions of the different analytical techniques employed.

## 2.2 Preparative Synthesis Techniques

### 2.2.1 Precipitation

Solution techniques continue to be dominant in the preparation of multi-component oxide systems. This derives from the ease of mixing solutions of salts in precise ratios, which can then be converted to oxide powders, frequently preserving much of the chemical homogeneity of the solutions. Precipitation (or co-precipitation for multi-component systems) is one of the oldest of the non-conventional powder preparation techniques and is still a powerful and widely used method [82,83]. For laboratory applications, co-precipitation demands no specialized equipment. The most common form utilizes massive concentrations of hydroxide ions to simultaneously precipitate all the cation components in a solution. In these techniques, the homogeneous distribution of the components is not assured in the precipitates because segregation may occur during precipitation. To improve the homogeneity and crystallization, the precipitates are generally heat-treated by calcination after filtration

and drying. Calcination is the heat treatment of a ceramic precursor for the purpose of eliminating volatile constituents. Calcining is also accompanied by some surface area and bulk volume reductions. These processes bring about aggregation of the powders.

### 2.2.2 Sol-gel Synthesis Techniques.

*Roy* and co-workers [84, 85, 86] recognized the potential for achieving very high levels of homogeneity in colloidal gels and used the sol-gel method in the 1950's and 1960's to synthesize a large number of novel ceramic oxide compositions involving Al, Si, Ti, Zr, etc., that could not be made using traditional ceramic powder methods.

The goal of sol-gel processing is to control the surfaces and interfaces of materials during the earliest stages of production. Long-term reliability of a material is usually limited by localized variations in the physical chemistry of the surface and interfaces within the material. The emphasis is on limiting and controlling physical-chemical variability by the production of uniquely homogeneous structures, or producing extremely fine-scale (10-100 nm) second phases.

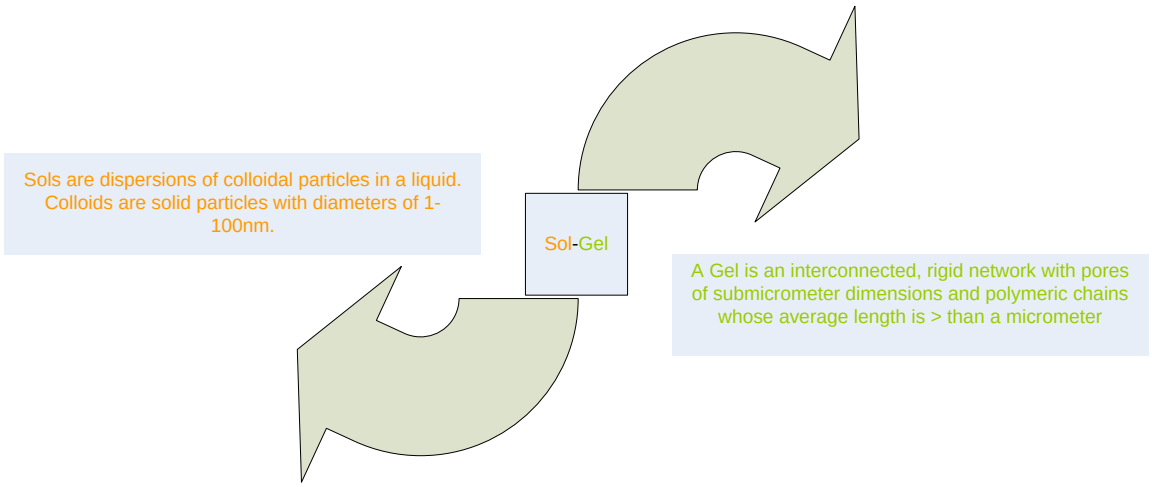


**Figure 2.1** Definition of a sol-gel. [87]

The sol-gel method is another route exploited in the synthesis of high quality, high-surface area nano-particles. There is a major evolution of structure during the

sol-gel transition. The system evolves from a sol, which, as described above, is a colloidal suspension of particles in a liquid (typically 1-100 nm). Gel refers to the semi-rigid framework in which the solid is contained in a framework of material. The sol can be prepared in two ways. It can be prepared by dispersing an insoluble solid in a liquid e.g. oxide/ hydroxide in water and then controlling the pH to keep the material suspended in solution. Another way of preparing the sol is by adding a precursor to solvent, which generates the colloidal product e.g. if metal alkoxides are added to water they will hydrolyse to oxides. Once the sol is formed, it is treated or left to generate a gel. An example of treating it would be to gently heat it for perhaps 2 weeks. The gel is then calcined to remove solvent and to decompose anions (such as carbonates and alkoxides to give oxides). The structure of the solid rearranges and allows crystallization to occur.

Alkoxide compounds have been extensively studied for use as molecular precursors in most of the sol-gel processes for synthesis of ceramic powders, films, coatings and monoliths. However, alkoxides are too expensive for some applications. In addition, moisture sensitivity and the rapid hydrolysis/condensation reaction rate of alkoxides lead to further complications in process and product control. Using cheaper precursors such as inorganic salts would be ideal if the equivalent level of quality in sol-gel processing could be achieved with such precursors. There are five basic steps on sol-gel formation [99] as represented in Figure 2.2.

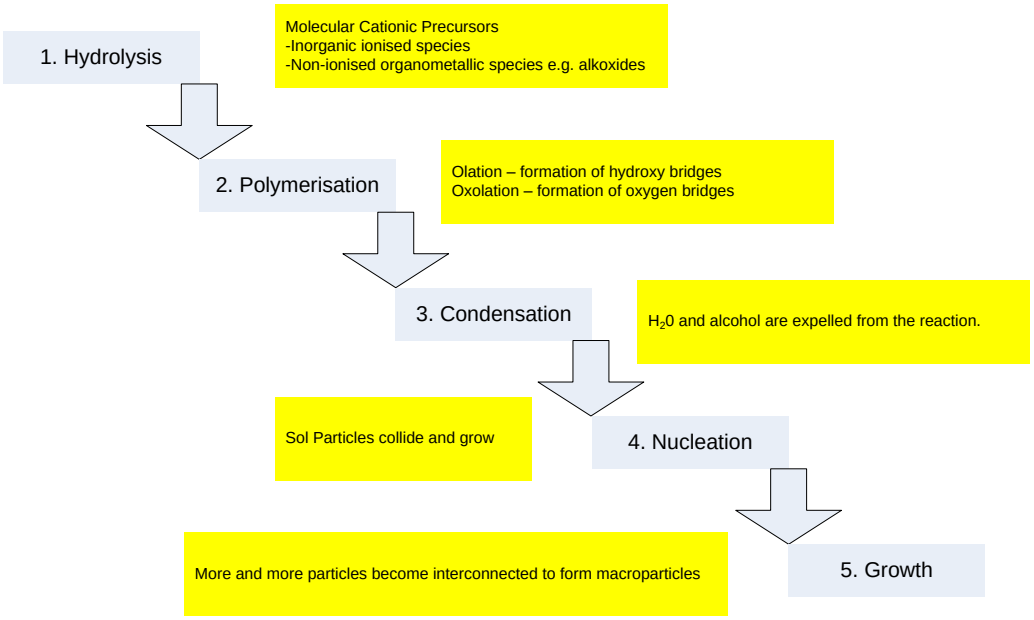


**Figure 2.2** The steps in sol-gel formation of a solid. [99]

Since it is the relative rates of hydrolysis and condensation that essentially determine the structure of the gel, it is imperative to understand the kinetics of the hydrolysis and condensation reactions, the ratio of their rate constants and ancillary influencing factors as illustrated in Figure 2.3. Yoldas [88] reported that the hydrolysis reaction and the condensation reaction are not separated in time but take place simultaneously. It has been well established that the presence of $H_3O^+$ ions in the solution increases the rate of the hydrolysis reaction, whereas $OH^-$ ions increase the condensation reaction [89].

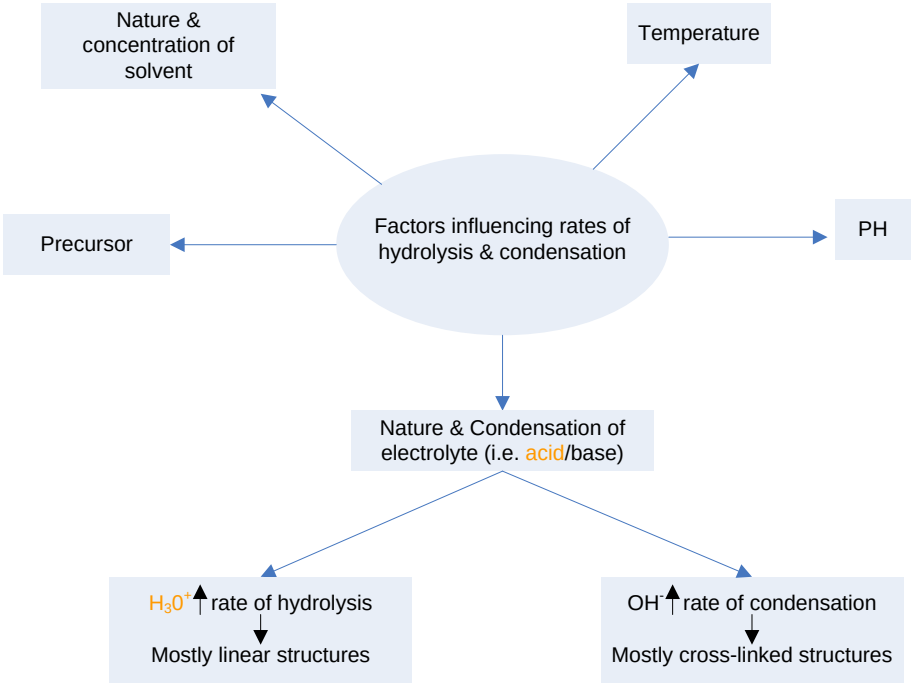


**Figure 2.3** Factors influencing rates of hydrolysis and condensation.

Orcel *et al.'s* studies [90] show that the shape and size of polymeric structural units formed via condensation are determined by the relative values of the rate constants for hydrolysis and polycondensation reaction ($K_h$ and $K_c$ respectively). Fast hydrolysis and slow condensation favour formation of linear polymers; on the other hand, slow hydrolysis and fast condensation result in larger bulkier and more ramified polymers. The gellation point of any system is easy to observe qualitatively, and simple to define in abstract terms, but extremely difficult to measure analytically. As the sol particles grow and collide, condensation occurs and macroparticles form. The sol becomes a gel when it can be deformed elastically. This is typically defined as the gellation point or gellation time, $t_g$. There is not an activation energy that can be measured, nor can one precisely define the point where the sol changes from a viscous fluid to an elastic gel. The change is gradual as more and more particles become interconnected.

Inorganic cerium nitrate precursors have been commonly employed in the sol-gel method. For example, one such synthesis involved dissolving polyethyleneglycol

(PEG) in water (solubility of PEG in water is 1 g $ml^{-1}$) and then adding the nitrate precursors before evaporating off the water to give a dense gel. At suitable PEG-nitrate ratios the PEG chains enclose the precursor molecules in a micelle. The gel is then heated further to decompose the nitrates and produce a powder [91].

### 2.2.3 Gel precipitation-peptisation method

The pursuit of high performance ceramic materials has prompted research to develop methods for synthesizing powders of high sinter activity, high purity and of homogeneous microstructure. In response to this, literature has established that fine powders of MgO-$ZrO_2$ have been produced by an in-situ chemical precipitation – peptisation method [92]. In this method, the magnesium and zirconia precursors were dissolved in triple distilled water and subsequently mixed together in a beaker under constant stirring with the oxalic acid being added dropwise to give a white gelatinous precipitate. The solution was allowed to equilibrate before being filtered and divided into 3 batches; each batch being treated differently. One batch was simply dried followed by calcination; the second batch was dried, then peptised with water to form a clear sol and gel, dried further and then calcined; while the third batch was washed with ethanol before being dried and subsequently calcined. On analysis, it was found that, in comparison to the other two batches, the batch treated with ethanol gave the smallest crystallite size at each temperature to which it was calcined, along with giving the highest specific surface area. This result could be explained by the suggestion that washing precipitated gels with alcohol produces soft agglomerates due to ethoxy groups inhibiting direct bonding during drying [93, 94].

### 2.2.4 Synthesis of "Bulk" Ceria Nanoparticles

In the research described herein, it was decided that the method of gel precipitation - peptisation outlined in the synthesis above could be adapted to try and propagate high-surface area ceria nanoparticles. Aside from the oxalic acid suggested in the

literature, two other acids, nitric acid and citric acid, respectively, were randomly chosen for comparative purposes.

Initially, bulk ceria was prepared via homogeneous precipitation based on the forced hydrolysis of cerium nitrate hexahydrate [95]. The pH of the solution is increased by for example, in-situ thermal decomposition of hexamethylenetetramine (HMT) to form ammonia, which in turn generates $OH^-$ as the precipitating ligand. Precipitation occurs when this ligand reacts with the metal cation, $Ce^{3+}$ in this case. Primary particles of several nanometres are obtained, although weak agglomerates of up to 1 micron are common. It is these agglomerates that densify on calcination.

If the precipitating ligand is added directly to the metal cation solution, there is little solution concentration. For this reason, it is better to generate the ligand *in-situ*. For this work, cheap, widely available ammonia was added to force hydrolysis by increasing the pH and generating the precipitating ligand.

Upon the addition of the acid, nitrate groups are substituted by acid complex ligands. Different acids have different complexing abilities. This results in a sol, which, on drying causes the nitrates to decompose and the ligands to condense to form a gel. Calcining evaporates any remaining solvent resulting in relatively high surface area nanoparticles.

The “bulk” ceria that was prepared was not actually bulk ceria as such, but nano-crystalline powder, which showed a high tendency to form dense agglomerates on calcination. Further treatment, such as peptisation with acid, is necessary to maintain the particle size within the nano-metre range on calcination and with relatively high surface area.

### 2.2.5 Forward and Reverse Precipitation

In the case of conventional "forward" precipitation, the precipitant solution (which is the base), is added to the cation solution (which is the acid), as described above. Alternatively, it may also be carried out by inverting the order of solution addition, as in the case of "reverse" precipitation. This procedure has been suggested to avoid the segregation effects that may occur where the initial and final pH of the cations is quite different [96]. The average crystal size after calcination is defined by this variable. Therefore, the environment in which nucleation and growth of the precursor precipitate is not the same for both routes [97]. As a result, ceramics with different structural characteristics might be expected.

Ceria nanoparticles were prepared via the precipitation-peptisation method using three different acids for comparison; citric acid, oxalic acid and nitric acid. For peptisation, crude bulk ceria had to be prepared. This was performed by "forward" precipitation of a 1 molar solution of cerium (III) nitratehexahydrate, $Ce(NO_3)_3.6H_2O$ ($M_r$ = 434.23 g). This was achieved by dissolving 43.423 g of $Ce(NO_3)_3.6H_2O$ crystals in deionised water in a 250 ml beaker. This solution was then carefully transferred to a 100 ml volumetric flask, where it was brought up to the calibration mark using deionised water. 100 ml of 1M solution was poured into a 250 ml beaker. A stirrer bar was added to the beaker, which was then placed on a stirrer/hot plate (at room temperature). A burette was then filled with 25 ml of ammonium hydroxide solution, which was slowly added to the solution in the beaker to precipitate out the $CeO_2$ under constant stirring. This resulted in a thick yellow/ white emulsion, which was left stirring for 30 min before being vacuum dried in a Buchner funnel. Once dry, the brownish/ purple precipitate was scraped into a crucible and dried overnight in the oven at 80°C. On drying, the precipitate was lemon yellow in colour and was ground down to a fine powder using a pestle and mortar.

The "reverse" precipitation technique was identical to the forward precipitation

technique, except that in this case 25 ml of the Ce (III) solution was added dropwise to 100 ml ammonium hydroxide initially. The colourless ammonium hydroxide solution turned pale brown on addition of the first drop of ammonium hydroxide. Further addition resulted in the formation of a thick brown/purple precipitate which was a dark brown/purple colour at the end of the process. During suction filtering and drying, the precipitate turned purple, green/yellow, and finally a bright yellow colour.

### 2.2.6 Ceria Doping

As discussed in Chapter one, the relationship between structural modifications and the sintering process are strongly affected by the redox properties of ceria. One way to stabilise the structure is to associate cerium oxide to other elements for obtaining solid solutions with improved thermal properties. Recent studies report the improvement of textural, redox, oxygen storage, and consequently, catalytic properties by introducing doping elements in the $CeO_2$ fluorite lattice [98, 99, 100, 101, 102, 103]. For the purposes of this project, the lanthanides chosen for use as dopant materials were lanthanum (La) and terbium (Tb).

### 2.2.7 Synthesis of acid-precipitated gel samples

3 g of the above bulk ceria powder was weighed out into a sample vial. 3 ml of 70% oxalic acid was then added to the vial using a micro pipette. A stirrer bar was placed in the solution and the vial was placed on a stirrer to stir overnight. This was repeated for 3 ml nitric acid and 3 ml citric acid and using 3 g of bulk ceria powder for each. A 10:1 molar ratio of lanthanum (La) or terbium (Tb) to cerium was used for dopant inclusion purposes.

After stirring, the acid peptised emulsions were scraped into crucibles and placed in the oven to dry at 80°C. The ceria-citric acid emulsion was light brown in colour, while the oxalic acid emulsion was pale yellow and the nitric acid emulsion was a

slightly darker yellow. The citric, oxalic and nitric emulsions dried to form cream, pale yellow and pale yellow/orange powders respectively. These powders were ground to a fine powder and returned to their crucibles ready for calcination. The precipitation samples were calcined in the following temperature range, 250°C to 1050°C progressing in 50°C increments, with a dwell time of 2 hours. As the temperature increased, all the ceria powder samples became a uniform pale yellow. At the higher temperatures, on removing the samples from the oven they were white in colour, however, they quickly assumed their pale yellow colour upon cooling.

The forward and reverse La-doped samples were prepared as described above except that the 1 M Ce (III) nitrate solutions were replaced by solutions containing 10 vol% 1 M La (III) nitrate hexahydrate. The forward precipitate was indistinguishable from that described above however, for the La doped sample the colour was a little darker at every step. The reverse doped precipitates were completely indistinguishable from the control samples.

The forward and reverse Tb-doped samples were prepared as described above except that the 1 M Ce (III) nitrate solutions were replaced by solutions containing 10 vol% 1 M terbium (III) nitrate pentahydrate. The forward doped precipitate looked almost identical to the forward control precipitate, except that it was brighter in colour. Once peptisation was complete the samples took on an orange/brown hue. The reverse doped samples were brown/orange at every stage.

## 2.3 Analytical Techniques

### 2.3.1 X-ray diffraction

#### 2.3.1.1 Introduction to XRD

About 95% of all solid materials can be described as crystalline. When x-rays interact with a crystalline substance (phase) a diffraction pattern is formed. In 1919 A. W. Hull presented a paper entitled, *A New Method of Chemical Analysis* [104]. He pointed out that '……**every crystalline substance gives a pattern; the same substance always gives the same pattern; and in a mixture of substances each produces its pattern independently of the others**.'

The x-ray diffraction (XRD) pattern of a pure substance is, therefore, akin to a fingerprint of the substance. The powder diffraction method is, thus, ideally suited for characterization and identification of polycrystalline phases. Today about 50,000 inorganic and 25,000 organic single components, crystalline phases, and diffraction patterns have been collected and stored on magnetic or optical media as standards. The main use of powder diffraction is to identify components in a sample by a search/match procedure. Furthermore, the areas under the peak are related to the amount of each phase present in the sample.

In day to day work we talk about x-ray reflections from a series of parallel planes inside the crystal. The orientation and interplanar spacings of these planes are defined by the three integers *h*, *k*, *l* called Miller indices. A given set of planes with indices *h*, *k*, *l* cut the *a*-axis of the unit cell in *h* sections, the *b* axis in *k* sections and the *c* axis in *l* sections. A zero indicates that the planes are parallel to the corresponding axis. For example, the (2, 2, 0) planes cut the *a*- and the *b*- axes in half, but are parallel to the *c*-axis as in Figure 2.5.

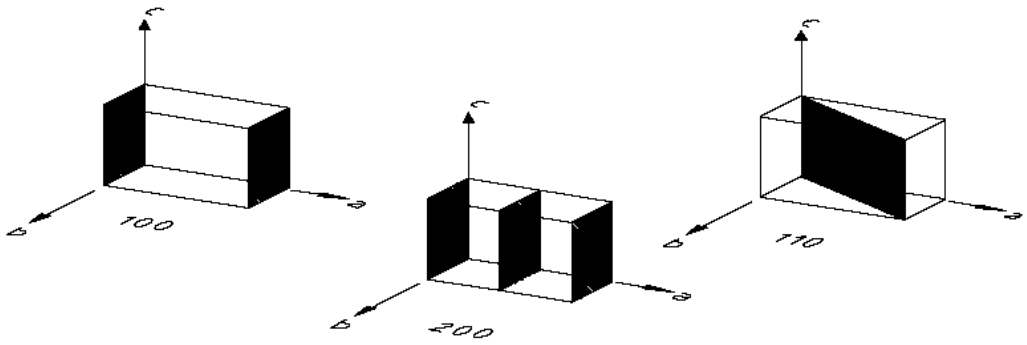


**Figure 2.5** The relation between the Miller indices and interplanes of the crystal.

Comparing the real diffraction patterns measured by XRD with the standard patterns form JCPDS (Joint Committee on Powder Diffraction Standards) database [105], the crystal structure, orientation, and Miller indices can be determined, and consequently, the crystalline phase substance can be identified accordingly. However, access to the other information contained in the pattern requires a more sophisticated technique. The first and (still major) unified technique for this purpose is Rietveld analysis [106].

Rietveld analysis is a comprehensive, computer based method for the analysis of powder diffraction patterns by least squares fittings of a calculated diffraction pattern to the raw observed data. H.M. Rietveld originally conceived it for studying neutron powder diffraction data, where the diffraction pattern contained many overlapping reflections due to low symmetry phases, or very large unit cells [107]. Since then, there have been major advances including the adaptation to the technique of X-Ray powder diffraction, and the facility to refine the structure of multiple phases simultaneously, and quantitative phase analysis.

A model of the material being analysed must be constructed from a preliminary analysis of the data collected, the chemistry of the sample and any other information available. A calculated pattern is then constructed using the structure model and diffraction physics. Following this, the model is optimised by least-squares refinement

of the variable parameters until suitable agreement between the data and the calculated pattern is obtained.

#### 2.3.1.2 Bragg's Law

English physicists Sir W.H. Bragg and his son Sir W.L. Bragg developed a relationship in 1913 to explain why the cleavage faces of crystals appear to reflect x-ray beams at certain angles of incidence (theta, $\theta$). The variable $d$ is the distance between atomic layers in a crystal, and the variable lambda, $\lambda$, is the wavelength of the incident x-ray beam; n is an integer. This observation is an example of x-ray wave interference, commonly known as X-ray diffraction (XRD), and provides direct evidence for the periodic atomic structure of crystals postulated for several centuries.

An electron in an alternating electromagnetic field will oscillate with the same frequency as the field. When an x-ray beam hits an atom, the electrons around the atom start to oscillate with the same frequency as the incoming beam and the X-Ray scatters. Scattered X-Rays from various parts in a random solid will, in almost all cases, be subject to destructive interference, that is, the combining waves are out of phase and there is no resultant energy leaving the solid sample. However, the atoms in a crystal are arranged in a regular pattern, and in very few directions constructive interference can occur. The waves will be in phase and there will be a well-defined x-ray beam leaving the sample at various directions. Hence, a diffracted beam may be described as a beam composed of a large number of scattered rays mutually reinforcing one another as shown in Figure 2.6.

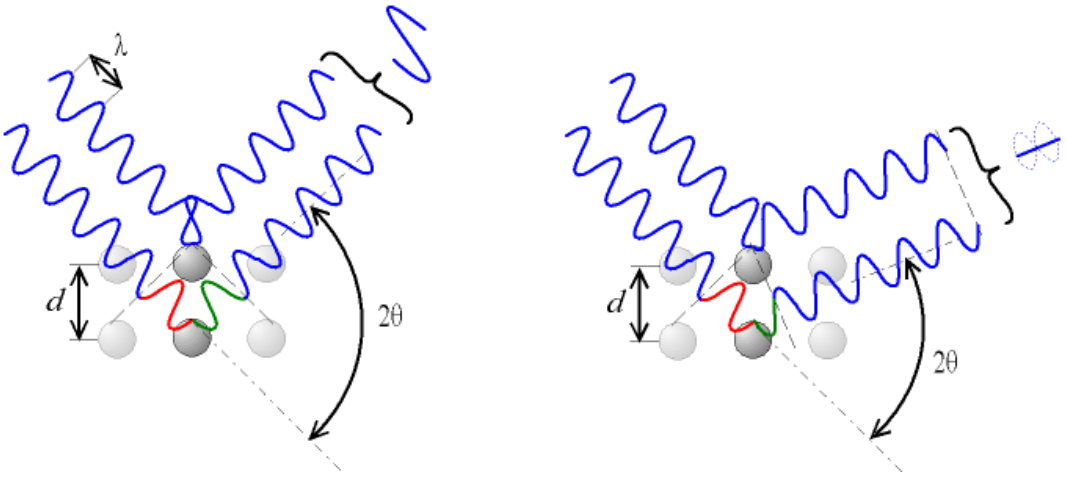


**Figure 2.6** The phase shift causes constructive (left) or destructive (right) interferences due to the 2θ deviation.

A single monochromatic wave, of any type, is incident on aligned planes of lattice points, with separation *d*, at angle *θ*, as shown below (Figure 2.7). A path difference between the 'ray' that which is reflected along **AC'** and the ray exists and then reflected along **AB** and **BC** paths exists. This path difference is:

$$(AB + BC) - (AC')$$

If this path difference is equal to any integer value of the wavelength then the two separate waves will arrive at a point with the same phase, and hence undergo constructive interference. Expressed mathematically:

$$(AB + BC) - (AC') = n\lambda$$

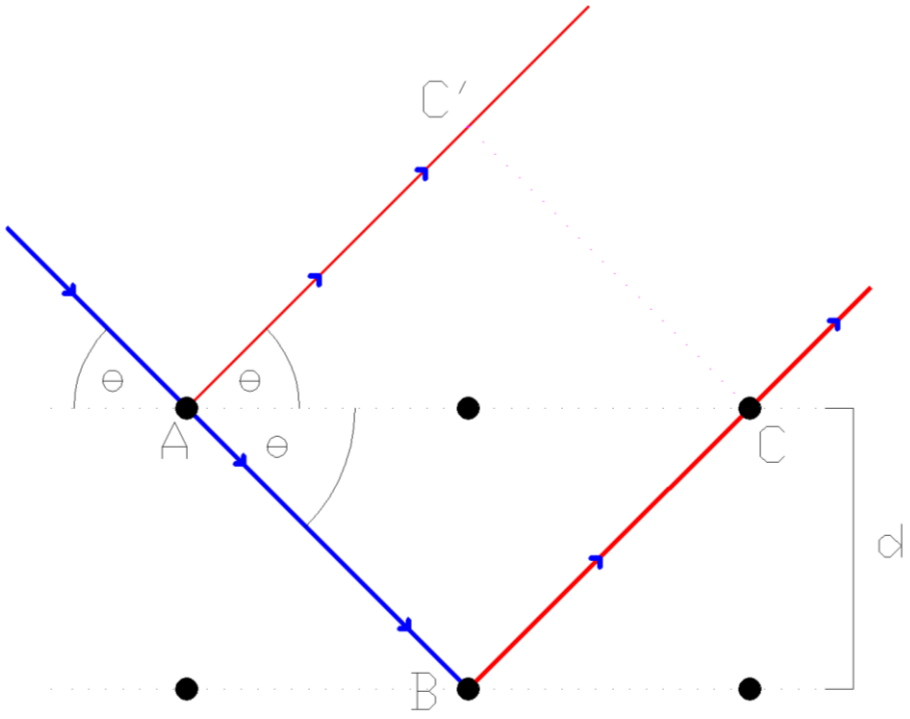


**Figure 2.7** Deriving Bragg's Law using the reflection geometry and applying trigonometry.

Using Pythagorean theorem it is easily shown that:

$$AB = \frac{d}{\sin\theta}\,, \quad BC = \frac{d}{\sin\theta}\,, \quad AC = \frac{2d}{\tan\theta}$$

Also, it can be shown that:

$$AC' = AC \cdot \cos\theta = \frac{2d}{\tan\theta}\cos\theta$$

Putting everything together and using known identities for sinusoidal functions:

$$n\lambda = \frac{2d}{\sin\theta} - \frac{2d}{\tan\theta}\cos\theta = \frac{2d}{\sin\theta}(1-\cos^2\theta) = \frac{2d}{\sin\theta}\sin^2\theta$$

Which simplifies to:

$n\lambda = 2d \cdot \sin\theta$ (Bragg's law).

XRD is used in two main areas, for the fingerprint characterization of crystalline materials, and the determination of their structure. Each crystalline solid has its unique characteristic x-ray pattern which may be used as a 'fingerprint' for its identification.

#### 2.3.1.3 X-ray diffractometer and the samples

However, a fingerprint diffraction of identifiable good quality is determined by two factors:

1. the diffractometer system
2. the sample

The X-ray diffractometer employed in this project is a Phillips Xpert MPD diffractometer using Cu *Kα* radiation incorporating a nickel mask to eliminate *Kβ* radiation, working voltage is 40 kV. A knife edge was held at about 0.5 mm above the centre of the sample to reduce scatter. The system utilizes the Xpert Data Organizer Software Suite and JCPDS reference database.

In X-ray diffraction work it is normal to distinguish between single crystal and polycrystalline or powder applications. The single crystal sample is a perfect (all unit cells aligned in a perfect extended pattern) crystal with a cross section of about 0.3 mm. The single crystal diffractometer and associated computer package is used

primarily to elucidate the molecular structure of novel compounds, either natural products or man made molecules. Powder diffraction is used for "fingerprint identification" of various solid materials. In powder or polycrystalline diffraction it is important to have a sample with a smooth surface. If possible, the sample is ground to particles of about several microns. The ideal sample is homogeneous and the crystallites are randomly distributed. The sample is pressed into a sample holder so that a smooth flat surface is creased.

Ideally, samples have a random distribution of all possible *h*, *k*, *l* planes. Only crystallites having reflecting planes (*h*, *k*, *l*) parallel to the specimen surface will contribute to the reflected intensities. If a truly random sample is present the possible reflection from a given set of *h*, *k*, *l* planes will have an equal number of crystallites contributing to it. In the steady conditions, the sample is stationary in the horizontal position while the x-ray tube and the detector both move simultaneously over the angular range theta during the analysis.

In this work it was necessary to measure small changes in lattice parameter, i.e. peak position. The exact position of the sample surface can affect the accuracy. In several cases, zirconia was added to the samples to act as an internal reference.

#### 2.3.1.4 X-ray photoelectron spectroscopy

X-ray photoelectron spectroscopy (XPS) is a quantitative spectroscopic technique that ideally can measure the empirical formula, chemical state and electronic state of the elements that exist within a material. XPS spectra are obtained by irradiating a material with a beam of X-rays while simultaneously measuring the kinetic energy (KE) and number of electrons that escape from the top 1 to 10 nm of the material being analyzed. XPS requires ultra-high vacuum (UHV) conditions.

XPS is a surface chemical analysis technique that can be used to analyze the chemistry of the surface of a material in its ‘as received’ state, or after treatment such as: fracturing, cutting or scraping in air or UHV to expose the bulk chemistry. Ion beam etching to remove surface contamination, exposure to heat to study the changes due to heating, exposure to reactive gases or solutions, exposure to ion beam implant, exposure to UV light as shown in Figure 2.8.

XPS can be used to measure:

- elemental composition of the surface (1–10 nm depth usually)
- elemental composition
- surface contamination
- chemical or electronic state of each element in the surface
- 2D elemental surface mapping
- uniformity of elemental composition from its surface to bulk via ion beam etching.

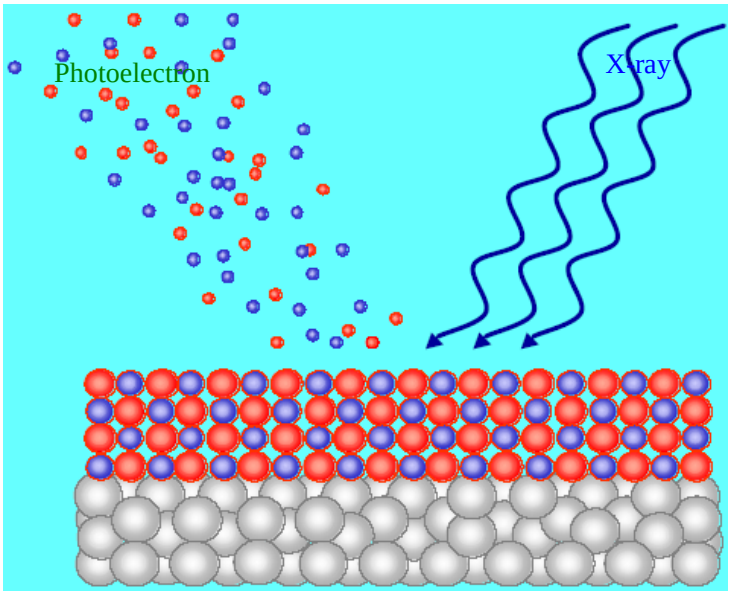


**Figure 2.8** The schematic relation of X-ray photons and emitted photoelectrons on the surface layer of the samples.

Because the energy of a particular X-ray wavelength equals a known quantity, the electron binding energy (BE) of emitted electrons can be determined by use of an equation based on the work of Ernest Rutherford (1914):

$$E_{binding} = E_{photon} - E_{kinetic} - \Phi$$

where $E_{binding}$ is the energy of the electron emitted from one electron configuration within the atom, $E_{photon}$ is the energy of the X-ray photons being used, $E_{kinetic}$ is the kinetic energy of the emitted electron as measured by the instrument and $\Phi$ is the work function of the spectrometer. The emission process is demonstrated below in Figure 2.9. The typical components of a XPS system are outlined below in Figure 2.10.

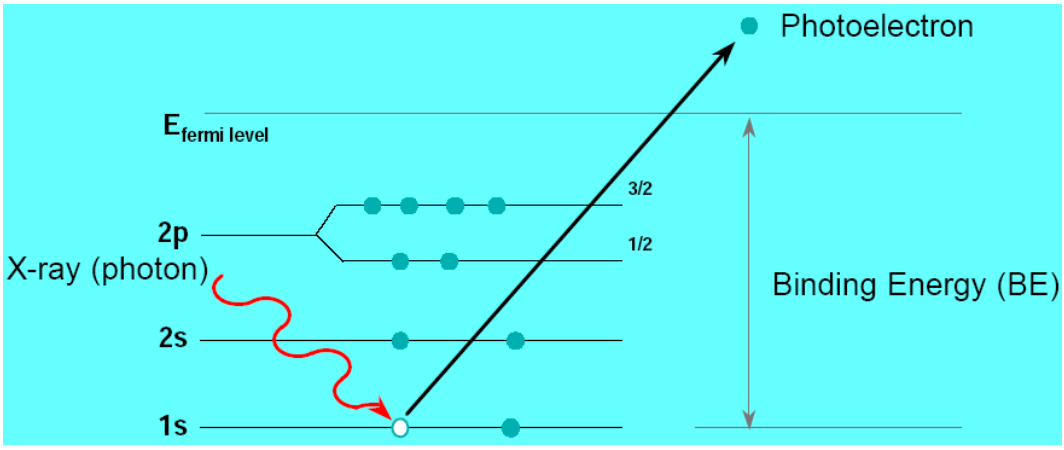


**Figure 2.9** The emission process of photoelectrons excited by incident x-rays. [108]

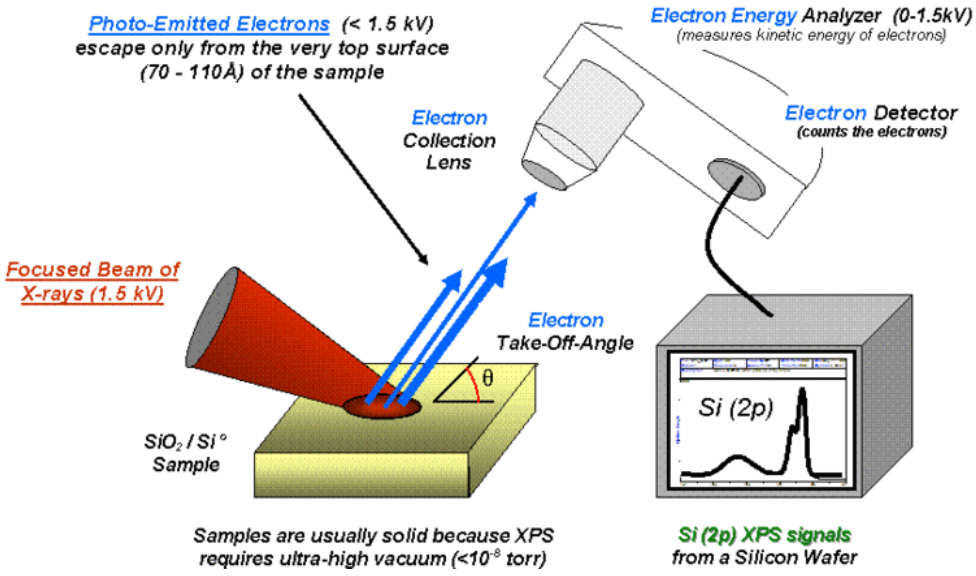


**Figure 2.10** The basic components of a XPS system. [109]

A typical XPS spectrum is a plot of the number of electrons detected versus the binding energy of the electrons detected. Each element produces a characteristic set of XPS peaks at characteristic core-level binding energy values that directly identify each element at the surface of the material being analyzed. These characteristic peaks correspond to the electron configuration of the electrons within the atoms, e.g., 1s, 2s, 2p, etc. The intensity of the characteristic peaks is directly proportional to the amount of element within the area (volume) irradiated. To generate atomic percentage values, each raw XPS signal must be corrected using a 'relative sensitivity factor' (RSF) and normalized over all of the elements detected.

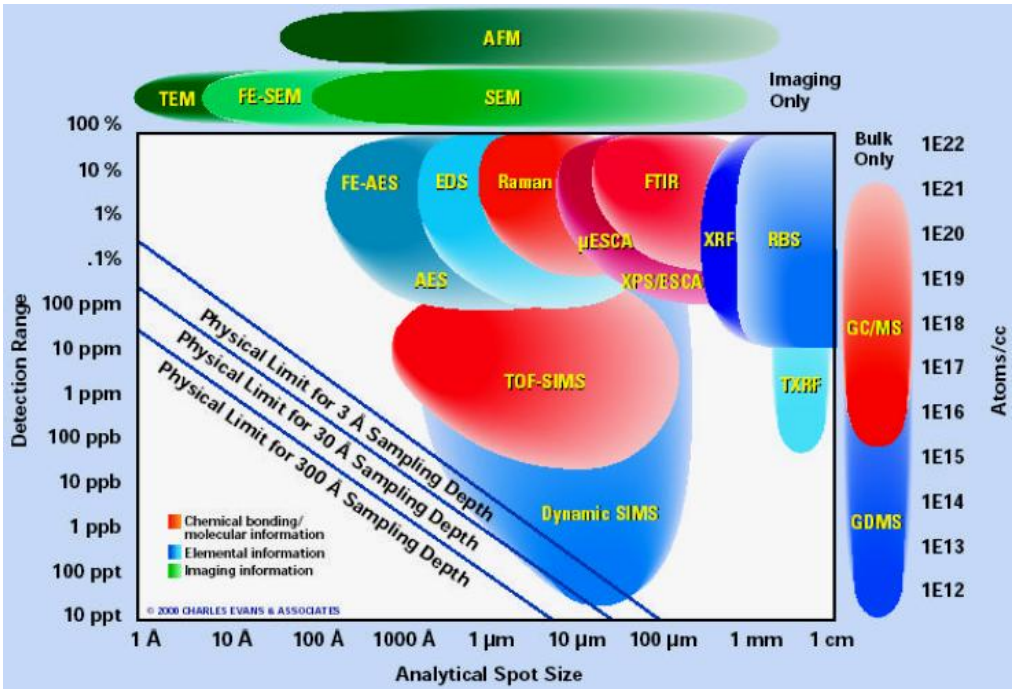


**Figure 2.11** Analytical resolution versus detection limits. [110]

To count the number of electrons at each KE value, with the minimum of error, XPS must be performed under ultra-high vacuum (UHV) conditions because electron counting detectors in XPS instruments are typically around 1m away from the material irradiated with x-rays.

It is important to note that XPS detects only those electrons that have actually escaped into the vacuum of the instrument, i.e. the photo-emitted electrons that originated from the top 10 to 12 nm of the material. All of the deeper photo-emitted electrons, which were generated as the X-rays penetrated 1–5 micrometers of the material, are either recaptured or trapped in various excited states within the material. For most applications, it is, in effect, a non-destructive technique that measures the surface chemistry of any material.

However, the detection limits is about 0.1–1.0 atom % (0.1 atom% = 1 part per thousand (PPTh) = 1,000 PPM) and the ultimate detection limit for most elements is

approximately 100 ppm, as per Figure 2.11. In this work, a high performance AXIS 165 X-ray photoelectron spectrometer was used for data collection and finely ground dry powder samples were mounted on conductive tape in the experiments.

### 2.3.2 Microscopy

An electron microscope uses electrons to illuminate and create an image of a specimen. It has much higher magnification and resolving power than a light microscope, with magnifications up to about two million times (compared to about two thousand for a conventional light microscope) allowing it to see smaller objects at greater detail. Unlike a light microscope, which uses glass lenses to focus light, the electron microscope uses electrostatic and electromagnetic lenses to control the illumination and imaging of the specimen.

#### 2.3.2.1 Transmission Electron Microscopy

The Transmission Electron Microscope (TEM) was invented in the early 1930's in Berlin [111, 112, 113]. TEM is an imaging technique where a beam of electrons is transmitted through a specimen forming a magnified image at a fluorescent screen or a layer of photographic film. Recently, sensitive CCD cameras have become the method of choice.

TEM is used heavily in both material science/metallurgy and the biological sciences. In both cases the specimens must be very thin and able to withstand the high vacuum present inside the instrument. In material science/metallurgy the specimens tend to be naturally resistant to vacuum, but must be prepared as thin foils, or etched so that a portion of the specimen is thin enough for the beam to penetrate. Preparation techniques to obtain an electron transparent region include ion beam milling and wedge polishing. The focused ion beam (FIB) method is a relatively new technique to

prepare thin samples for TEM examination from larger specimens. Because the FIB can be used to micro-machine samples very precisely, it is possible to mill very thin membranes from a specific area of a sample, such as a semiconductor or metal. Materials that have dimensions small enough to be electron transparent, such as nano dimensional powders or nanotubes, can be quickly produced by the deposition of a dilute sample containing the specimen onto support grids. The suspension is normally a volatile solvent, such as ethanol, ensuring that the solvent rapidly evaporates allowing a sample that can be rapidly analyzed.

The contrast in a TEM image is not like the contrast in a light microscope image. A crystalline material interacts with the electron beam mostly by diffraction rather than absorption, although the intensity of the transmitted beam is still affected by the volume and density of the material through which it passes. The intensity of the diffraction depends on the orientation of the planes of atoms in a crystal relative to the electron beam; at certain angles the electron beam is diffracted strongly from the axis of the incoming beam, while at other angles the beam is largely transmitted. Modern TEMs are often equipped with specimen holders that allow the user to tilt the specimen to a range of angles in order to obtain specific diffraction conditions and apertures placed below the specimen allow the user to select electrons diffracted in a particular direction.

A high-contrast image can, therefore, be formed by blocking electrons deflected away from the optical axis of the microscope by placing the aperture to allow only unscattered electrons through. This produces a variation in the electron intensity that reveals information on the crystal structure.

This technique (known as *Bright Field* or *Light Field*) is particularly sensitive to extended crystal lattice defects in an otherwise ordered crystal, such as dislocations. As the local distortion of the crystal around the defect changes the angle of the crystal

plane, the intensity of the scattering will vary around the defect, as the image is formed by the distortion of the crystal planes around the defect.

It is also possible to produce an image from electrons deflected by a particular crystal plane. By either moving the aperture to the position of the deflected electrons, or tilting the electron beam so that the deflected electrons pass through the centred aperture, an image can be formed of only deflected electrons, known as a *Dark Field* image.

In this work, all samples were dispersed into organic solvents, e.g. ethanol, toluene etc. and a few drops of the above solutions were transferred to the holey carbon film on copper grids (400 meshes) and dried under ambient atmosphere at room temperature overnight. TEM observations were carried out in JEM-2011 and JEM-2000FX electron microscopes operating at 200 kV. The images were collected and treated by the associated or freeware software packages, e.g. Gatan and ImageJ software packages.

#### 2.3.2.2 Scanning Electron Microscopy

The scanning electron microscope (SEM) is a type of electron microscope capable of producing high-resolution images of a sample surface. Due to the manner in which the image is created, SEM images have a characteristic three-dimensional appearance and are useful for judging the surface structure of the sample.

In a typical SEM, electrons are thermionically emitted from a tungsten or lanthanum hexaboride ($LaB_6$) cathode and are accelerated towards an anode; alternatively, more acute electron beams can be emitted via field emission (FE) [114, 115]. Tungsten is used because it has the highest melting point and lowest vapour pressure of all metals, thereby allowing it to be heated for electron emission. The electron beam, which typically has an energy ranging from a few hundred eV to 100 keV, is focused by one

or two condenser lenses into a beam with a very fine focal spot sized 1 nm to 5 nm. The beam passes through pairs of scanning coils in the objective lens, which deflect the beam horizontally and vertically so that it scans in a raster fashion over a rectangular area of the sample surface. When the primary electron beam interacts with the sample, the electrons lose energy by repeated scattering and absorption within a teardrop-shaped volume of the specimen known as the interaction volume, which extends from less than 100 nm to around 5 μm into the surface. The size of the interaction volume depends on the beam accelerating voltage, the atomic number of the specimen and the specimen's density. The energy exchange between the electron beam and the sample results in the emission of electrons and electromagnetic radiation which can be detected to produce an image, as described below.

The most common imaging mode monitors low energy (<50 eV) secondary electrons. Due to their low energy, these electrons originate within a few nanometers from the surface. The electrons are detected by a scintillator-photomultiplier device and the resulting signal is rendered into a two-dimensional intensity distribution that can be viewed and saved as a digital image. This process relies on a raster-scanned primary beam. The brightness of the signal depends on the number of secondary electrons reaching the detector. If the beam enters the sample perpendicular to the surface, then the activated region is uniform about the axis of the beam and a certain number of electrons ‘escape’ from within the sample. As the angle of incidence increases, the ‘escape’ distance of one side of the beam will decrease and more secondary electrons will be emitted. Thus, steep surfaces and edges tend to be brighter than flat surfaces, which results in images with a well-defined, three-dimensional appearance. Using field emission sources technique, resolutions less than 1 nm are possible.

However, the imaging can also be obtained from backscattered electrons (BSE). Backscattered electrons consist of high-energy electrons originating in the electron beam, which are reflected or back-scattered out of the specimen interaction volume. Backscattered electrons may be used to detect contrast between areas with different

chemical compositions, especially when the average atomic number of the various regions is different, since the brightness of the BSE image tends to increase with the atomic number. There are fewer backscattered electrons emitted from a sample than secondary electrons. The number of backscattered electrons leaving the sample surface upward might be significantly lower than those that follow trajectories toward the sides.

X-rays, which are also produced by the interaction of electrons with the sample, may also be detected in an SEM equipped for energy-dispersive X-ray spectroscopy (EDX) or wavelength dispersive X-ray spectroscopy (WDX).

The preparation of samples is relatively easy compared to that for TEM. A small quantity of dilute dry samples was adhered to the surface of a piece of conductive double-sided sticky carbon-coated tape which contacts tightly with the aluminium stubs (diameter 12 mm). For the samples on the silicon wafers, the procedure is the same. The samples were coated on the surface of the Si wafer, and the carbon-coated adhesive tape connects both the down-side of the Si wafer and the aluminium stubs (diameter 35 mm) tightly. However, in order to improve the electrical conductivity and therefore obtain better images, gold-coating was used periodically. The gold-coating was operated in 3 cycles of repeated evacuation and flushing with argon gas and then coating. The SEM used here was a JSM-5510 electron microscope using a beam voltage 5~10 kV.

### 2.3.3 Nitrogen Sorption Measurements

Gas adsorption measurements are widely used for determining the surface area and pore size distribution of a variety of different solid materials, e.g. industrial adsorbents, catalysts, pigments, ceramics and building materials. The measurement of adsorption at the gas/solid interface also forms an essential part of most fundamental and applied investigations of the nature and behaviour of solid surfaces.

Adsorption (in the present context, positive adsorption at the gas/solid interface) is the enrichment of one or more components in an interfacial layer. Physisorption (as distinct from chemisorption) is a general phenomenon: it occurs whenever an adsorbable gas (the adsorptive) is brought into contact with the surface of a solid (the adsorbent). The intermolecular forces involved are of the same kind as those responsible for the imperfection of real gases and the condensation of vapours. With some adsorption systems, certain specific molecular interactions occur (e.g. polarisation, field-dipole, field gradient-quadruple), arising from particular geometric and electronic properties of the adsorbent and adsorptive. The term adsorption may also be used to denote the process in which adsorptive molecules are transferred from the gas phase to, and accumulate in, the interfacial layer. Its counterpart, desorption, denotes the reverse process, i.e. the decrease in the amount of adsorbed substance. Adsorption and desorption are often used adjectivally to indicate the direction from which experimentally determined adsorption values have been approached, e.g. the adsorption curve (or point) and the desorption curve (or point). Adsorption hysteresis arises when the adsorption and desorption curves deviate from one another.

The many different procedures which have been devised for the determination of the amount of gas adsorbed may be divided into two groups:

a) those which depend on the measurement of the amount of gas leaving the gas phase (i.e. gas volumetric methods) and
b) those which involve the measurement of the uptake of the gas by the adsorbent (e.g. direct determination of increase in mass by gravimetric methods).

In the static volumetric determination a known quantity of gas is usually admitted to a confined volume containing the adsorbent, maintained at constant temperature. As adsorption takes place, the pressure in the confined volume falls until equilibrium is established. The amount of gas adsorbed at the equilibrium pressure is given as the difference between the amount of gas admitted and the amount of gas required to fill

the space around the adsorbent, i.e. the dead space, at the equilibrium pressure. The adsorption isotherm is constructed point-by-point by the admission to the adsorbent of successive charges of gas with the aid of a volumetric dosing technique and application of the gas laws. The volume of the dead space must, of course, be known accurately: it is obtained either by pre-calibration of the confined volume and subtracting the volume of the adsorbent (calculated from its density), or by the admission of a gas which is adsorbed to a negligible extent. Nitrogen adsorption isotherms at the temperature of the boiling point of nitrogen at ambient atmospheric pressure are generally determined by the volumetric method and provide the basis for the various standard procedures which have been proposed for the determination of surface area [116].

Prior to the determination of an adsorption isotherm, most if not all of the physisorbed species must be removed from the surface of the adsorbent. This may be achieved by outgassing (degassing), i.e. exposure of the surface to a high vacuum - usually at elevated temperature. The outgassing conditions (temperature programme, change in pressure over the adsorbent and the residual pressure) required to attain reproducible isotherms must be controlled to within limits which are dependent on the adsorption system. Instead of exposing the adsorbent to a high vacuum, it is sometimes expedient to achieve adequate cleanliness of the surface by flushing the adsorbent with an inert gas (which may be the adsorptive) at elevated temperature. With certain microporous solids reproducible isotherms are only obtained after one or more adsorption-desorption cycles. This problem can be overcome by flushing with the adsorptive and subsequent heating in vacuum.

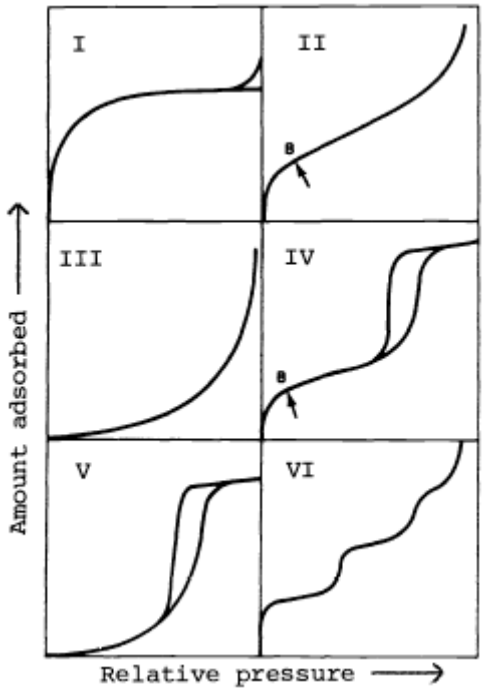


**Figure 2.12** Types of physisorption isotherms (reprinted from ref. [114]).

The majority of physisorption isotherms may be grouped into the six types shown in Figure 2.12.

The reversible **Type I isotherm** is given by microporous solids having relatively small external surfaces (e.g. activated carbons, molecular sieve zeolites and certain porous oxides), the limiting uptake being governed by the accessible micropore volume rather than by the internal surface area.

The reversible **Type II isotherm** is the normal form of isotherm obtained with a non-porous or macroporous adsorbent. The Type II isotherm represents unrestricted monolayer-multilayer adsorption. Point B, the beginning of the almost linear middle section of the isotherm, is often taken to indicate the stage at which monolayer coverage is complete and multilayer adsorption is about to begin.

The reversible **Type III isotherm** is convex to the $p/p^0$ axis over its entire range and, therefore, does not exhibit a Point B. Isotherms of this type are not common; the best known examples are found with water vapor adsorption on pure non-porous carbons.

However, there are a number of systems (e.g. nitrogen on polyethylene) which give isotherms with gradual curvature and an indistinct Point B. In such cases, the adsorbent-adsorbate interaction is weak as compared with the adsorbate-adsorbate interactions.

Characteristic features of the **Type IV isotherm** are the hysteresis loop, which is associated with capillary condensation taking place in mesopores, and the limiting uptake over a range of high $p/p^0$. The initial part of the Type IV isotherm is attributed to monolayer-multilayer adsorption since it follows the same path as the corresponding part of a Type II isotherm obtained with the given adsorptive on the same surface area of the adsorbent in a non-porous form. Type IV isotherms are given by many mesoporous industrial adsorbents.

The **Type V isotherm** is uncommon; it is related to the Type III isotherm in that the adsorbent-adsorbate interaction is weak, but is obtained with certain porous adsorbents.

The **Type VI isotherm** represents stepwise multilayer adsorption on a uniform non-porous surface. The step-height now represents the monolayer capacity for each adsorbed layer and, in the simplest case, remains nearly constant for two or three adsorbed layers. Amongst the best examples of Type VI isotherms are those obtained with argon or krypton on graphitized carbon blacks at liquid nitrogen temperature.

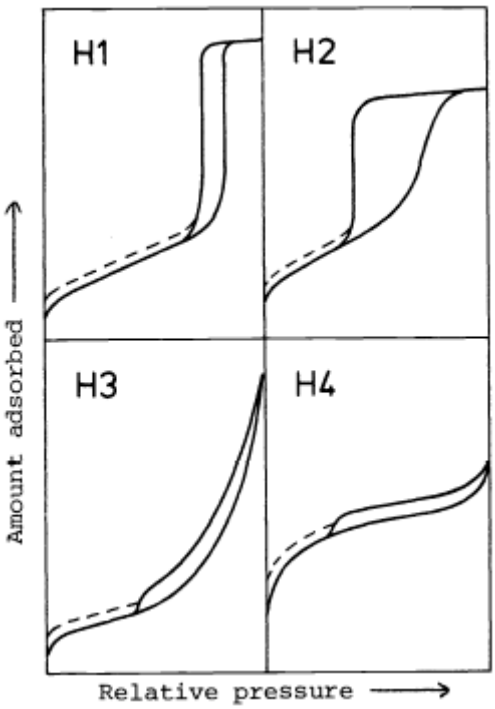


**Figure 2.13** Types of hysteresis loops (reprinted from ref. [114]).

Hysteresis appearing in the multilayer range of physisorption isotherms is usually associated with capillary condensation in mesopore structures. Such hysteresis loops may exhibit a wide variety of shapes. Two extreme types are shown as H1 and H4 in Figure 2.13. In the former the two branches are almost vertical and nearly parallel over an appreciable range of gas uptake, whereas in the latter they remain nearly horizontal and parallel over a wide range of $p/p^0$. In certain respects Types H2 and H3 may be regarded as intermediate between these two extremes. A feature common to many hysteresis loops is that the steep region of the desorption branch leading to the lower closure point occurs (for a given adsorptive at a given temperature) at a relative pressure which is almost independent of the nature of the porous adsorbent.

The shapes of hysteresis loops have often been identified with specific pore structures. Thus, Type H1 is often associated with porous materials known, from other evidence,

to consist of agglomerates or compacts of approximately uniform spheres in fairly regular array and, hence, to have narrow distributions of pore size. Some corpuscular systems (e.g. silica gels) tend to give Type H2 loops, but in these cases the distribution of pore size and shape is not well-defined. Indeed, the H2 loop is especially difficult to interpret: in the past it was attributed to a difference in mechanism between condensation and evaporation processes occurring in pores with narrow necks and wide bodies (often referred to as 'ink bottle' pores), but it is now recognised that this provides an over-simplified picture.

The Type H3 loop, which does not exhibit any limiting adsorption at high $p/p^0$, is observed with aggregates of plate-like particles giving rise to slit-shaped pores. Similarly, the Type H4 loop appears to be associated with narrow slit-like pores, but in this case the Type I isotherm character is indicative of microporosity.

With many systems, especially those containing micropores, low pressure hysteresis (indicated by the dashed lines in Figure 2.13), may be observed extending to the lowest attainable pressures. Removal of the residual adsorbed material is then possible only if the adsorbent is outgassed at higher temperatures. This phenomenon is thought to be associated with the swelling of a non-rigid porous structure or with the irreversible uptake of molecules in pores (or through pore entrances) of about the same width as that of the adsorbate molecule.

Nitrogen sorption measurements of all samples were carried out using a Micromeritics Gemini 2375 volumetric analyzer (Micromeritics Instrument Corporation, U.K) at 77 K. The samples were outgassed at 110~200 °C for 4 hours above under flowing nitrogen prior to measurement. Specific area and pore size distribution were calculated by Brunauer-Emmett-Teller (BET) [ 117 ] and Barrett-Joyner-Halenda (BJH) [118] methods respectively.

# 3 Chapter 3 - Lattice Constant Dependence on Particle Size for Ceria prepared from an acid precipitation-peptisation gel.

This chapter is based on a paper presented at EMAG-NANO 2005: Imaging, Analysis and Fabrication on the Nanoscale, University of Leeds, August 2005. It has been published as part of the Journal of Physics: Conference Series 26 (2006) 119-122.

## 3.1 Abstract

High surface area ceria nano-particles have been prepared using a citrate sol-gel precipitation method. Changes to the particle size have been made by calcining the ceria powders at different temperatures. X-ray diffraction methods were used to determine their lattice parameters. The particles sizes were also assessed using transmission electron microscopy (TEM), scanning electron microscopy (SEM), and BET, and, the lattice parameter was found to decrease with decreasing particle size. The results are discussed in light of the role played by surface tension effects.

## 3.2 Introduction

Ceria (and doped ceria) has become one of the most important ceramic materials. It has a number of important and varied catalysis uses (most notably as an important component of the three way automotive catalyst) [119], as an ionic conductor [120], as a gas sensor [121], and as an electrolyte material of solid oxide fuel cells [122]. Ceria thin films have also found uses as high refractive index materials and insulating films on semiconductors. Nanoparticles, in general, show higher catalytic activity and better sinterability, for example, in comparison with coarse grained bulk materials [123].

The defect chemistry of ceria is relatively well established. It is generally thought that as a trivalent cation is added to the lattice, its charge is compensated by the presence of anion vacancies. Such vacancies are associated with the dopant cations and are randomly distributed on anion sites within the fluorite lattice. In particular, whilst this maybe the thermodynamically the most important defect mechanism, other defect systems are possible as minority species [124] and experimental evidence for interstitial oxygen defects has been found for nanoparticles of ceria [125]. The change in lattice constant of ionic crystallites with decreasing nanoparticle size is an important issue that is not fully understood [126]. Tsunekawa *et al.* report lattice expansion with decreasing particle size for several nanosized $CeO_2$ particle preparations [127]. The results were from conventional electron diffraction performed in a TEM. Usually TEM diffraction patterns cannot provide the accuracy required of lattice parameter measurements, which need to be better than 0.5%. More definitive measurements of this changing lattice constant are presented here using x-ray diffraction.

There are numerous chemical methods for the production of nano-dimensioned particles of ceria. These include precipitation, sol-gel techniques, micellar controlled (nanoreactors) and oxidation. Most syntheses of ceria nanoparticles aim to provide spherical particles of high surface area, which are either non-agglomerated or weakly agglomerated. However, each preparation method will produce materials with different defect densities and morphologies and it is difficult to relate any changes to variations in particle dimensions. For this investigation, the citrate sol-gel precipitation-peptisation approach was employed, which yielded high surface area nanoparticulate materials.

## 3.3 Experimental Procedure

### 3.3.1 Synthesis of Bulk Ceria

Ceria nanoparticles were prepared via the precipitation-peptisation method using three different acids for comparison; citric acid, oxalic acid and nitric acid. For peptisation, crude bulk ceria had to be prepared. This was performed by firstly making up a 1 molar solution of cerium (III) nitratehexahydrate, $Ce(NO_3)_3.6H_2O$ ($M_r$ = 434.23 g). This was achieved by dissolving 43.423g of C $e(NO_3)_3.6H_2O$ crystals in deionised water in a 250 ml beaker. This solution was then carefully transferred to a 100 ml volumetric flask, where it was brought up to the calibration mark using de-ionised water. 100 ml of 1 M solution was poured into a 250 ml beaker. A stirrer bar was added to the beaker, which was then placed on a stirrer/ hot plate (at room temperature). A burette was then filled with 25 ml of ammonium hydroxide solution, which was slowly added to the solution in the beaker to precipitate the $CeO_2$ under constant stirring. This resulted in a thick yellow/ white emulsion, which was left stirring for 30 min before being vacuum dried in a Buchner funnel. Once dry, the brownish/ purple precipitate was scraped into a crucible and was placed for 24 hrs in the oven at 80 °C. On drying, the precipitate was lemon yellow in colour and was ground down to a fine powder using a pestle and mortar.

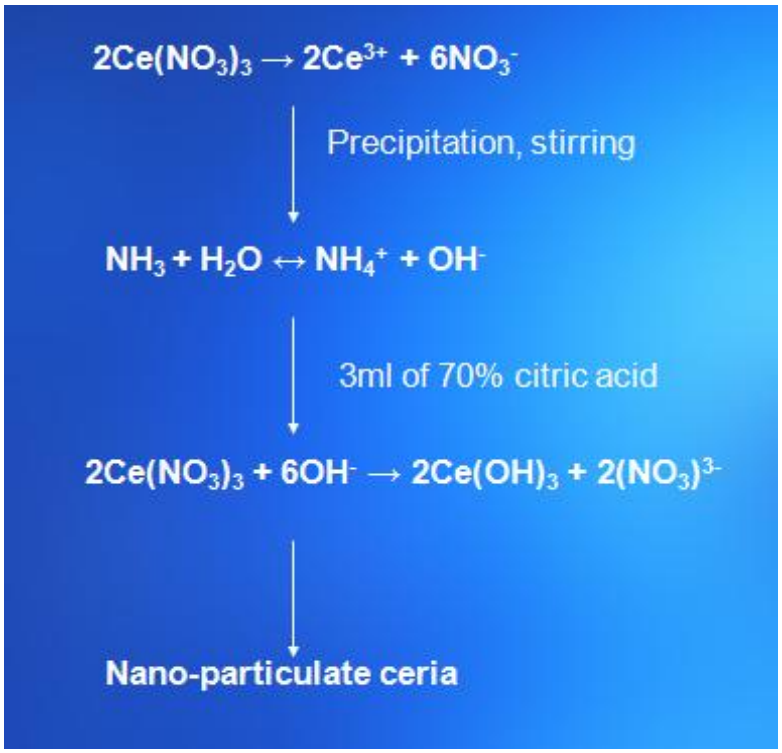


### 3.3.2 Synthesis of acid precipitation-peptisation gel samples

3 g of this bulk ceria powder was weighed out into a sample vial. 3 ml of 70% oxalic acid was then added to the vial using a micro pipette. A stirrer bar was placed in the solution and the vial was placed on a stirrer to stir overnight. This was repeated for 3 ml of 70% nitric acid and 3 ml of 70% citric acid, using 3 g of bulk ceria powder for each.

After stirring, the acid peptised emulsions were scraped into crucibles and placed in the oven overnight to dry at 80 °C. The ceria-citric acid emulsion was light brown in colour, while the oxalic acid emulsion was pale yellow and the nitric acid emulsion was a slightly darker yellow. The citric, oxalic and nitric emulsions dried to form cream, pale yellow and pale yellow/orange powders respectively. These powders were ground down and returned to their crucibles ready for calcination. The precipitation samples were calcined in the following temperature range, 250 °C to 1050 °C progressing in 50 °C increments, with a dwell time of 2 hrs. As the temperature

increased, all the ceria powder samples became uniform pale yellow in colour. At the higher temperatures, on removing the samples from the oven they were white in colour, however, they quickly assumed their pale yellow colour on cooling.

## 3.4 Analyses

Powder X-Ray diffraction (PXRD) patterns were recorded on a Phillips PW 3710 Xpert MPD diffractometer ($\theta$~$2\theta$ mode), equipped with a Cu Kα radiation source of wavelength 1.54 Å, incorporating a nickel mask to eliminate $K\beta$ radiation, standard scintillation detector, with an accelerating of 40 kV and an anode current of 30 mA. Data was collected over the range of 10 - 70° ($2\theta$), using a step size of 0.03°. Measurement of lattice parameters were not made by simple analysis of peak positions, but rather by using detailed Rietveld simulation studies where the position of the features were quantitatively matched in simulation by changing lattice spacings within the crystal framework. The Phillips Analytical Rietveld 1.0b software package used also permitted quantitative analysis of each phase present.

Crystallite size was calculated using the quantitative relationship between the crystal thickness t, diffraction peak maximum $\theta$ and the diffraction peak full width half maximum (FWHM) β, which is known as the Debeye-Scherrer equation:

$$t = K\lambda / \beta \cos \theta$$

All sizes are quoted for samples are an average result of 5 different reflections, between 25 - 60° $2\theta$.

The nitrogen adsorption and desorption isotherms at 77 K were measured using a Micromeritics Gemini 2375 volumetric analyzer (Micromeritics Instrument Corporation, U.K). All samples were degassed under the flow of ultra high grade 5.0

nitrogen at 200 °C for 4 hrs prior to each measurement.

Scanning electron micrographs (SEM) were recorded on a JSM-5510 apparatus (JEOL) using a beam voltage of 5 kV. Transmission electron microscopy (TEM) was used for structural characterization. Each powder was dispersed onto holey carbon support grids and examined at 200 kV in a JEOL 2000FX.

## 3.5 Results and Discussion

### 3.5.1 PXRD Analysis.

Figure 3.1 below shows the characteristic fluorite PXRD pattern for pure $CeO_2$, calcined in the temperature range of 350 °C to 950 °C. The characteristic cubic F*m*3*m* structure is observed, with the corresponding cubic unit cell parameters for ceria of a = b = c = 0.541134 nm. The X-ray diffraction analysis is made on the four main reflections found at $2\theta$ = 28.55° (111), 33.11° (200), 47.52° (202) and 56.37° (311), in agreement with the formation of fluorite-structured materials with a face centered cubic (fcc) cell [128]. At 550 °C the peaks are broad and not fully crystallized. After heating to 850 °C, the peaks are sharp and symmetrical, having crystallized in the F*m*3*m* space group and show no tendancy to form any other phases, regardless of age time, or temperature. The sharp reflections and high count values indicate large crystallite sizes and hence, strong sintering of the pure ceria particles with time and temperature.

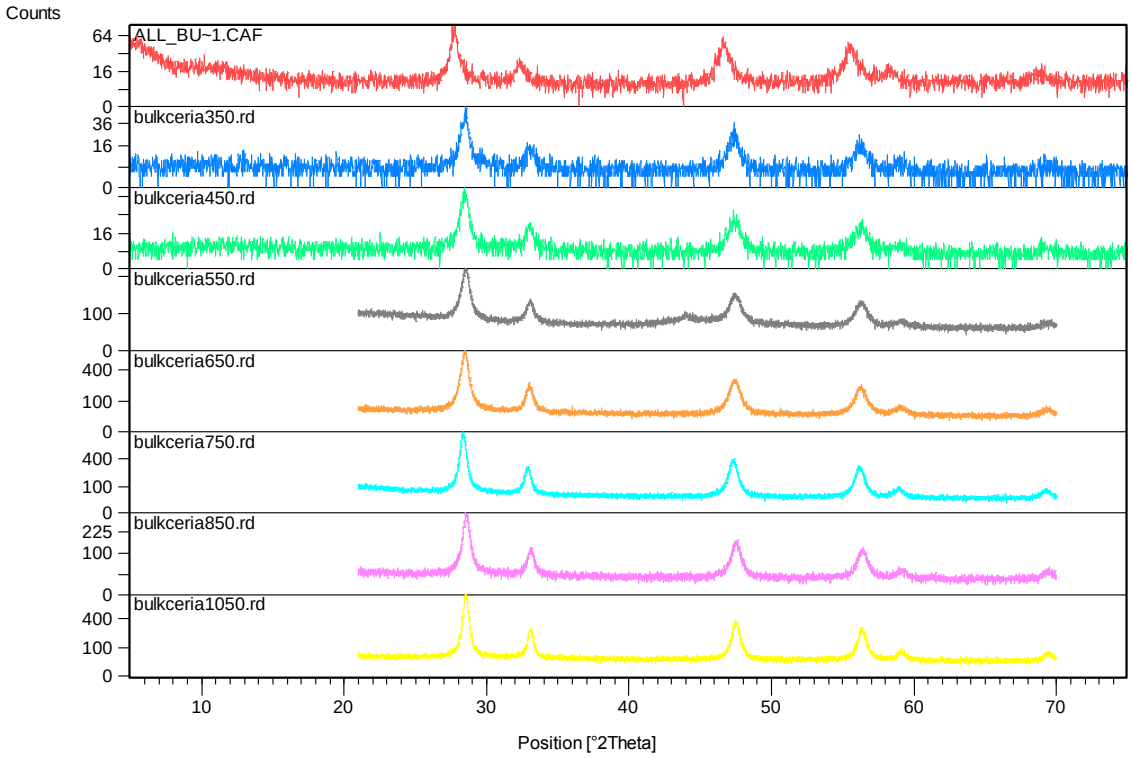


**Figure 3.1**: PXRD data of $CeO_2$ prepared by the citric acid precipitation-peptisation technique aged from 350 °C to 1050 °C, illustrating the flourite phase and the crystallization and sintering of particles with temperature and time.

Table 3.1 lists the parameters used to Rietveld fit the PXRD data, in the cubic F*m*3*m* space group.

**Table 3.1:** Rietveld parameters for $CeO_2$ cubic phase

| **Phase** | **Space Group** | **Lattice Parameter** | **Ion** | **Site** | **x** | **y** | **z** | **B/nm$^2$** | **N** |
|---|---|---|---|---|---|---|---|---|---|
| **Cubic** | Fm3m | a = b = c = 0.541143nm | $Ce^{4+}$ | 4e | 0 | 0 | 0 | 0.007 | 4.0 |
| **$CeO_2$** | Z = 4 | | $O^{2-}$ | 4e | 0.25 | 0.25 | 0.25 | 0.003 | 8.0 |

Figures 3.2 - 3.4 are PXRD 3D stacked plots for various temperatures (350 °C to 1050 °C) for oxalic, citric and nitric precipitation-peptisation preparatory methods. As stated previously, at high temperatures, ceria (of cubic fluorite structure), is susceptible to crystalline growth. Low temperature sintered ceria exhibits broad and low intensity PXRD peaks. Figure 3.5 is a PXRD 2D comparison plot of various temperatures (350 °C to 1000 °C) for the citric acid precipitated synthesis.

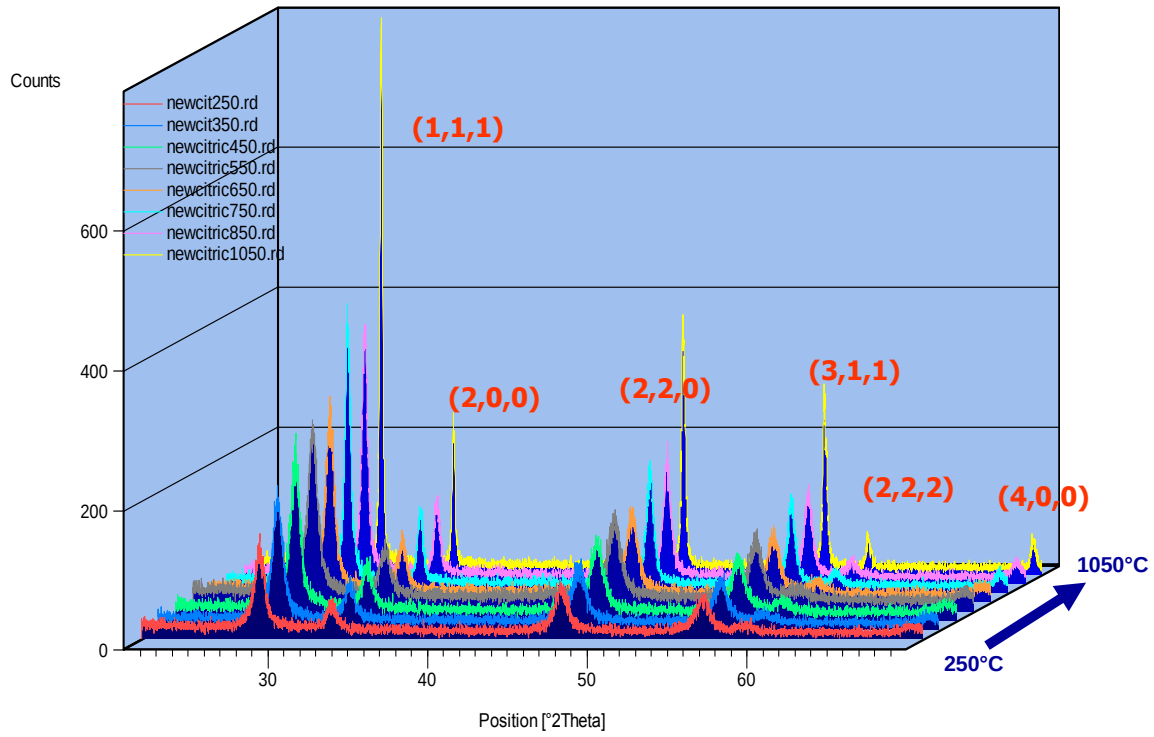


**Figure 3.2**: 3D PXRD stack plot as a function of temperature for the citric acid precipitation technique.

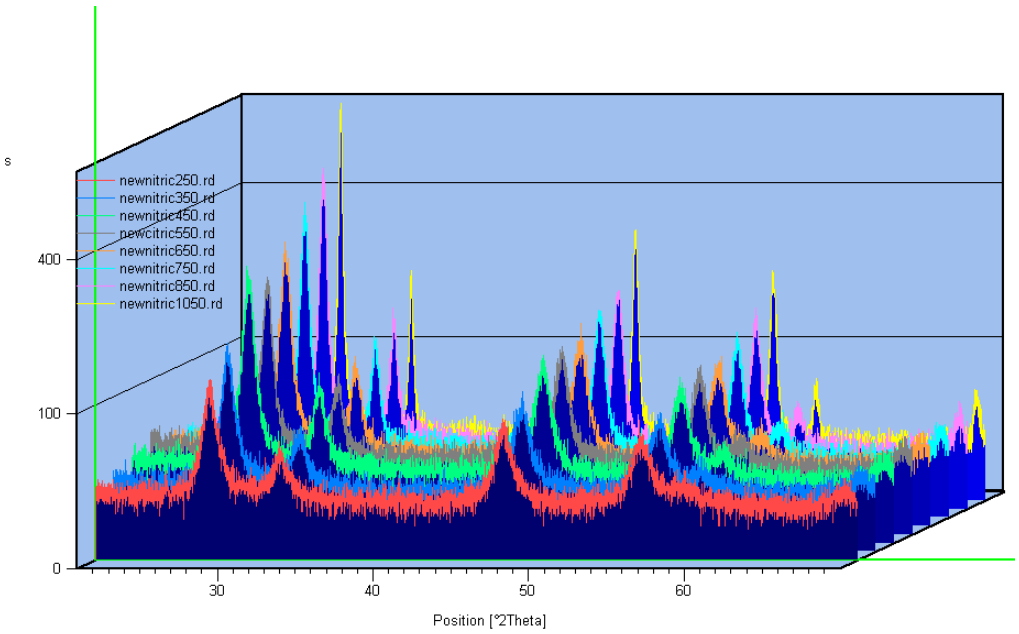


**Figure 3.3:** 3D PXRD stack plot as a function of temperature for the nitric acid precipitation technique.

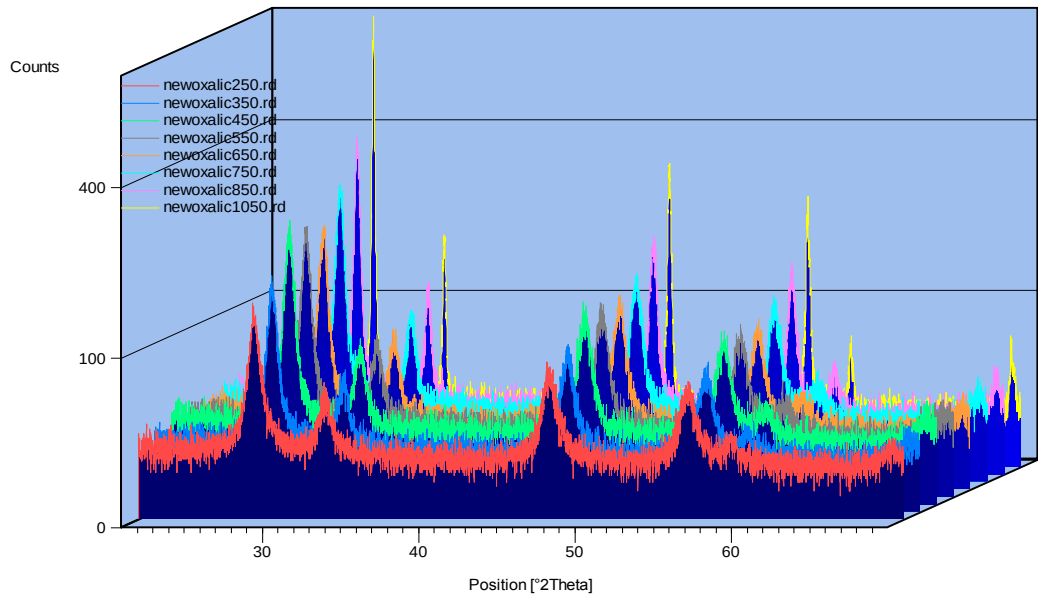


**Figure 3.4:** 3D PXRD stack plot as a function of temperature for the oxalic acid precipitation technique.

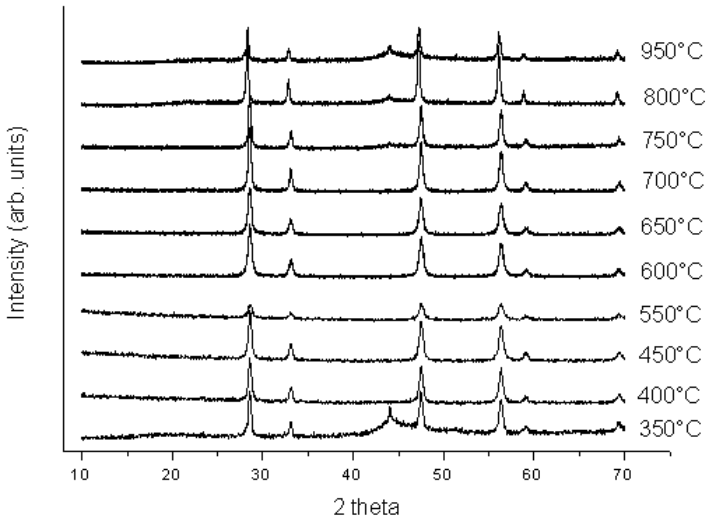


**Figure 3.5:** 2D PXRD comparison plot for citric acid technique

From these PXRD patterns, lattice parameter and particle size approximations were calculated using the Scherrer equation, as defined in section 3.2. Each figure exhibits similar heating trends in that the FWHM decreases, peak intensity increases and the (2,2,2) peak emerges as crystallization occurs

The expected lattice parameter for the ceria fluorite structure is 0.541134 nm. Low temperature ceria tends to exhibit higher lattice parameters, largely due to the presence of anion vacancy defects which result in lattice expansion. Such defects are introduced during sample preparation and vary according to method and reagents used. Figure 3.6 illustrates d-spacing as a function of sintering temperature, while Figure 3.7 illustrates how lattice parameter varies as a function of sintering temperature.

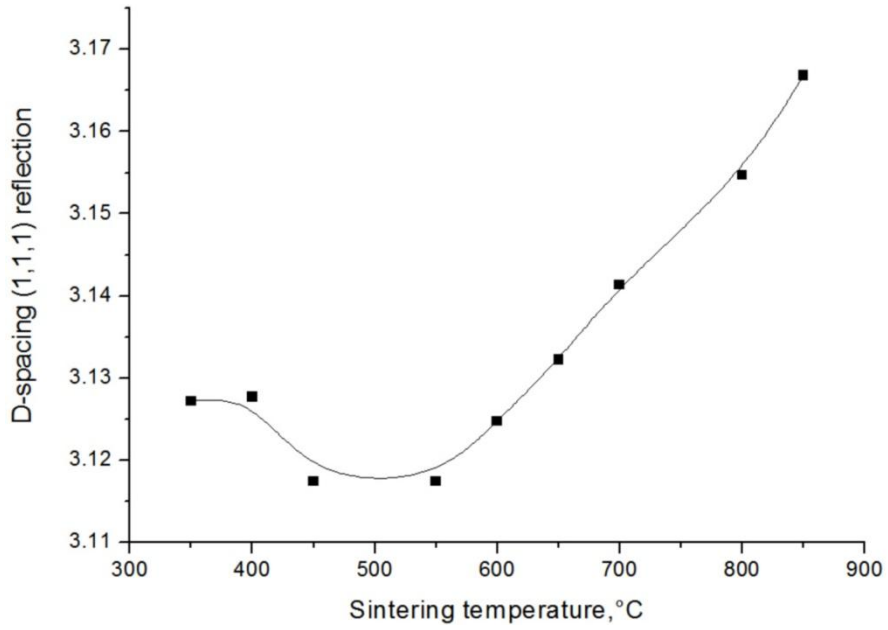


**Figure 3.6:** d-spacing as a function of sintering temperature

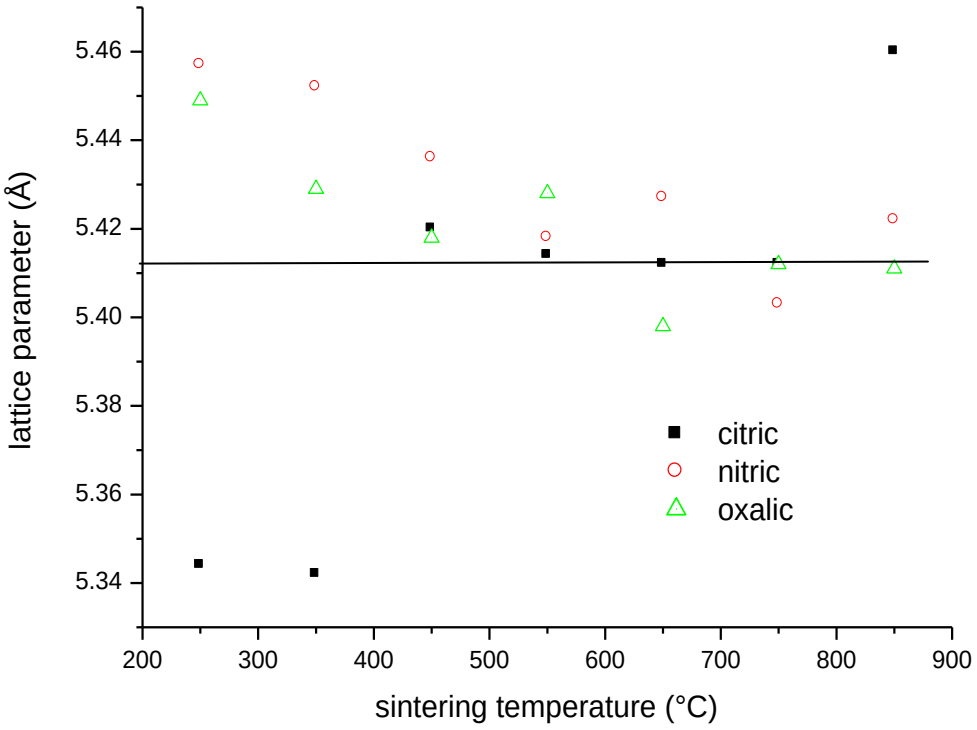


**Figure 3.7:** Lattice parameter as a function of sintering temperature.

The lattice parameter for nitric and oxalic acid show a decreasing value with increasing temperature, whereby it approaches the optimum lattice parameter for the

ceria fluorite structure. This is consistent with the presence of anion vacancy defects at lower temperature and the resultant lattice expansion [129]. However, citric acid deviates significantly from this trend, which suggests that the complexation method of the acid ligands in this synthesis technique differs somewhat from that of nitric and oxalic acid. From the experimental technique employed here, it shows that particle size increases as temperature increases for the citric acid route, though lattice parameter continues to increase steadily.

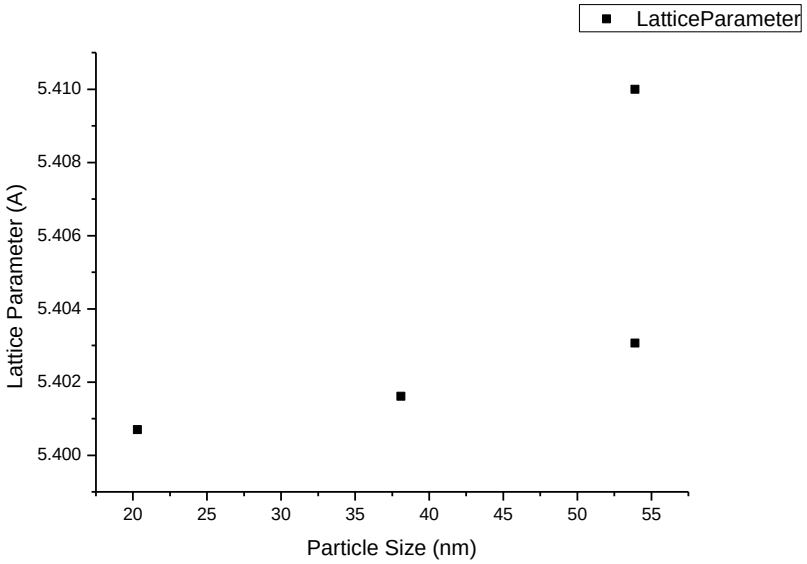


**Figure 3.8:** Lattice parameter as function of particle size for citric acid prep method, calculated using Scherrer Eq.

This is further demonstrated in Figure 3.8, which illustrates lattice parameter as a function of particle size for the citric acid method, calculated using the Scherrer equation, as defined in section 3.2. Once again, this exhibits the same deviations from the optimum lattice parameter.

### 3.5.2 Nitrogen gas adsorption analysis

Figure 3.9 is a plot of the surface area as a function of sintering temperature obtained from nitric acid peptised samples, compared with published results for bulk ammonia

precipitated ceria [130]. Table 3.2 illustrates how the samples prepared using the gel precipitation method differ to the nanoparticles prepared by ammonia precipitation. It is interesting to note that the surface area of the acid samples are 2 to 3 times larger than that of the ammonia precipitated ceria.

**Table 3.2:** BET surface area of acid peptised samples and bulk ceria.

| **Sample** | **Surface area ($m^2/g$)** | **Temperature (°C)** |
|---|---|---|
| **$NH_3$** | 16 | 300 |
| **Nitric** | 52 | 350 |
| **Citric** | 68 | 350 |
| **Oxalic** | 58 | 350 |

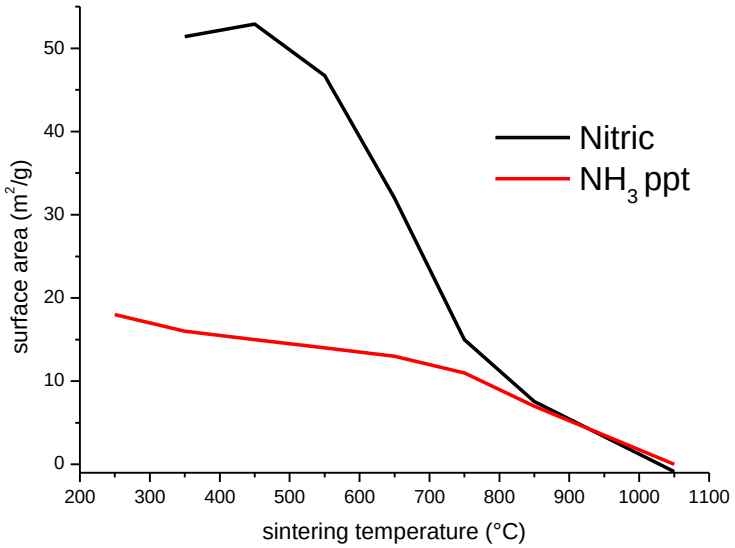


**Figure 3.9:** Surface area as a function of sintering temperature for ceria treated with nitric acid and ammonia precipitated ceria (literature).

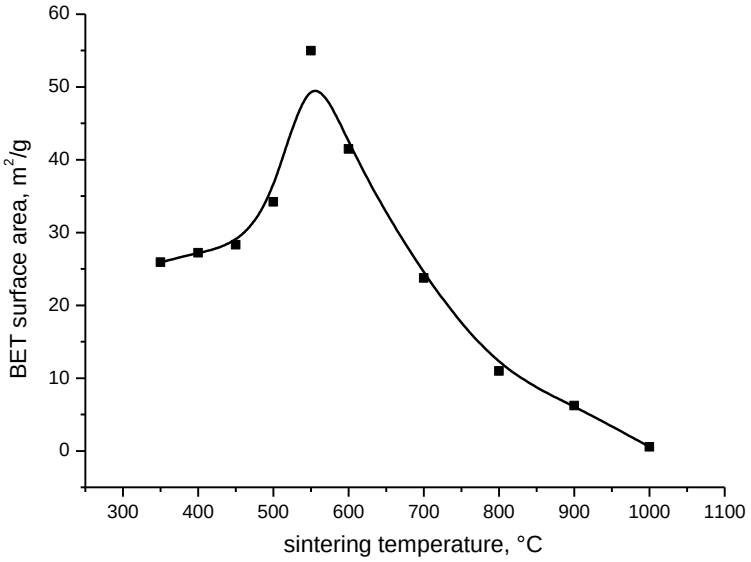


**Figure 3.10:** Surface area as a function of sintering temperature for ceria treated with citric acid.

Figure 3.10 demonstrates surface area as a function of sintering temperature for citric acid precipitated gel samples. Again, we see that, as particle size decreases, a corresponding increase in surface area is observed. As compared to other preparatory methods, this shows a distinct maximum, which in turn suggests the citrate is strongly complexed to the particles, at least at the surface.

### 3.5.3 SEM Analysis

SEM analysis was used to analyse the morphology of the particles produced and to see whether the results were in agreement with those obtained from X-ray diffraction as discussed above. Figure 3.11 to 3.15 are the micrographs obtained from the analysis of nitric acid peptised samples, calcined to 450°C. The images are taken at various magnifications.

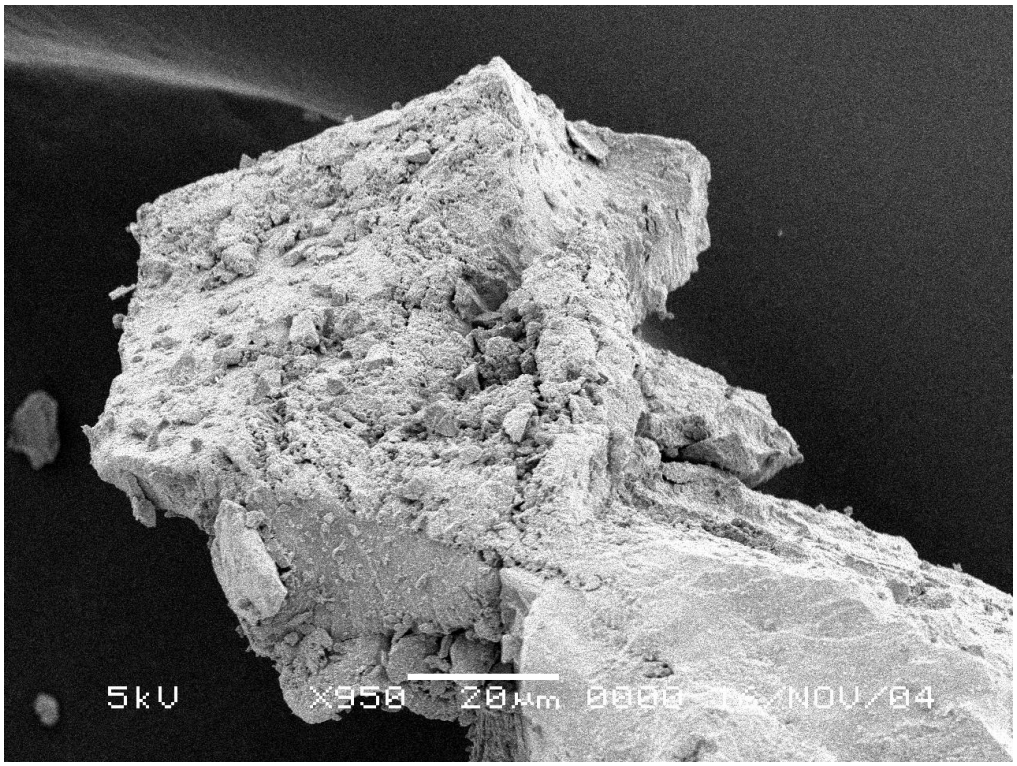


**Figure 3.11:** Electron micrograph for nitric acid peptised gel sample calcined at 450 °C.


**Figure 3.12:** Electron micrograph for nitric acid peptised gel sample calcined at 450 °C.

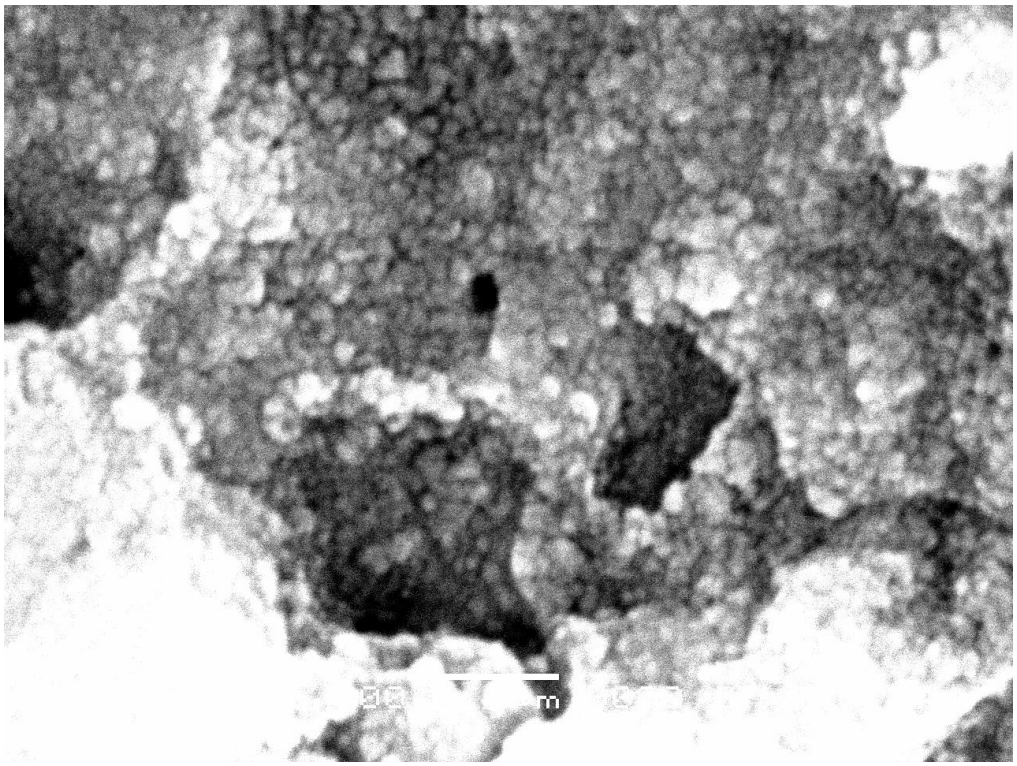

**Figure 3.13:** Electron micrograph for nitric acid peptised gel sample calcined at 450 °C.

### 3.5.4 TEM and HREM Analysis

As measured with TEM, the particle or grain size of the oxide can be seen for each sample and an average value was obtained from the measurement of 100 grains in each powder. At 350 °C, the average particle size is 29.8 nm by comparison with 950 °C where the average grain size goes up to 54.9 nm. At 650 °C, an average particle size of 25.7 nm is measured, which is not too dissimilar from the 350 °C sample. Figure 3.13 shows TEM dark field micrographs of ceria nanoparticles at A) 350 °C, B) 650 °C and C) 950 °C respectively. The Scherrer equation calculations outlined in section 3.3.1 are broadly in line with this TEM analysis.

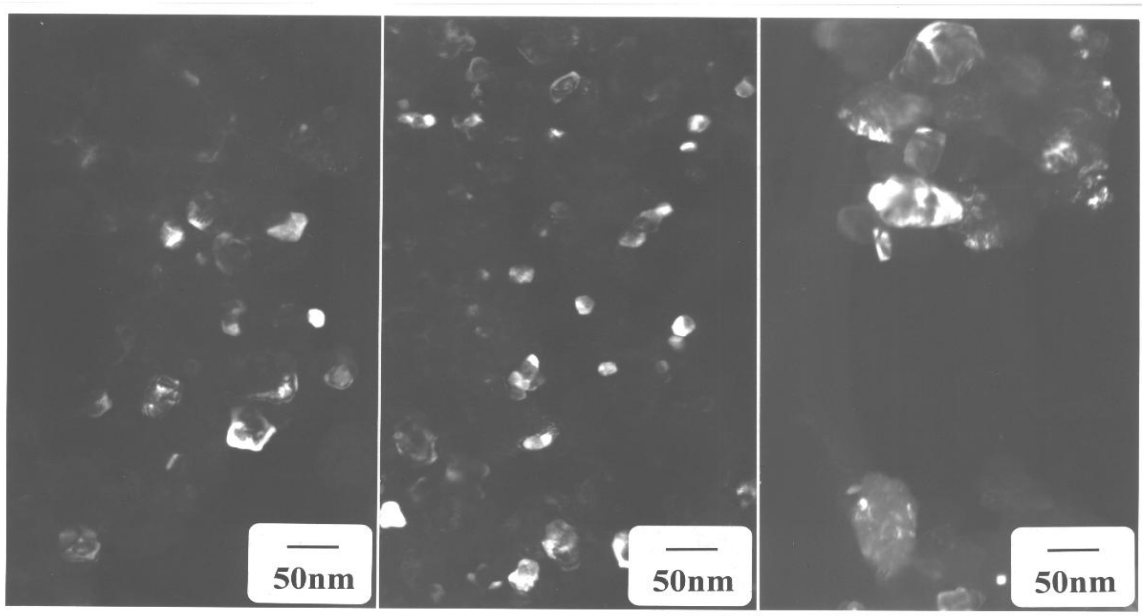


**Figure 3.14:** Dark Field TEM micrographs of ceria nanoparticles at 350 °C, 650 °C and 900 °C

High resolution TEM (HRTEM) was employed to enable direct imaging of lattice spacings which in turn allowed extraction of d-spacings and calculation of the change in lattice parameter for further comparison with PXRD analysis. This was done for each of the three representative temperatures, 350 °C, 650 °C and 950 °C. Figure 3.15 illustrates a HREM image of a single ceria grain/particle calcined to 950 °C. The fast Fourier transform (FFT) computational approach, was employed for the purpose of this research. Initial FFT images at the (1,1,1) and (2,0,0) spacings at 950 °C were found to be 2% larger than those at 350 °C, while the 650 °C were found to be 2 % smaller than those at 350 °C. This is in direct contrast/comparison with PXRD d-spacing analysis presented in section 3.3.1. The reason for this agreement is probably because the product of the simple salt plus base reactions appears to be almost exclusively dense nanocrystals that are highly crystalline with little amorphous or porous character.

It is also important to note that no obvious signs of vacancy clustering can be seen in

Figure 3.15 (and many other similar images). These are visible in atom scale TEM [131] and their absence suggests that the materials are stoichiometric $CeO^2$ or very close to this, ruling out any role of $Ce^{3+}$ like states in the bulk.

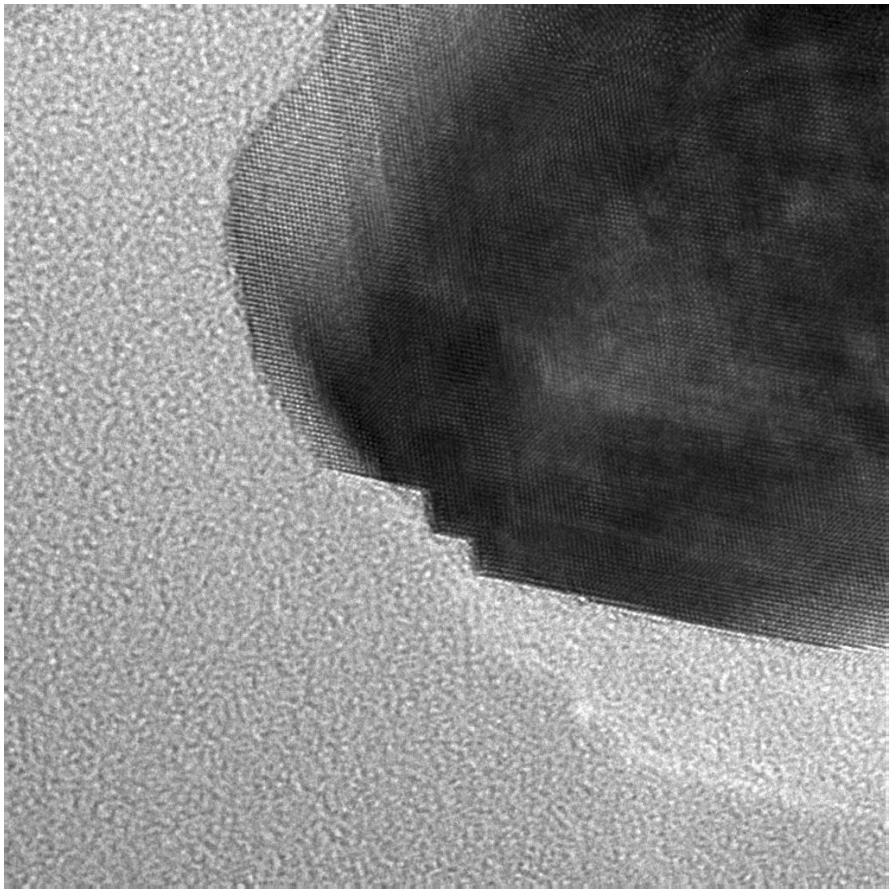

**Figure 3.15:** HREM image of a single ceria grain/particle, calcined at 950 °C

## 3.6 Discussion and Conclusions

The reason for lattice contraction observed is considered at small particles sizes for citric acid produced samples. Results obtained from PXRD analysis suggest that at higher temperatures, defects are being produced which result in lattice expansion as might be expected for small particles. However, below a critical size, lattice contraction maybe observed. These results strongly indicate that surface tension plays a major role in determining the lattice parameter. This is further supported by the decrease in particle size as temperature decreases as measured by TEM and HREM presented herein. The data suggests that anion vacancy defects are not created to any major extent in this work at these small particles. It is difficult to rationalise a reason for the differences in behaviour of citric acid compared to the mineral acids. It may simply be related to the size of the particles produced i.e. citric < oxalic < nitric and this small particle size allows more efficient oxidation in air thereby forming $4^+$ rather than $3^+$ Ce ions. This investigation of lattice parameter changes versus particle size, coupled to very careful synthesis methods, provides a deeper understanding of cerium oxide particle nanoscience.

# 4 Chapter 4 - Comparison of the preparation of nanocrystalline cerium oxide nanoparticles by forward and reverse precipitation

## 4.1 Abstract

The morphological and structural characterization of crystalline $CeO_2$ nanoparticles prepared by forward and reverse precipitation techniques were investigated and compared by powder x-ray diffraction (PXRD), nitrogen adsorption (BET) and high resolution transmission electron microscopy (HRTEM) analysis. The two routes gave quite different materials although in both cases the products were essentially highly crystalline, dense particulates. It was found that the reverse precipitation technique gave the smallest crystallites with the narrowest size dispersion. This route also gave as-synthesised materials with higher surface areas. HRTEM confirmed the observations made from PXRD data and showed the two methods resulted in quite different morphologies and surface chemistries. The forward route gives products with significantly greater densities of $Ce^{3+}$ species compared to the reverse route. Data are explained using known precipitation chemistry and kinetic effects.

## 4.2 Introduction

Cerium dioxide (ceria, CeO2) has been the subject of significant scientific research in recent years due to its distinctive chemical and physical nature and a number of realized and potential applications. Ceria exhibits unique UV absorptivity [132], high thermal stability and mechanical hardness at high temperature coupled to high redox activity [133]. Unique optical characteristics such as Raman-allowed modes shifting and broadening [134]; lattice expansion; and a strong particle size related blue

shift in ultraviolet absorption spectra [135] have been reported. Applications for ceria include: as a support and promoter for exhaust-gas conversion (three-way exhaust catalyst) [136], oxygen ion conductor in fuel cells [137], and gas sensors [138] have also been reported.

With such a variety of applications, different forms (e.g. particulate, mesoporous membrane/film) are needed and many methods of preparing these materials have been reported from these laboratories [139]. Ceria nanoparticles are of particular research interest because of the high chemical activity and surface area of small particulates. Note here that ceria is almost exclusively prepared as nanocrystallites and agglomerations of these form particles (care is needed in the use of terminology). The sensitivity of the cerium electronic band structure to the crystallite size suggests that changes in the chemical properties of ceria crystallitess at nanoscale dimensions might be expected and the effects of crystallite size changes on e.g. the lattice parameter have been reported by Morris and co-workers amongst others [140]. Another example of crystallite size effects, it has been noted that in oxygen sensor applications, by changing the particle size from micrometers to the nanometer region, the response time shortened from minutes to milliseconds [141]. Further, the use of nanocrystalline CeO2 particles have allowed 200-400 °C decreases in sintering temperature when compared with micron sized CeO2 crystallites for the production of dense ceramics [142].

It is clear from the work reported that the continued use of ceria in materials science requires both careful study and realization of rapid and scalable methods to synthesize different sizes/morphologies of the nanocrystallites whilst maintaining narrow size distributions. There are numerous chemical methods for the production of nano-dimensioned crystallites of ceria. These include sol-gel techniques [143, 144], forced hydrolysis [145], microemulsion [146] and precipitation [147, 148, 149] to name but a few. In sol-gel processing, alkoxide or organometallic compounds are typically used as precursors which are expensive. Hydrothermal synthesis and forced

hydrolysis often require severe conditions, such as higher temperatures and pressures and can involve longer reaction times. Microemulsion techniques are an efficient method for preparing highly size monodispersed CeO2 nanocrystallites. However, all of these methods are challenging and expensive to scale to commercially viable quantities.

Precipitation is an attractive route due to the availability of cheap salt precursors, simple operation, and easily scalable for mass production [150]. However, whilst academic synthesis methodology has become ever more complex, there has been relatively little systematic study of the simple precipitation process reported. In particular, we note that "reverse" precipitation of ceria has been scarcely reported. Hassanzadeh-Tabrizi *et al.* and Jalilpour and Fathalilou [151, 152] have used reverse precipitation to generate small crystallites but these have provided little insight to the mechanism and comparison of products to forward precipitation [153, 154]. In this chapter, we analyze the products from precipitation of $CeO_2$ nanoparticles using the reverse precipitation technique and compare the results with those produced using forward precipitation methods and provide a rationale for the materials produced.

## 4.3 Experimental Procedure

### 4.3.1 Synthesis of ceria crystallites

Forward precipitation is the standard methodology used in large quantity production. Briefly, the base is added to the acid under stirring. However, despite the widespread use, care must be taken when precipitation reactions are carried out. As the base is added rapid pH variation occurs locally (at point of addition) due to mixing and more slowly through the course of the synthesis. The reaction might also be exothermic and heat variation may also occur. Crystallites may appear only later to be re-dissolved as stirring occurs. This precipitation process is complex and these

transient changes in solution can cause composition inhomogeneity [147], wide size ranges [142] as well as other product variation. The sensitivity of product to varying pH can cause effects such as coring when product stability is sensitive to pH [155].

Forward precipitation was investigated using the forced hydrolysis of cerium nitrate hexahydrate with ammonia hydroxide solutions [145]. Te resultant precipitates were then peptised to a sol-gel to provide more unform product. Three different peptizing acids for comparison; citric acid, oxalic acid and nitric acid were examined, but citrate proved the most effective giving the smallest crystallites and a narrow size distribution and only these results are presented. A 1 molar solution of cerium (III) nitratehexahydrate, $Ce(NO_3)_3.6H_2O$ was used. 100 ml of this solution was poured into a 250 ml beaker and stirred continuously at room temperature. The pH of this solution was measured at about 2.2. A 2 molar solution of ammonium hydroxide solution was added at the rate of about 0.1 ml $s^{-1}$ to a final pH of 12. This resulted in an immediate white or yellow emulsion which on stirring became brownish-purple. The precipitate was recovered by filtration and was vacuum dried on a Buchner funnel. Once dry, the precipitate was scraped into a crucible and dried overnight in the oven at 80 °C. On drying, the precipitate was lemon yellow in colour and was ground down to a fine powder using a pestle and mortar. This sample was then suspended in water and peptized using drop-wise addition of citric acid until a clear sol-gel was formed. The resultant gel was dried as above and samples were calcined at 350 °C for 8 hours and then portions of this were calcined at 50 °C intervals to vary the crystallite size.

The “reverse” precipitation technique was identical to the forward precipitation technique, except that in this case the Ce (III) solution was added (at same rate above) to 100 ml of the ammonium hydroxide. All subsequent processing steps wee as described above for the forward precipitation route. The initial and final pH during precipitation were measured at around 13.5. The initial precipitate formed was yellow/white but then became brown/purple before finally turning green/yellow.

The precipitate formed was aged, recovered and subsequently processed as detailed above. Unlike the forward precipitation where heat was needed to affect colour change to white/lemon and remained purple until drying, the recovered solid precipitate turned bright yellow during washing washing, filtering and vacuum drying. The colour changes observed can be tentatively assigned to changes in oxidation state as it has been suggested that a cerium III precipitate product is a light purple colour and a cerium IV precipitate product is light yellow [156]. Thus, it seems likely that the reverse precipitation material contains significantly less $Ce^{3+}$ states then the forward precipitation product.

## 4.4 Analyses

To characterize the morphology of the nanoparticles, powder x-ray diffraction (PXRD) patterns were recorded on a Phillips PW 3710 Xpert MPD diffractometer ($\theta$~$2\theta$ mode), equipped with a Cu Kα radiation source (operating at an accelerating of 40 kV and an anode current of 30 mA) of wavelength 1.54 Å. A nickel mask was used to eliminate $K\beta$ radiation and a standard scintillation detector was used. The instrument was calibrated against a ceria sample aged at 1200 ° for 24 h to ensure accuracy. Data were collected over the range of 10 – 70 °2θ, using a step size of 0.03°. Measurement of lattice parameters were not made by simple analysis of peak positions, but rather by using detailed Rietveld simulation studies where the position of the features were quantitatively matched in simulation by changing lattice spacings within the crystal framework. The Phillips Analytical Rietveld 1.0b software package used also permitted quantitative analysis of each phase present. The crystallite size was calculated using the Scherrer equation, $t = K\lambda/B\cos\theta$. All sizes are quoted for samples are an average result of 5 different reflections, between 25 - 60° 2θ.

The nitrogen adsorption and desorption isotherms at 77 K were measured using a Micromeritics Gemini 2375 volumetric analyzer (Micromeritics Instrument

Corporation, UK). All samples were degassed under the flow of ultra high grade 5.0 nitrogen at 200 °C for 4 h prior to each measurement. Scanning electron micrographs (SEM) were collected on a JSM-5510 apparatus (JEOL) using a beam voltage of 5 kV. Transmission electron microscopy (TEM) was used for structural characterization. Each powder was dispersed onto holey carbon support grids and examined at 200 kV in a JEOL 2000FX microscope.

## 4.5 Results

The precipitation reactions can be described by reference to known chemistry and the observed colour changes noted above can be explained by this reaction. For both forward and reverse precipitation reaction begins with solution of cerium nitrate to yield $Ce^{3+}$ as expressed in equation 4.1. The solvated cations react with OH- ions formed by protonation of $NH_3$ molecules (equation 4.2). Equation 4.3 shows reaction of the aqueous cerium cations with hydroxyl ions. The product $Ce(OH)_3$ cerium (III) hydroxide) is quickly precipitated out due to an extremely low solubility constant ($K_{sp}$ = 6.3 x $10^{-24}$ at 25 °C) [157]. It is clear that this species is formed in both reactions and results in the strong purple colour. Chen *et al*. [139] suggested that a strongly basic solution favors $Ce^{4+}$ compared to $Ce^{3+}$ via a base oxidation process and the precipitate can be oxidized as shown in equation 4.4. As shown in equation 4.5 the product $Ce^{4+}$ ions undergo strong hydration and form aqueous coordination shells. This reaction scheme is important because it has been shown that the rate of reaction of equation 4.4 is critical in determining the final particle size and Zhou *et al*. [157] showed that the size of $CeO_2$ particles can be significantly decreased by introducing oxygen bubbles into solution to react with the as-formed $Ce(OH)_3$. This is presumably because it limits growth of the $Ce(OH)_3$ particles due to formation of highly insoluble $CeO_2$ type materials.

$$2Ce(NO_3)_3 \rightarrow 2Ce^{3+} + 6NO_3^- \quad \text{Eq(4.1)}$$

$$NH_3 + H_2O \leftrightarrow NH_4^+ + OH^- \quad \text{Eq(4.2)}$$

$$Ce^{3+} + 3OH^- \leftrightarrow Ce(OH)_3(aq) \quad \text{Eq(4.3)}$$

In large excess of base oxidation can occur:

$$2Ce(OH)_3(aq) + 1/2\ O_2 \rightarrow 2CeO_2(aq) + 3H_2O \quad \text{Eq(4.3)}$$

$$Ce(H_2O)_x(OH)_y^{(4-y)+} \rightarrow CeO_2.2(H_2O) + (4\text{-}y)H_3O^+ + x\text{-}2(H_2O) \quad \text{Eq(4.4)}$$

This reaction scheme suggests that there may be significant differences in the product of forward and reverse precipitation. In forward precipitation, nucleation and growth occurs at quite low solution pH since base is being added to acid. Thus it might be expected that the reaction will produce much higher concentrations of $Ce^{3+}$ particularly at the early stage of the process. The observation of an initial white/yellow colour is probably due to high local concentrations of base favouring $Ce^{4+}$ which then become $Ce^{3+}$ as the solution is stirred. As the reaction proceeds and the solution becomes more basic, it might be expected that the reaction begins to yield $Ce^{4+}$, however, the formation of the tetra-valent species might be limited because precipitation is complete. In reverse precipitation, the acid is added to base and material is precipitated in strongly alkaline conditions favouring initial formation of $Ce^{4+}$. As the reaction proceeds, there is an increased tendency to precipitate $Ce^{3+}$ as the solution becomes less alkali. This is consistent with the observations made above where the precipitate was in initially white/yellow but became brown/purple. The reaction also explains why the precipitate changed to yellow during vacuum drying as a rapid surface reaction is enough to convert the surface tri-valent cations to $Ce^{4+}$ whilst for the forward precipitation reaction extended times and temperatures are required for oxidation as the bulk is $Ce^{3+}$. With such changes in the precipitation mechanism, the physical and chemical properties of the products should be markedly different. Data showing this is the case is described below.

Figure 4.1 shows the PXRD pattern for materials prepared via forward precipitation

that have been calcined in the temperature range of 350 °C to 1050 °C. The reflections observed are characteristic of the cubic fluorite F*m*3*m* structure [158] and the main reflections observed are indicated in the figure. Between 350 and 550 °C the peaks are broad and typical of very small crystallite sizes. It is only after heating to 850 °C, the peaks become sharp and symmetrical consistent with crystallite growth. There is no tendency to form any other phases, regardless of age, time or temperature.

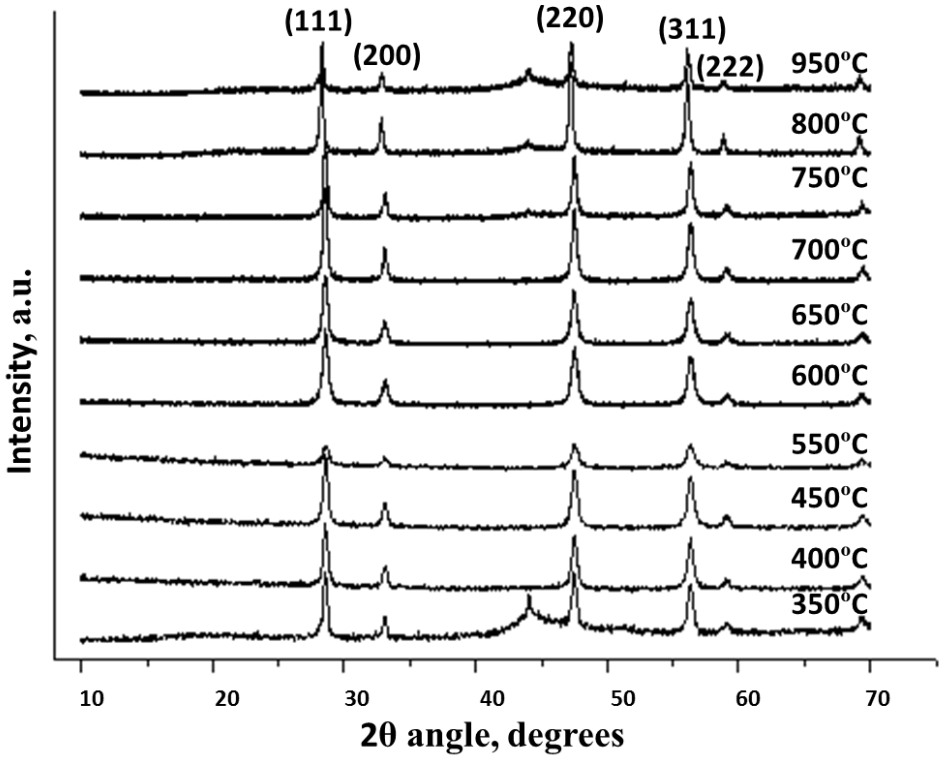


**Figure 4.1:** XRD data of CeO2 prepared by forward precipitation technique calcined at various temperatures between 350 °C to 950 °C. There is a weak reflection around 43 °2θ which is due to scatter from the sample support.

Figure 4.2 shows similar PXRD patterns for $CeO_2$ prepared by reverse precipitation following calcination at various temperature. As with forward precipitation, the characteristic cubic F*m*3*m* fluorite structure is observed. Between 350 and 500 °C the peaks are broad and typical of small crystallites, and significantly the broadening

of the diffraction features at low calcinations temperature is much more apparent for these materials compared to those prepared via forward precipitation. Following calcination at higher temperatures, the peaks become significantly sharper and more symmetrical typical of rapid crystallite growth. As in forward precipitation, the samples show no tendency to form any other phases, regardless of age, time or temperature and there is no evidence of new diffraction peaks.

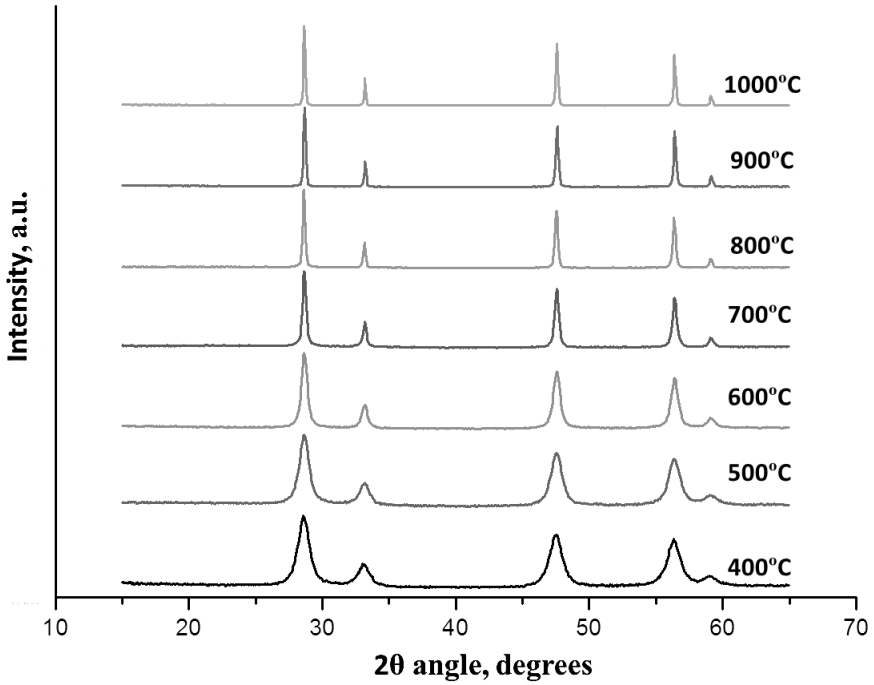


**Figure 4.2:** PXRD data of $CeO_2$ prepared by the citric acid reverse precipitation technique calcined at temperatures between 350 °C to 1000 °C as shown.

The PXRD were quantified for accurate comparison of lattice parameter and crystallite size. The crystallite size and lattice parameter data are shown in Figure 4.3 for both forward and reverse precipitation methods. As seen in Figure 4.1, the crystallites grow continually through the calcination regime (Figure 4.3A) with more rapid growth beginning at temperatures greater than 650 °C. The minimum crystallite size observed is after the lowest temperature calcination and is 16.5 nm and

this has increased to 38.9 nm after 650 °C calcination. The lattice parameter varies with particle size as revealed in Figure 4.3B and shows a decreasing value with increasing crystallite size eventually reaching the value of around 5.411 Å expected for bulk ceria at largest crystallite sizes Lattice parameter expansion at low crystallite sizes has been ascribed to increased amounts anion vacancies and accompanying $Ce^{3+}$ defects at the surface of nanocrystallites and the change with temperature due to decreasing contribution of the surface as crystallite size increases (due to sintering) and/or oxidation at higher temperature. As discussed by Chen *et al.* [139] lattice parameter reduction may also be explained by the presence of tri-valent cerium hydroxyl states rather than anion vacancy production.

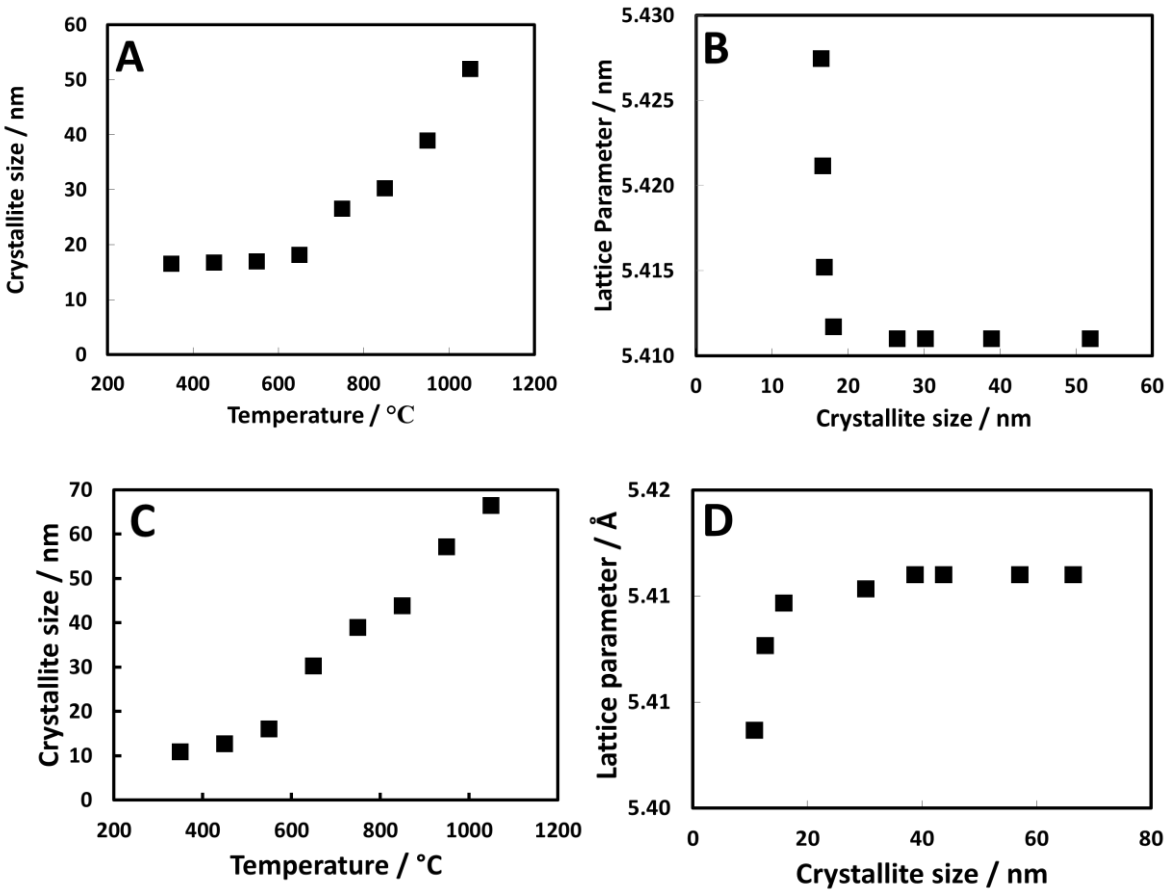


**Figure 4.3:** Comparison of XRD derived data sets. A and B represent the crystallite size variation as function of calcination temperature and the lattice parameter against crystallite size respectively for the forward precipitation route. C and D are similar data for the reverse precipitation route.

In reverse precipitation the crystallite growth with calcination temperature follows a similar trend (Figure 4.3C). However, the crystallites grow at an increased rate. After 350 °C calcination the crystallite size compared to the forward precipitation route is lower at a value of 10.5 nm. However, following 950 °C calcination, the crystallite size is higher at 57.2 nm. This is consistent with the expected increase in sintering and densification known for smaller crystallites and is due to increased

crystallite-crystallite contact and lower mass transport limitations [142]. The change in lattice parameter with crystallite size shows the opposite trend to that of forward precipitation. At smaller crystallites sizes the lattice parameter is reduced compared to the bulk value and increases with crystallite size until the bulk value is attained. Chen *et al.* [139] have argued such lattice contraction arises from surface tension effects in small particles. Chen *et al.* argued the precipitation route is important in understanding lattice parameter changes for $CeO_2$ since the amount of surface hydroxyl states causing lattice expansion at small crystallite sizes can mask the inherent lattice contraction due to surface tension [139]. It would, thus, appear that the reverse precipitation route is linked to lower $Ce(OH)_3$ type states and suggests that these have been converted to $CeO_2.(2H_2O)$ consistent with higher pH during the precipitation process. As reverse precipitation is the addition of the metal nitrate (acid) to a large excess of base, the lattice parameter measurements observed are consistent with the methodology.

The surface area of these materials was also measured by BET (nitrogen) technique and the results are consistent with the PXRD measurements showing higher surface areas and greater pore volume at lower calcinations temperatures (i.e. smaller crystallite sizes). Typical isotherms for forward and reverse precipitation are shown in Figure 4.4 (A and B). All isotherms, bar some of the samples at high calcinations temperatures, can be classified as type IV [159] typical of mesoporous materials. The shape of the isotherms and the measured crystallite sizes suggests inter- crystallite pores are present. As can be seen in Figure 4.4A and Figure 4.4B, the mesopore structure is essentially lost for the reverse precipitation process (but note the forward precipitation) as little hysteresis is observed. This is consistent with the suggested higher sintering rate suggested from analysis of the PXRD data.

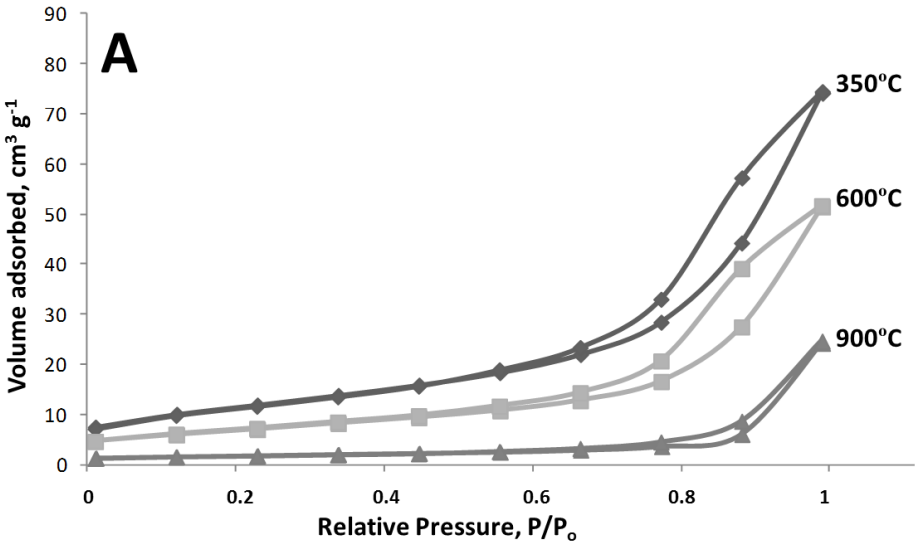


**Figure 4.4A:** Pore Volume measured at 350 °C, 600 °C and 900°C for forward precipitation technique

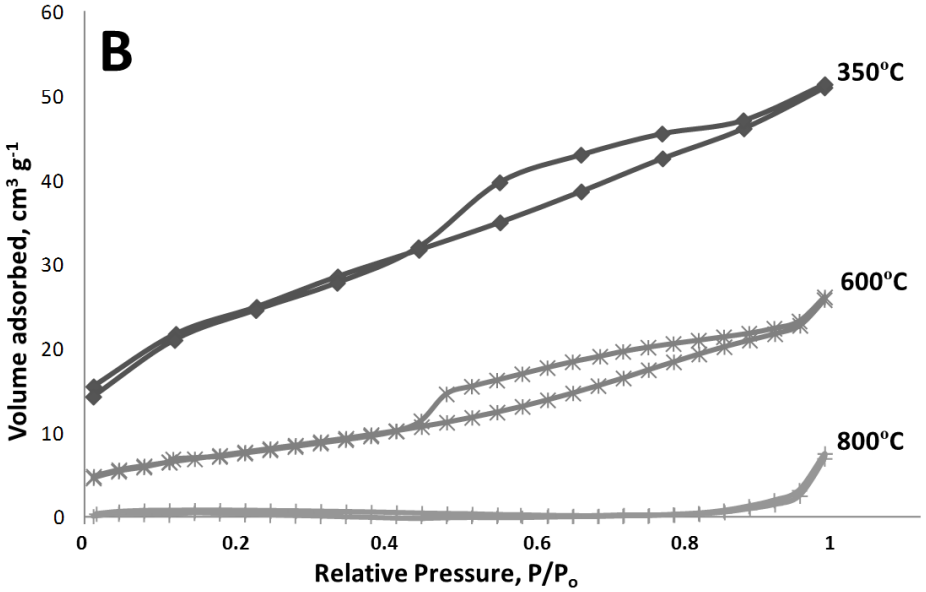


**Figure 4.4B:** Pore Volume measured at 350 °C, 600 °C and 800°C for reverse precipitation technique

This is confirmed in the data shown in Figure 4.5 which describes the quantification of the BET derived surface area data for the samples prepared via reverse precipitation compared to values calaculated via the Scherrer crystallite sizes. The latter was estimated assuming an octahedrally shaped crystallite which is a reasonable assumption considering previous work [160] and the TEM data shown below. The surface area was calculated from the ratio of the surface area ($=2\sqrt{3}a^2$) and volume ($^1/_3\sqrt{2}a^3$) using the Scherrer calculated values as a. It can be seen that the data are in reasonable agreement at low calcination temperatures but the measured surface area decreases more markedly than the calculated data at temperatures > 650 °C. The low temperature agreement (any variance can be assumed to be due to the simple geometric calculations and disregarding of the contact between crystallites) again suggests the crystallites are dense and have negligible intra-crystallite porosity. It is suggested that the data diverge at higher temperatures because significant crystallite-crystallite condensation is occurring as well as inter-crystallite pores become closed and non-available to nitrogen adsorption.

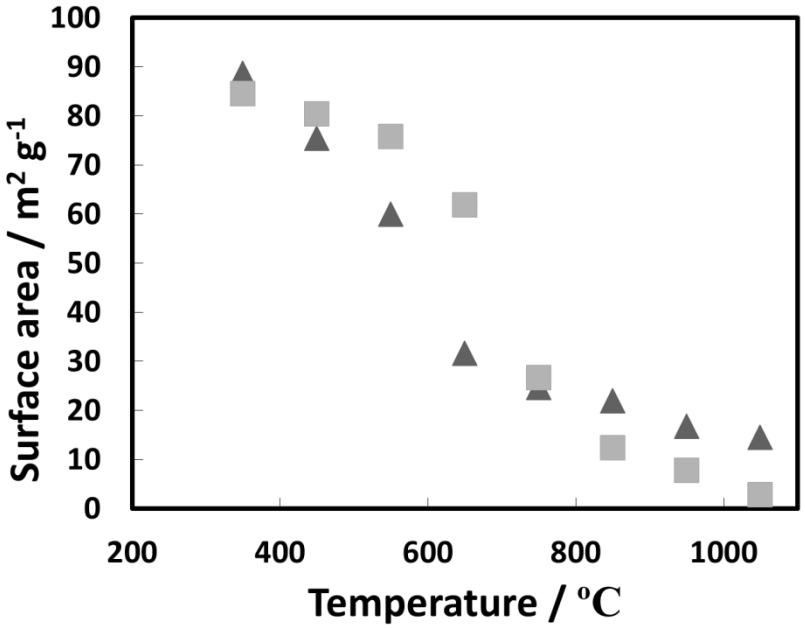


**Figure 4.5:** Surface area vs. calcination temperature for reverse precipitation. ■ are BET measured data and ▲ are calculated from XRD derived crystallite size data assuming cubic crystallites.

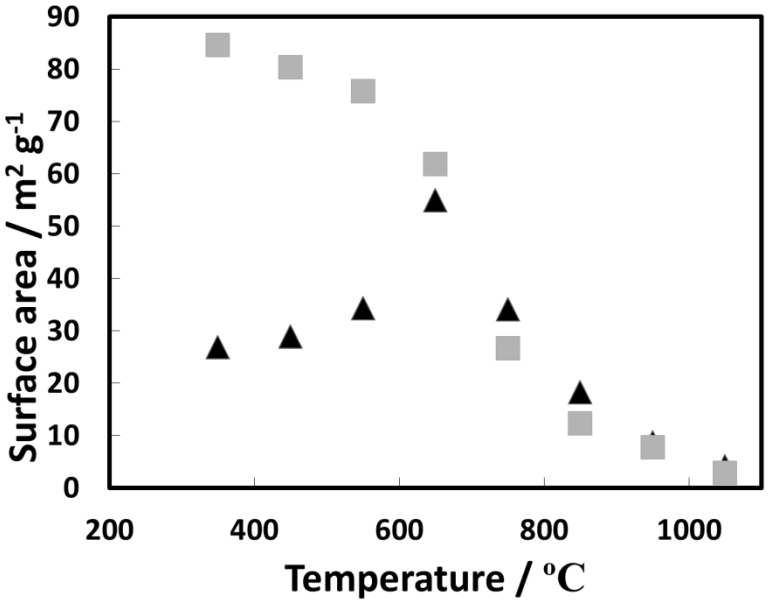


**Figure 4.6:** Surface area (via $N_2$ adsorption isotherms) vs. calcination temperature for forward (▲) and reverse (■) precipitation.

Figure 4.6 compares the variation in surface area of materials prepared via forward and reverse precipitation following different calcinations treatments. The surface area of the materials prepared via forward precipitation is more complex than that of similar forward precipitation prepared samples and shows a quite clear maximum surface area at 550 °C as can be seen in Figure 4.6. The data suggest some type of thermal decomposition is taking place from around 400 °C. The surface area increases from 26.8 to 54.9 $m^2$ $g^{-1}$ following calcination at 350 and 550 °C and then decreases until it follows the same curve as that shown by the reverse precipitated materials (comparison data shown in Figure 4.6). It is suggested that the different behaviour derives from strong a mixture of strong hydrogen bonding and condensation of –Ce-OH groups (loss of water and formation of –Ce-O-Ce- linkages) at the points of contact between crystallites and so decreasing the surface area below that expected from the crystallite size. As the temperature increases, the $Ce(OH)_3$ species are oxidized to $CeO_2$ and the surface area apparently increases. Again the data is consistent with higher concentrations of Ce(OH)3 for the forward precipitation technique. It should be noted that the decomposition of cerium hydroxyl species formed in nanocrystallites is seen around 400 °C to support the suggestion made here [142, 148].

TEM confirm the suggestions made above and typical micrographs of samples prepared via forward and reverse precipitation following 350 °C are shown in Figure 4.7. In all cases only crystalline particles were observed and there was no evidence of amorphous material or pores within the crystallites as was suggested by the BET and XRD studies. Average crystallite sizes are in reasonable agreement with XRD measurements at about 15 to 20 nm for forward precipitation and 8 – 12 nm for reverse precipitation and confirm the smaller size of particles formed via the reverse precipitation method. The crystallite shape of each preparation route is also markedly different. From forward precipitation the products are not only larger but also have more well-defined shape with two different morphologies present (Figure 4.7A and 4.7B). A number of crystallites have cubic and pseudo-cubic geometry (as

marked with dashed lines in Figure 4.7A) whilst others have a platelet structure (see the darker image shown in Figure 4.7B). Cubic $CeO_2$ crystallites are well known and are thought to arise via Oswald Ripening of more spherical shapes precipitated in the early stages of growth [161]. In the case of reverse precipitation, the crystallites are noticeably smaller and the size dispersion much less (Figure 4.7C). The crystallites now appear to adopt largely one shape have a more dimensionally uniform shape appearing almost spherical in nature. Closer examination reveals them to be polyhedral with relatively well-defined crystal facets as indicated in Figure 4.7D and are similar to shapes seen in previous work [160, 162] and can be best described as truncated octahedral [163]. The smaller size of the materials prepared via reverse precipitation can be explained by increased oxidation rate [162] and/or kinetic and thermodynamic limitations where good evidence has been provided that the truncated octahedra morphology is the precursor to platelet and cubic morphologies due to orientated attachment along the well-defined crystallite faces [164].

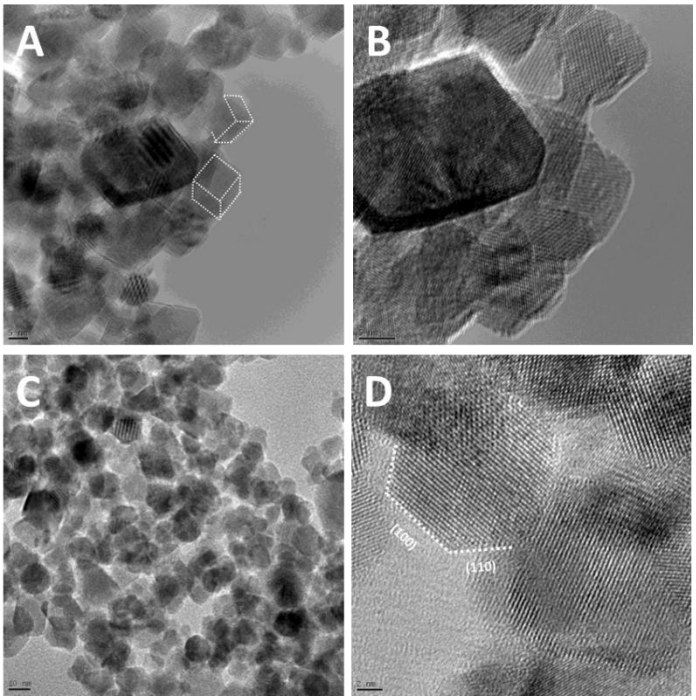


**Figure 4.7:** TEM images (high and low magnification) of samples following 350 °C calcination. A and B represent a sample prepared via forward precipitation and C and D via reverse precipitation.

## 4.6 Discussion and Conclusions

Forward and reverse precipitation gives markedly different products. Pourbaix diagrams show that $Ce^{3+}$ is stable in solution at normal pH values and that a minimum pH value of 4-6 must be reached before formation of $Ce(OH)_3$ occurs [165]. However, the $Ce(OH)_3$ formed has some solubility to a pH of about 10 when precipitation of the hydroxide is rapid. As the pH is raised further, the formation of $Ce^{4+}$ ($Ce(OH)_4$ or $CeO_2.2H_2O$) products becomes more likely, consistent with the reaction model given above in Eq. 4.1 – Eq. 4.5. It thus seems that the reverse precipitation, where the pH through the process is uniformly high, is likely to give a $CeO_2$ type product whilst the forward precipitation process is more likely to give $Ce^{3+}$ precipitates particularly during the early stages of the process where the pH changes from acidic through to alkaline. This suggestion is apparently borne out by both the

colour changes observed during synthesis and the lattice dimensions measured by XRD as well as previous XPS measurements [140].

What is also important is that the products of the precipitation are smaller and have lower size dispersions. This is also partly explained by the Pourbaix diagrams as the entire precipitation process occurs at a pH value where solubility is limited and thus nucleation, re-solution and the size related thermodynamic stability [166] of the particles has a much lesser effect and the statistical nature of the particle growth process is limited. Zhou *et al.* offer a detailed rationale for the size homogeneity of the product [149]. These authors point out that the solutions with high pH are highly supersaturated and this provides conditions for homogeneous nucleation. It should also be noted that growth of large particles is reliant on two processes; the normal Ostwald Ripening and also orientated attachment [157]. Orientated attachment is enhanced by surface hydroxyl groups ($Ce(OH)_3$) and so will tend to form larger crystallites. It is also interesting to note that the orientated attachment mechanism promotes formation of cubic [157] and linear [141] crystallite morphologies. It can, therefore, be reasonably asserted that this is the cause of the cubic and platelet structures seen for the forward precipitation route (Figure 4.7) and supports the higher $Ce(OH)_3$ content suggested by experimental evidence presented here for this preparation route. It might be thought that the oriented attachment is limited for $CeO_2$ type products because of the lower surface hydroxyl densities and thus the truncated octahedral shape is maintained.

From this work, it is suggested that reverse precipitation, which is often ignored as a synthesis method, can provide a useful methodology to produce small particles producing a more size homogenous product and smaller particle sizes/higher surface areas. However, the products can have markedly different crystallite shapes and surface chemistries. They are likely to be more 'passive' to particle-particle attachment and also contain lower defect densities as they consist of single crystallites following homogeneous precipitation.

# 5 Chapter 5 - The Structure and Defect Chemistry of Ceria-Terbia Solid Solutions

This chapter is based on a paper which has been presented in a poster format at INSPIRE 2009 and it has been published in a letter format in Chemical Physics Letters.

## 5.1 Abstract

The addition of terbia to ceria has been investigated using XRD, XRF, XPS and TEM. Good solid solutions were formed across the entire composition range and there was no evidence for the formation of mixed phases or surface segregation over either the composition or temperature range investigated. Both $Tb^{3+}$ and $Tb^{4+}$ ions exist within the solution and the ratios of these cations are consistent with the addition of $Tb_8O_{15}$ to the fluorite ceria structure across a wide range of compositions. Local regions of anion vacancy ordering may be visible for small crystallites. There is no evidence of significant $Ce^{3+}$ ion concentrations formed at the surface or in the bulk by the addition of terbia. The lattice parameter of these materials was seen to decrease with decreasing crystallite size. This is consistent with increased surface tension effects at small dimension.

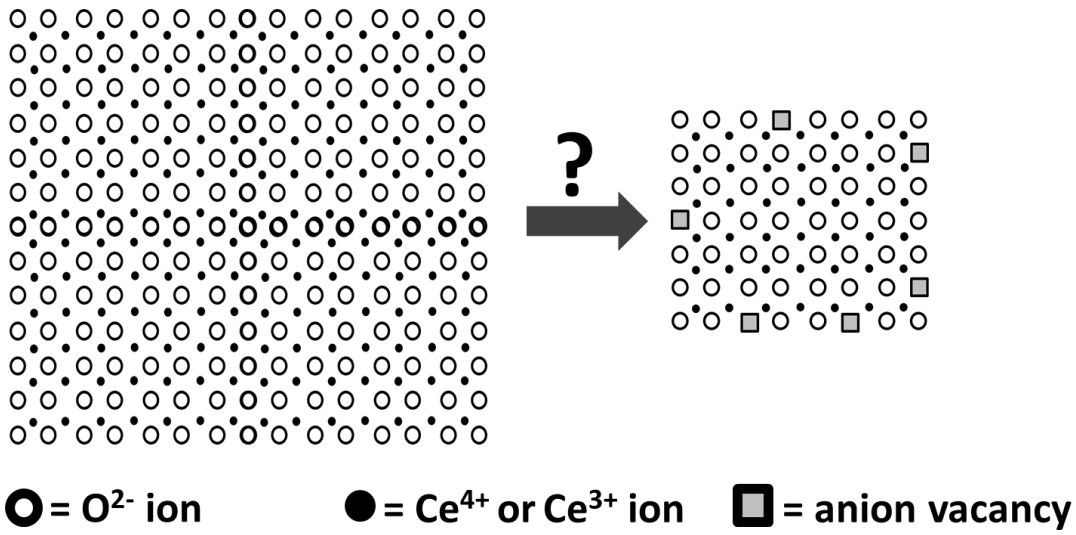


## 5.2 Introduction

Cerium dioxide ($CeO_2$), ceria is one of the most studied inorganic oxides. In practical terms this is due to its' use in several processes [167, 168] including car exhaust [169] and combustion catalysis [170], its' use as the polishing material in silicon wafer production [171], its' application in fuel cell technology [172] and in hydrogen generation [173]. Scientifically, it has been of long term interest because its' crystal structure and defect chemistry [167, 174, 175,176]. The fluorite phase is a frequently found crystal structure and a structural motif found in more complex inorganic materials [176]. Because of the similarity of the thermodynamic stability of the tri-valent and tetra-valent oxide states of cerium, there is well documented non-stoichiometry of this oxide and the composition of the oxide can be written as $CeO_{(2-x)}$ [167, 174, 175]. Here, anion vacancies are introduced into lattice and it is generally accepted that these are charge compensated by the existence of reduced valence cation sites ($Ce^{3+}$ ions) although a more correct explanation of the defect mechanism is described in terms of a small polaron state. The presence of these defects is what makes ceria an industrially important material as they facilitate a range of redox reactions, oxygen storage and increase electrical conductivity [167, 168]. Most importantly, these defects can be added without significant structural

modification (thereby preventing dramatic phase changes and accompanying changes to e.g. surface area) although small lattice parameter changes and some anion vacancy superstructures can be formed [176].

However, ceria is seldom used in a pure form and ‘dopants' are normally added to increase the concentration of anion vacancies [177, 178, 179, 180]. This has a remarkable effect on electrical conductivity [181] and catalytic activity [167, 168, 170, 182]. Common additives include the sesquioxide lanthanide oxides (e.g. $Gd_2O_3$, $La_2O_3$, $Sm_2O_3$). The anion vacancies are formed because of the need to charge compensate the $Ln^{3+}$ cation sites in the fluorite type lattice. Unlike the case for undoped ceria, these substituents are not associated with any additional electron states. Terbium oxide is one of the least studied lanthanide oxide additives to ceria. This is probably due to its cost (Tb is around 60 times less common than Ce [183]). Tb exhibits a mixture of 3+ and 4+ states and, like ceria, has a well-developed non-stoichiometry [183]. All authors report that the addition of terbium oxide to ceria results in a mixture of $Tb^{3+}$ and $Tb^{4+}$ ions at fluorite cation sites [184, 185, 186, 187, 188, 189, 190, 191, 192, 193]. Wang *et al.* [194] suggest that the concentration of $Tb^{3+}$ relative to $Tb^{4+}$ decreases with dopant concentration. The majority of authors claim that $Ce^{3+}$ is also present (this is not a necessary part of doping as the $Tb^{3+}$ species balance the vacancy insertion) but it is not clear in many cases that this is associated with the usual ceria non-stoichiometry (associated with thermal or redox treatments, surface chemistry and segregation) or is a result of the doping making reduction more facile. Martínez-Arias *et al.* [184], Guo *et al.* [185] and Wang *et al*. [194] suggest that no or very limited $Ce^{3+}$ is formed on terbium ion addition.

Thus, some confusion in understanding this system exists. This is partially related to the fact that a comprehensive study of the structural changes as a function of dopant concentration is not available as it is e.g. for La and Pr [177, 180, 195]. Indeed, there are only two reports of loading levels greater than 20 mol% (both at 50 mol%)

[184, 194] and higher loadings are needed to determine solubility limits etc. This work is motivated by an attempt to address this paucity of data and also to examine if some of the conflicts in the literature result from variations in the nanoparticulate (more correctly nanocrystallite) nature of many of the samples studied. Further, we have recently discussed the importance of nanocrystalline dimension for ceria and in particular how lattice parameters can be reduced at small particle sizes, [175, 196]. In that work, the tendency to stabilize 3+ states at low particle sizes (causing lattice expansion) counters the size dependent reduction of the lattice parameter. The possibility of studying a system where $Ce^{3+}$ sites are not a contributing factor to size effects provide a strong stimulus for this work.

## 5.3 Experimental Procedure

### 5.3.1 Sample preparation

Samples were prepared via reverse precipitation where a mixed cerium (III) nitrate hexahydrate/terbium(III) nitrate pentahydrate aqueous solution (0.05 M total metal) was added slowly to a 0.5 M $NH_4$ solution. This method was found to yield smaller crystallite sizes and a more homogeneous distribution of terbium within a crystallite because the pH of the final solution remains strongly basic through the precipitation process and avoids the strong pH effects reported by us for the $CeO_2$-$La_2O_3$ system [197]. The cerium and terbium relative concentrations were varied to provide a wide range of concentrations. After addition the solutions were mixed for 1 h before filtration and triply washing in deionized water. All samples were calcined at 500 °C for 12 h to ensure complete removal of carbonate. Samples were labelled as CTBXX where XX is the measured terbium mol%. CTB is a terbium oxide sample with no ceria and CEO is a cerium oxide only sample. Analysis was performed on samples that had been calcined at various temperatures for 4 h.

## 5.4 Analyses

Powder x-ray diffraction (PXRD) patterns were recorded on a Phillips M-PRO diffractometer equipped with a PIXEL detector using CuKα radiation. In most samples 5% w/w of zirconia (previously calcined at 1200 °C for 24 h to provide sharp lines) was added as an internal reference so that reflection positions and, hence, lattice parameters could be accurately determined (+/- 0.02 Å). Zirconia was added after sample calcination to prevent any solid state reactions occurring. This method is necessary to remove errors in sample height/position which varies from sample to sample. PXRD scans were an average of 4 individual scans to increase the signal to noise ratio. The lattice parameter was estimated from $a = n\lambda(h^2+k^2+l^2)^{1/2}/2\sin\theta$ using 4 reflection positions (θ is the diffraction angle). Total external reflection x-ray fluorescence (TXRF) data were used to estimate the metal mole% of Tb in each sample. Data were obtained using a Bruker S2 PICOFOX instrument and quantification was via peak fitting combined with full matrix calculations. The accuracy of this method was compared to analysis of 3 physical mixtures of $CeO_2$ and $Tb_4O_7$ (calcined at 1000 °C ) to ensure accuracy. From these comparisons, the error in calculated versus actual ratio was estimated as < 2 mole%. Transmission electron microscopy (TEM) data were collected on an FEI Titan system with aberration correction. X-ray photoelectron spectroscopy (XPS) data were collected using a Vacuum Science Workshop Atomtech ESCA system using Al kα radiation (200 W). A pass energy of 50 eV was used. For XPS analysis, samples were pressed into discs and binding energy referencing was achieved by reference to an adventitious C1s feature at 285.0 eV. No differential charging of the samples was observed. Prior to analysis, samples were heated at about 110 °C in vacuum to minimize surface contamination and outgassing during analysis.

## 5.5 Results

Typical TXRF data are shown in Figure 5.1A. No unexpected lines could be observed and only Tb and Ce features could be detected with any impurities estimated to be less than 0.1 mol%.

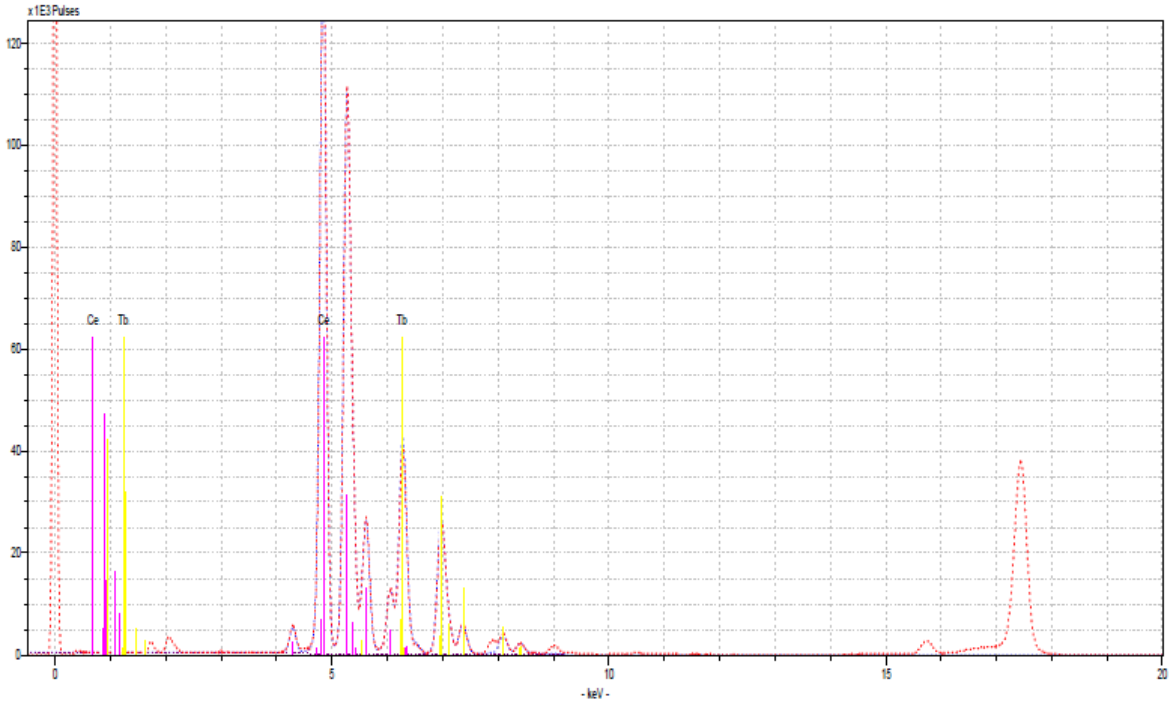


**Figure 5.1A:** Typical TXRF data from a cerium terbium oxide (Tb at 8 mole%) solid solution. The dashed line is the raw data and the expected fluorescence lines are marked.

The measured terbium concentrations were always less than might be expected from the original mixed nitrate solution (target) concentrations as detailed in Table 5.1.

**Table 5.1:** Target concentration (TCO) versus measured terbium sample concentration (MCO)

| **TCO** | | 0 | 10 | 20 | 30 | 40 | 50 | 60 | 70 | 80 | 90 | 100 |
|---|---|---|---|---|---|---|---|---|---|---|---|---|
| **MCO** | | 0 | 8 | 14 | 25 | 34 | 37 | 54 | 66 | 79 | 89 | 100 |
| **TCO-MCO** | | 0 | 0.2 | 0.2 | 0.17 | 0.15 | 0.14 | 0.1 | 0.06 | 0.01 | 0.01 | 0 |
| **TCO** | | | | | | | | | | | | |

Note that terbium is being added into the ceria as oxide but because of the variation in oxide stoichiometry, dopant levels are conveniently expressed as metal mol% and this is used throughout. The difference of target and measured Tb concentration is high at low concentrations and then shows a decrease as the Tb concentration increases (Figure 5.1B).

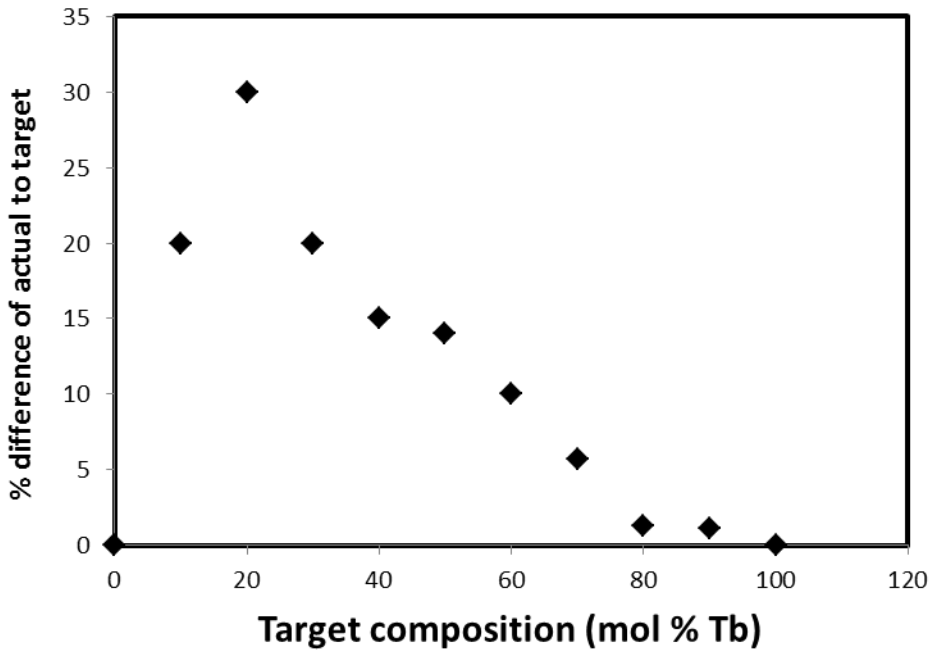


**Figure 5.1B:** The % difference of the measured composition from the target composition plotted against target composition.

This is consistent with limited (but higher than cerium) solubility of the terbium oxide-hydroxide material formed by precipitation in the basic solution. As the terbium concentration increases, the amount remaining in solution becomes less significant. This has been noted by us previously for lanthana doped ceria materials [197]. As pointed out in that paper, this solubility issue needs careful consideration in preparing these materials but is seldom reported.

Unlike lanthanum, praseodymium and cerium oxides, the structural chemistry of

terbium oxides has been infrequently studied and there is less detailed understanding of the defect chemistry and non-stoichiometry of this system. As sourced or synthesised material is generally described as $Tb_4O_7$ but the actual stoichiometry can vary from $TbO_{1.5}$ to $TbO_2$ (depending on synthesis and treatment conditions) and can be described by an homologous series of superstructures given by $Tb_nO_{2-n}$ although identification of these phases is far from certain [198, 199, 200, 201]. It is generally accepted that the lattice parameter varies linearly with composition from 5.359 ($Tb_2O_3$) to 5.213 Å ($TbO_2$) [198]. Vicker and Ruben's data agrees reasonably well with this [201] as does Gutley and Eyring's although the assignment of stoichiometry of the phases in the latter work is not the same as in the former suggesting, for example, that the $Tb_4O_7$ phase is best described as $TbO_{1.74}$ rather than $TbO_{1.75}$. The data from Gruen *et al.* [198] will be used as for standardisation here and are plotted in Figure 5.2(A).

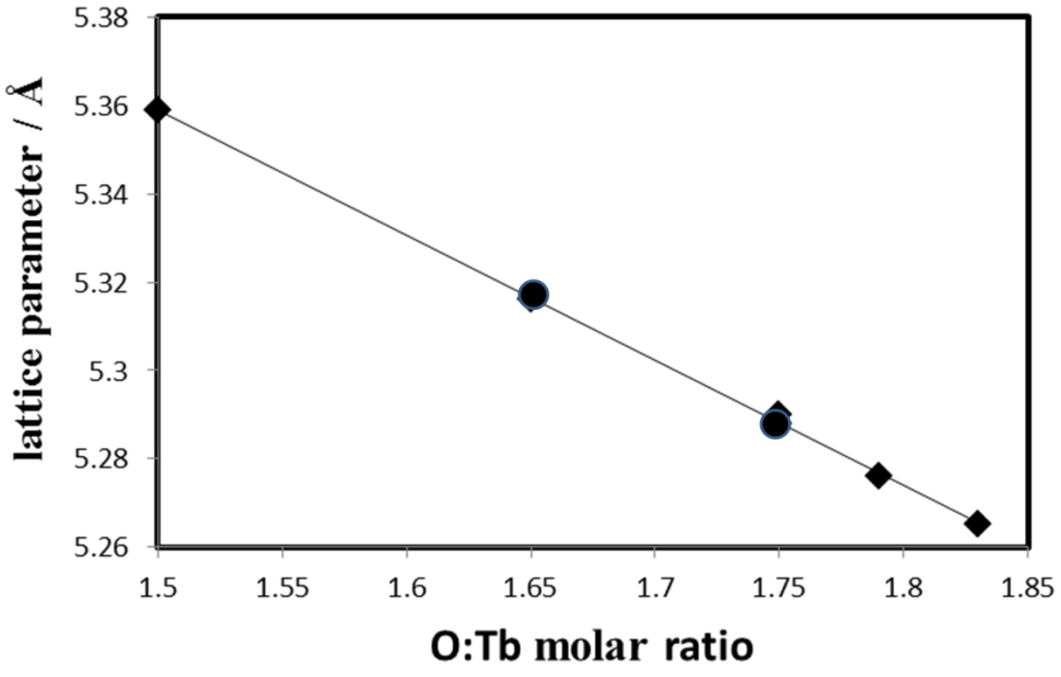


**Figure 5.2A:** Plot of lattice parameter versus O:Tb molar ratio from the work of Gruen *et al.* [198] (diamonds). Points marked with circles are data from this paper.

XRD data from the terbium only containing sample (CTB) calcined at 1100°C prepared in this work are shown in Figure 5.2(B) (and expanded form in the insert). The data display reflections are typical of fluorite-like phases but on expansion it can be seen the features are complex and made up of at least three different individual reflections resulting from the presence of three similar phases.

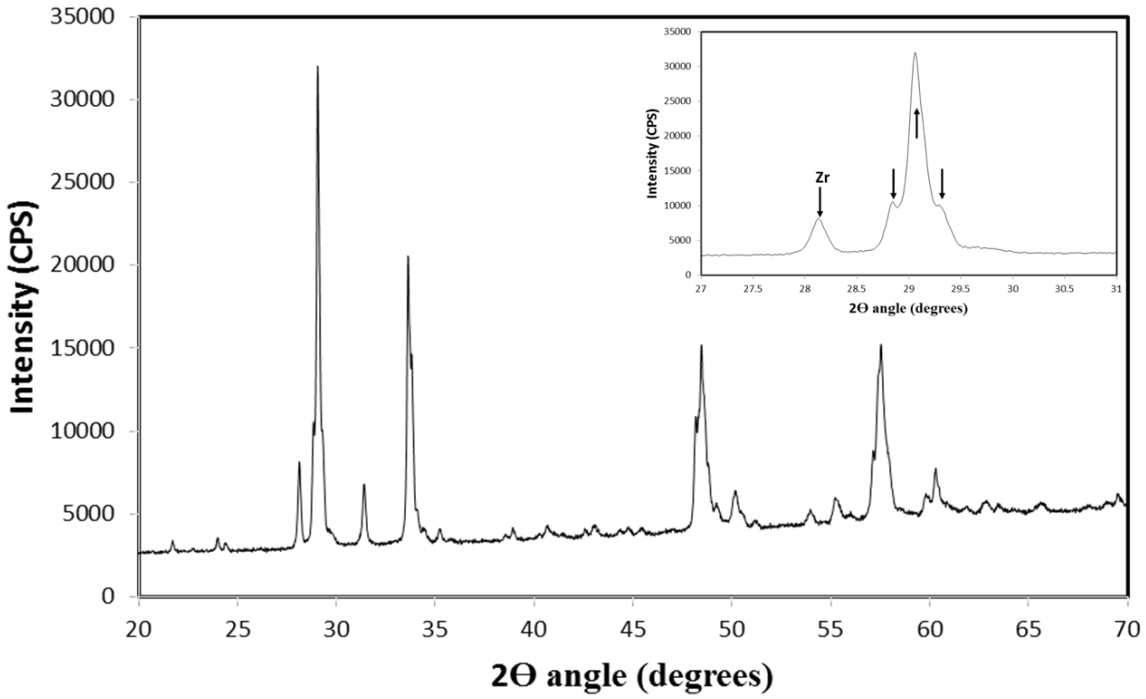


**Figure 5.2B:** XRD data of CTB sample (terbium oxide) prepared as other samples and calcined at 1100 °C. Insert shows expanded form of data of reflection around 29 °2Θ. Zr indicates a $ZrO_2$ reflection from standard and the other arrows mark three reflections from three similar phases.

The lattice parameters of these phases are determined at 5.2879, 5.250 and 5.220 Å and (using data in Figure 5.2(A)) are consistent with stoichiometries of $TbO_{1.75}$

($Tb_4O_7$), $TbO_{1.875}$ ($Tb_8O_{15}$), $TbO_{1.98}$ (~$TbO_2$). The $Tb_4O_7$ phase is expected, as is the $Tb_8O_{15}$ phase and other authors have reported this [202, 203]. Its' observation here suggests it is a metastable phase. The $TbO_{1.98}$ phase probably represents close to stoichiometry within experimental error. The formation of this mixed phase structure probably reflects complex oxidation and reduction phenomena during heating and cooling in air but does not necessarily reflect the thermodynamic stability of the $Tb_nO_{2-n}$ stoichiometry.

PXRD data for a series of ceria samples with increasing terbia concentration following calcination at 1100°C are shown in Figure 5.3(A). All reflections are consistent with a single cubic fluorite phase (JCPDS file 34-394) being present and indicate the formation of a solid solution across the entire composition range without any evidence of a solubility limit. As the terbia concentration increases, the reflections move to higher 2θ angles consistent with a decreasing lattice parameter.

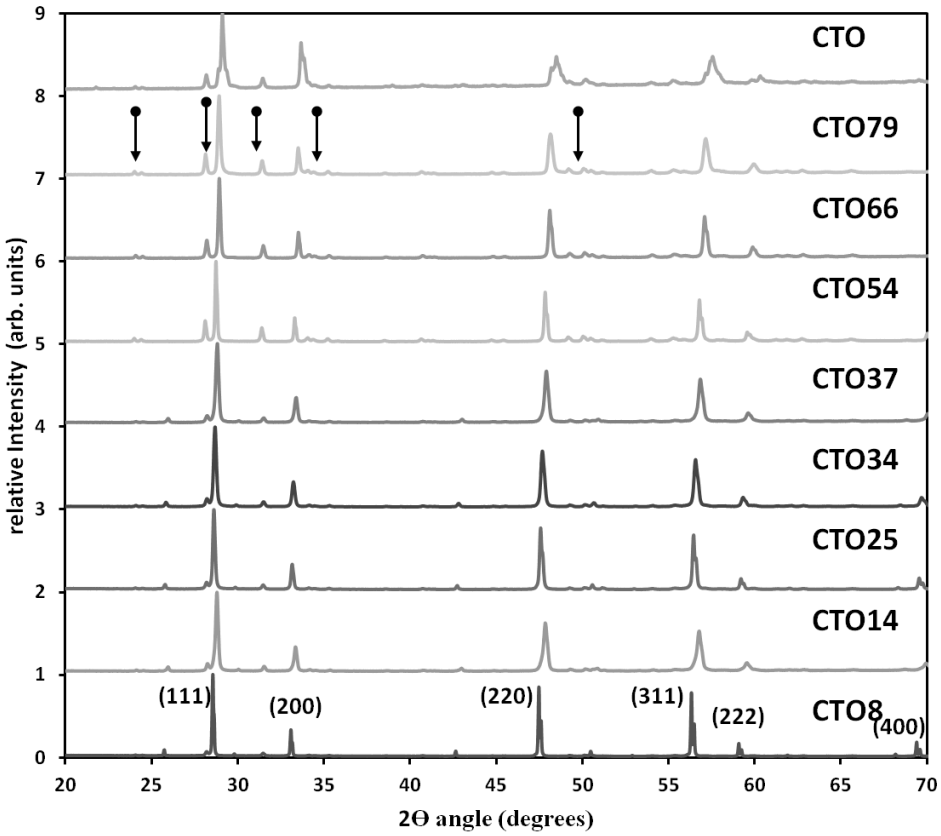


**Figure 5.3A:** Representative XRD data as a function of terbia content following 1100 °C calcination. Samples as indicated in figure. Arrows mark some of the zirconia features added as an internal reference. The fluorite reflections are indicated for the CTB sample

Note that when the terbia is added to ceria, there is no evidence of new or overlapping features that are indicative of complex superstructure. This observation suggests that any anions vacancies introduced by cation substitution are randomly distributed through the structure, at least at these larger (i.e. higher calcination temperature, as below) particle sizes but TEM data does suggest the possibility of local regions of vacancy ordering as detailed below. The decreasing lattice parameter as a function of terbia content seen in Figure 5.3(A and B) is expected since both cubic $Tb_2O_3$ (5.395 Å [201]) and $TbO_2$ (5.213 Å [201]) have smaller lattice parameters than $CeO_2$ (5.411 Å). In Figure 5.3(B) the data are quantitatively described and it can be seen that the lattice parameter decreases linearly with the terbia content. The

linearity of the plot suggests that the terbium is added into the ceria lattice in the same way at all compositions. The linearity of the plot can be used to estimate a lattice parameter of 5.251 Å at 100 mol% Tb (this is almost identical to the one of the phases observed in the 100% terbium oxide sample). Since this indicates formation of the $Tb_8O_{15}$ phase, it is consistent with the addition of both $Tb^{3+}$ and $Tb^{4+}$ cations into the lattice.

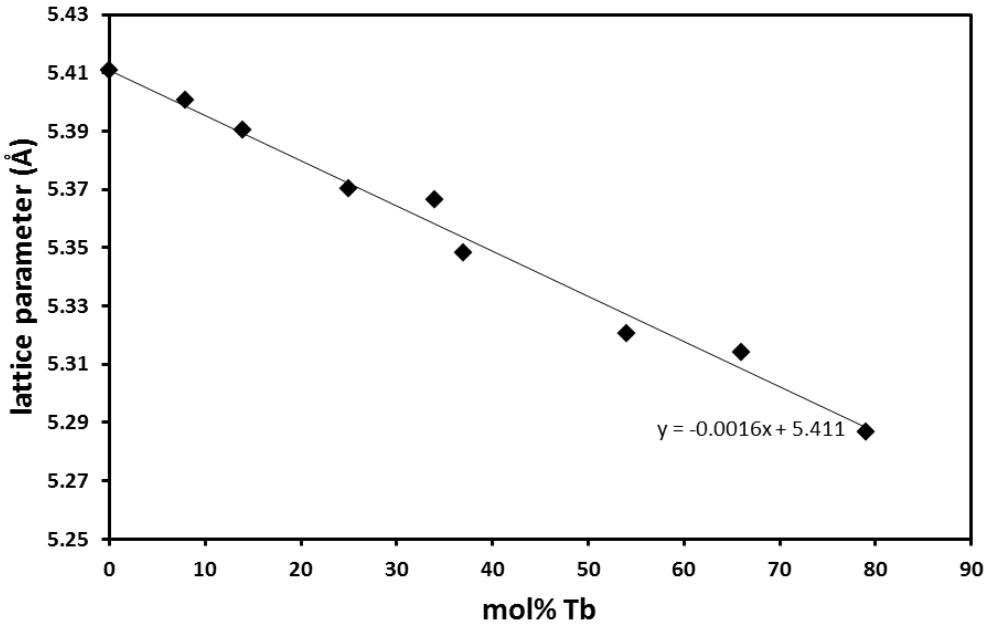


**Figure 5.3B:** Lattice parameter against mole% Tb at 1100 °C (broken line) and 700 °C (solid line).

Whilst this mixed valence incorporation has been suggested by other authors, the data presented here indicate that 1/4 of the terbium is added as $Tb^{3+}$ and 3/4 as $Tb^{4+}$ at all loadings and this is the first time this has been properly quantified. It should also be noted, since only a single phase of the materials is observed (single peak for each reflection observed) at all loadings that even small amounts of ceria can stabilise the terbia stoichiometry towards $Tb_8O_{15}$.

If data from samples calcined at 700 °C are compared to those at 1100 °C, it is apparent that the lattice parameter measured is consistently around 5% lower than that

recorded for the higher calcination temperature. We have shown that the lattice parameter of ceria is highly sensitive to crystallite size [175, 196] and in order to understand the dependence further it is necessary to quantify the variation in crystallite size variation with both composition and temperature. As can be seen in Figure 5.3(A), as the terbium content increases there is a well-defined broadening of the reflections associated with a decrease in crystallite size. Using Scherrer formulism to quantify the data, the crystallite size of samples of different composition following an 1100 °C calcination is shown in Table 5.2 and plotted in Figure 5.4(A) as ln(crystallite size) against 1/(terbium content).

**Table 5.2:** Crystallite size (nm) as measured after an 1100 °C calcination versus measured terbium concentration (mol %)

| **Mol% Tb** | 3 | 8 | 10 | 14 | 25 | 34 | 37 | 54 | 66 | 79 | 89 | 100 |
|---|---|---|---|---|---|---|---|---|---|---|---|---|
| **Crystal Size (nm)** | 364 | 116 | 102 | 86 | 79 | 75 | 72 | 70 | 68 | 66 | 64 | 50 |

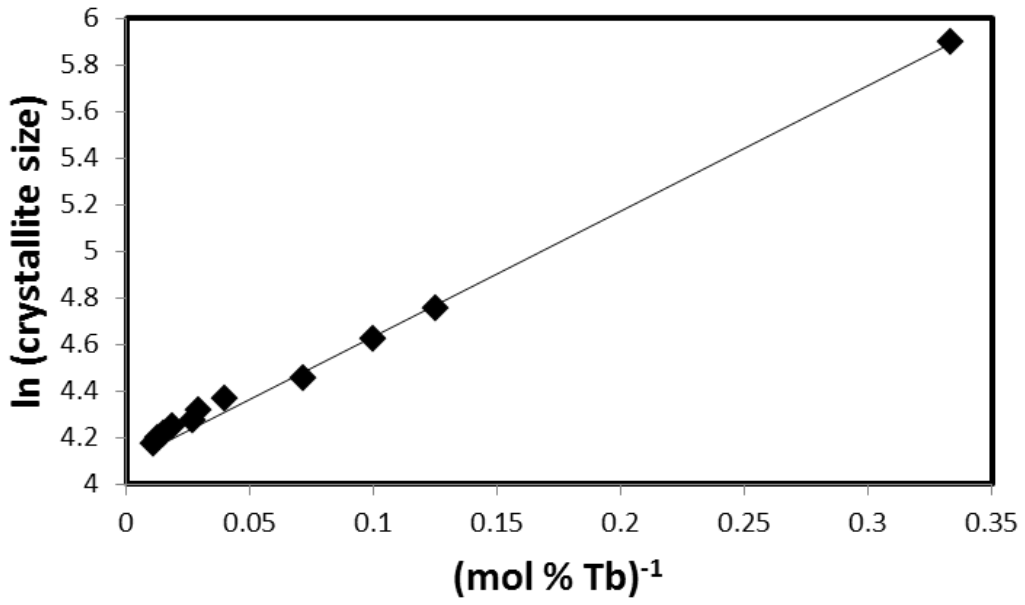


**Figure 5.4A:** Relationship between the ln of crystallite size versus amount of terbia addition to the ceria lattice.

The crystallite size measured decreases with increasing terbia concentration. This is typical of ceria doped with other lanthanides [204]. Assuming the particle size is a

simple measure of rate (since all heating periods were the same) and that the activation energy of the process is given by a linear variation with Tb content, $\Delta H_{act}$ (1 + CΘ). Here, $\Delta H_{act}$ is the activation energy at zero terbia content, C is a constant and Θ (mol% Tb) is the terbia content. Then a simple Arrhenius treatment gives:

$$\text{Particle size} = \nu \exp(-\Delta H_{act}(1 + C\Theta)/RT) \qquad \text{Eq. 5.1}$$

It is possible to estimate the value of $-\Delta H_{act}$ and C by measuring an activation energy for one of the samples. Data shown in Table 5.3 and Figure 5.4(B) represent the variation in particle size for the CTB10 sample as a function of calcination temperature.

**Table 5.3:** Crystallite size (nm) versus calcination temperature for sample CTB10

| **Temperature (K)** | 550 | 600 | 650 | 700 | 800 | 850 | 900 | 1000 | 1100 |
|---|---|---|---|---|---|---|---|---|---|
| **Crystal Size (nm)** | 18.9 | 27.9 | 29.9 | 36 | 56.2 | 78.6 | 86.1 | 105 | 124 |

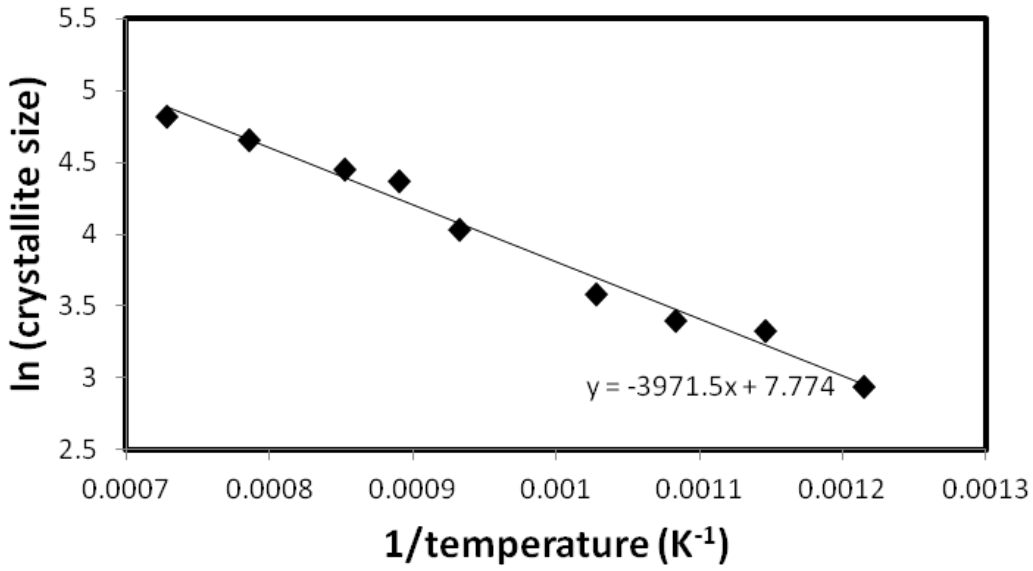


**Figure 5.4B:** Arrhenius relationship for change in calcination temperature (CTB10 sample)

Arrhenius kinetics can be used to estimate the activation energy for sintering at this Tb concentration at about 33.0 kJ $mol^{-1}$. Using the data in Figure 5.4(B) the activation energy for sintering at any Tb content can be written as $\Delta H_{act,\Theta} = 32.9\ (1 + 0.0027\ \Theta)$ kJ $mol^{-1}$. It is noted that this is not a true 'activation energy' because true equilibrium has probably not been achieved in these calcination treatments.

It is apparent from this data that there is dependence of the lattice parameter measured and the crystallite size. Using the data from Table 5.3 (for the CTB10 sample) and measuring the lattice parameter from the individual data sets shown in Figure 5.5(A), the lattice parameter as a function of crystallite size can be plotted (Figure 5.5(B)). It can be seen that the lattice parameter increases monotonically with size before reaching a plateau at the highest particle sizes.

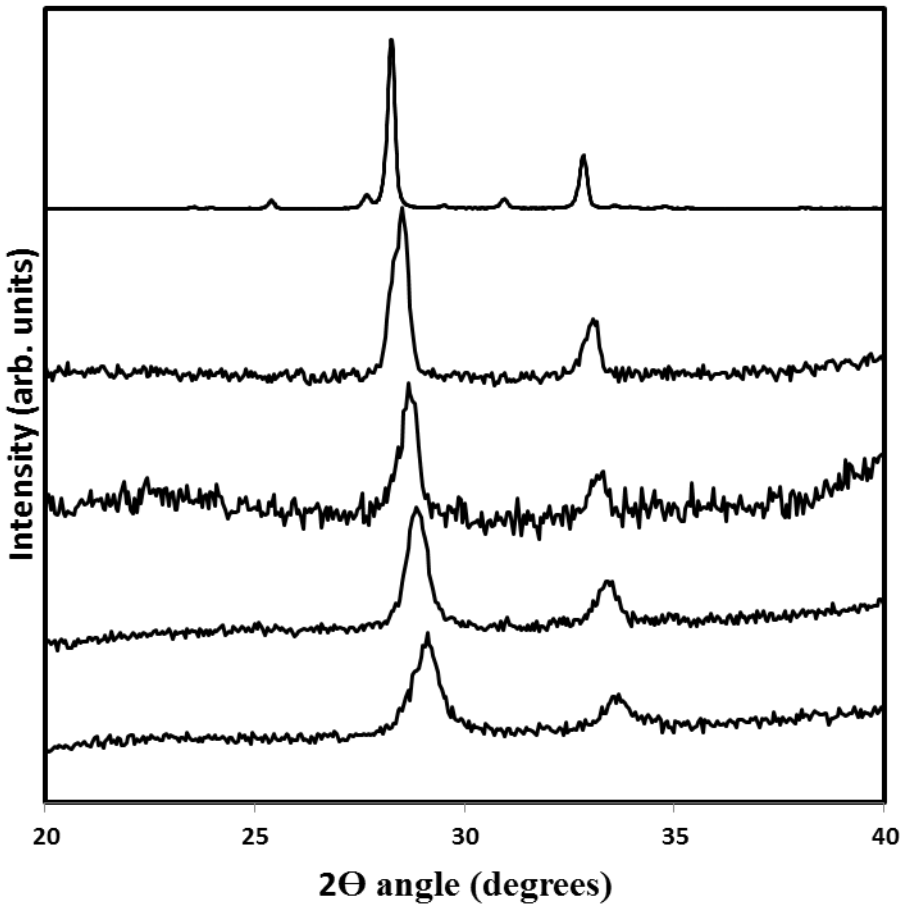


**Figure 5.5A:** Representative XRD data as a function of calcination temperature (from bottom 600, 700, 800, 900 and 1100 °C) for the CTB10 sample

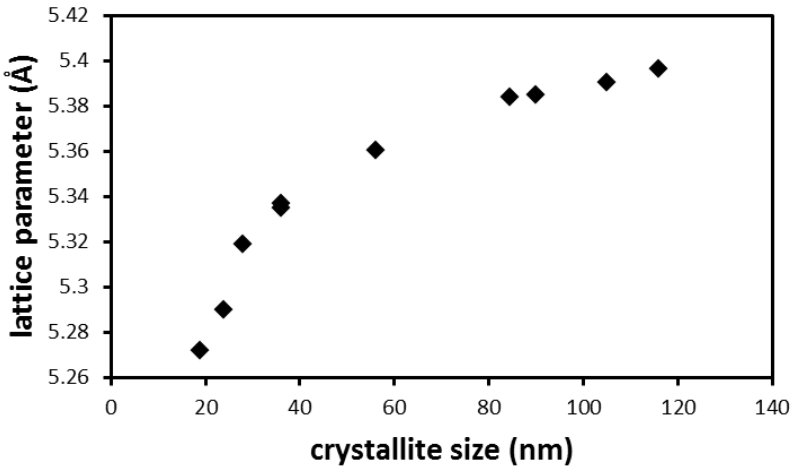


**Figure 5.5B:** Lattice parameter against crystallite size for the CTB10 sample

$CeO_2$ has been reported to exhibit both a decreasing and increasing lattice parameter with increasing crystallite size and there has been much debate on the origin of these effects [175]. Morris *et al.* suggest that $CeO_2$ decreases in lattice parameter as particle size decreases due to surface tension effects but this can be masked by presence of hydroxyl, carbonate and other groups due to preparation [175]. The alternate view is that anion vacancies and accompanying, larger $Ce^3$-like states bring about lattice expansion [205]. The lattice contraction due to crystallite size reduction (5.3963 Å at 116 nm to 5.27195 at 18.9 nm) observed here is significant at around 2.3% and clearly much less the value expected if all of the terbium was added as $Tb^{4+}$ (5.391 Å assuming the lattice parameter of $TbO_2$ = 5.213 Å (Figure 5.2(A)) and cannot be explained by a variation of the terbium oxidation state as a function of calcination temperature. Since lattice contraction cannot be achieved by changing the valence of cerium cations, it is very clear that the contraction is caused by either surface tension or quantum size effects in small crystallites [175, 196, 206].

The data also suggests that significant quantities of $Ce^{3+}$ in the samples would be needed to prevent observation of such large lattice parameter decreases. This can be calculated from simple consideration of the measured lattice parameter values and

half the value of the lattice parameter of cubic phase $Ce_2O_3$. (viz. 11.2 Å [205]) using the equation:

$$5.2795(1-x) + 5.605\,(x) = 5.3963 \qquad \text{Eq. 5.2}$$

x evaluates at about 37%. Since the surface volume (assuming it is one lattice parameter thick) to bulk volume ratio for an 18.9 nm diameter crystallite assuming a spherical shape is around 51%, it is obvious that neither the surface or the bulk can be substantially reduced or else such strong dependence on crystallite size would not be observed. Indeed, there is little evidence for any gross $Ce^{3+}$ concentration in these materials (see below).

TEM micrographs support the XRD structural data. Illustrative data are seen in Figure 5.6 for the TBO37 sample. Figure 5.6(A) shows a micrograph (dark field view) of a large aggregation of several smaller crystallites formed after a 1100 °C calcination. These aggregations are typical of the high temperature calcination of ceria as is the crystallite morphology of 3D polyhedra [207]. The edges of some of the individual crystallites making up the aggregation have been indicated in Figure 5.6(A). As can be seen, there is a high degree of crystallite size polydispersity ranging from 25 to 300 nm. However, the average crystallite size measured from several micrographs is about 90 +/- 30 nm in general agreement with the XRD determination. High resolution studies show the single crystal nature of these individual crystallites (Figure 5.6(B) and 5.6(C)) and lattice planes are easily observed. In no micrographs recorded for 1100 °C calcined materials (largest particle sizes) were there obvious indications of any complex superstructures indicative of ordered arrangements of anion vacancies. The lattice spacing determined here (<100> direction shown) was 5.346 Å in very good agreement with the XRD determined value of 5.348 Å (Figure 5.3(B)) and in general all TEM and XRD measurements agreed to less than .02 Å.

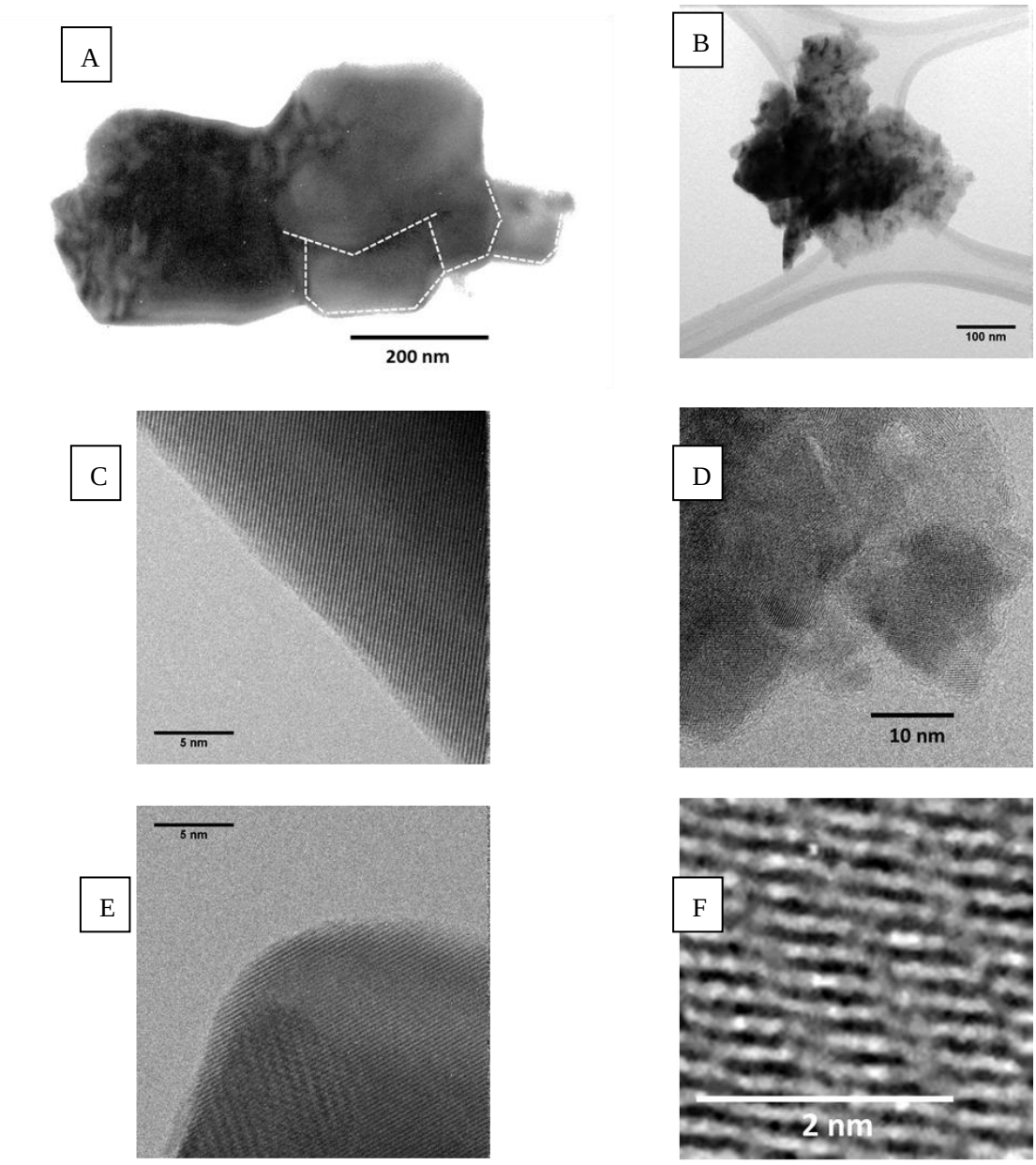


**Figure 5.6:** TEM micrographs of CTB37 samples after calcination at 1100 °C ((A)-(C)) and 650 °C ((D)-(F)). Scale bars as shown and further details in text.

The CTB37 material calcined at 650 °C also showed good agreement with XRD data. Data are also shown in Figure 5.6. Figure 5.6(d) shows a low resolution image typical of aggregations of smaller crystallites. The average size of the crystallites was between 5 and 30 nm with an average value of 23 +/- 5 nm in agreement with the XRD data. Higher resolution images (Figure 5.6(E)) show the highly crystalline

nature of these smaller particles. Measurement of the lattice parameter from these images is difficult because of size variation from crystallite to crystallite and the sensitivity of lattice parameter to size noted above. However, an average value of 5.299 Å is in reasonable agreement with a value of 5.290 Å (Figure 5.5(B)) measured by XRD on similar materials and confirm the observation of lattice contraction at small crystallite dimension. Where the smaller crystallite data differs from larger crystallites is that local regions (normally a few $nm^2$ in area) of higher periodicity typical of ordered vacancy superstructures can be occasionally observed in the TEM images. An example can be seen in Figure 5.6(F) where a small but regular displacement of lattice lines (running from top left to bottom right) can be observed. A comparison between small and large crystallites is shown in the graphical abstract. Similar, complex TEM images have been observed previously for complex terbium oxide phases that exhibit anion vacancy ordering [203]. It is possible that these ordered superstructures are also present for larger crystallites but are not observed because either greater thickness which results in intensity averaging or that higher temperature calcination results in increased ion diffusion and randomisation of any ordered vacancy structure [178]. Alternatively, the smaller size of the crystallites may present a lower mass transport barrier to the formation of low energy superstructures.

It can also be concluded from the TEM data presented here, that there is little sign of formation of either an amorphous layer or significant segregation at the surface of the crystallites. Other authors have suggested extensive surface segregation and precipitation for the terbia-ceria system but this is at higher treatment temperatures [188, 189] and there is no sign of new phase production in either TEM or XRD. Lanthana is known to segregate from ceria and this is driven by larger 3+ ions and the reactivity of lanthana to hydroxide and carbonate [177, 195, 197, 208]. It might be concluded, lattice strain in terbia doped ceria is lower than that seen for the larger lanthanide 3+ ions since solubility extends over the whole of the dopant range compared to those systems. It would thus appear that, the addition of terbium oxide

does not cause any gross changes in surface structure or composition in the surface region in the temperature range studied in this work.

XPS provides further detail on the structure and composition at the outermost regions of the crystallites. Tb3d spectra provided little information. These are difficult to tell apart because the main features are at almost identical binding energies and are only differentiated by careful analysis of weak satellites requiring detailed analysis [184]. Without being able to isolate individual data sets from $Tb_2O_3$ and $TbO_2$, quantification of the relative concentration of 3+ and 4+ valence states was not possible. However, it was possible using Ce3d and O1s XPS data to assess whether the materials (because of the terbium ion inclusion) showed evidence of significant anion vacancy inclusion beyond that associated with $Tb^{3+}$ ions and if the terbium substantially altered the amount of hydroxyl, carbonate and other oxygen containing species in the surface region. Illustrative Ce3d and O1s data are given in Figure 5.7 (A and B). Ce3d photoelectron spectra from cerium oxide materials have an intricate multiplet structure because of final state effects. For convenience, we follow Burroughs *et al.* in the assignment of these [209].

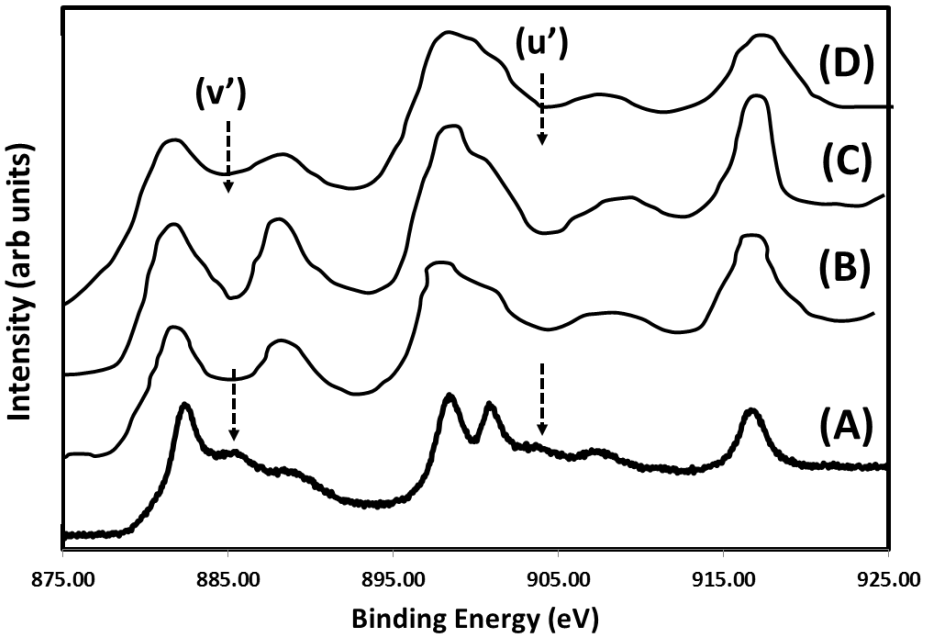


**Figure 5.7A:** Ce3d XPS spectra of various samples. (A) CEO-RED, a sample containing significant $Ce^{3+}$ states, (B) CTB34, (C) CTB54 and (D) CEO-OX an oxidised ceria sample

Two features marked in Figure 5.7(A), u' and v' derive from $Ce^{3+}$ states. As well as illustrative data from two Tb containing sample (CTB34 and CTB54) comparative data from ceria only samples in reduced form (CEO-RED) and an oxidised from (CEO-OX) are also shown. These data are described in detail elsewhere [175]. The u' and v' features are clearly visible in the CEO-RED sample and not in the CEO-OX sample as expected. Visible inspection shows that the Tb containing materials have amounts of $Ce^{3+}$ equal to or less than the ceria only sample following extensive oxidation. By comparison to our previous work [195] it is suggested that there is less than 5% cerium ion present in the trivalent state. Thus, there is no evidence that terbia loading significantly increases the reactivity of the ceria and promotes either anion vacancy formation or reaction to $Ce^{3+}$ compounds. This is confirmed by O1s photoelectron spectroscopy data (Figure 5.7(B)).

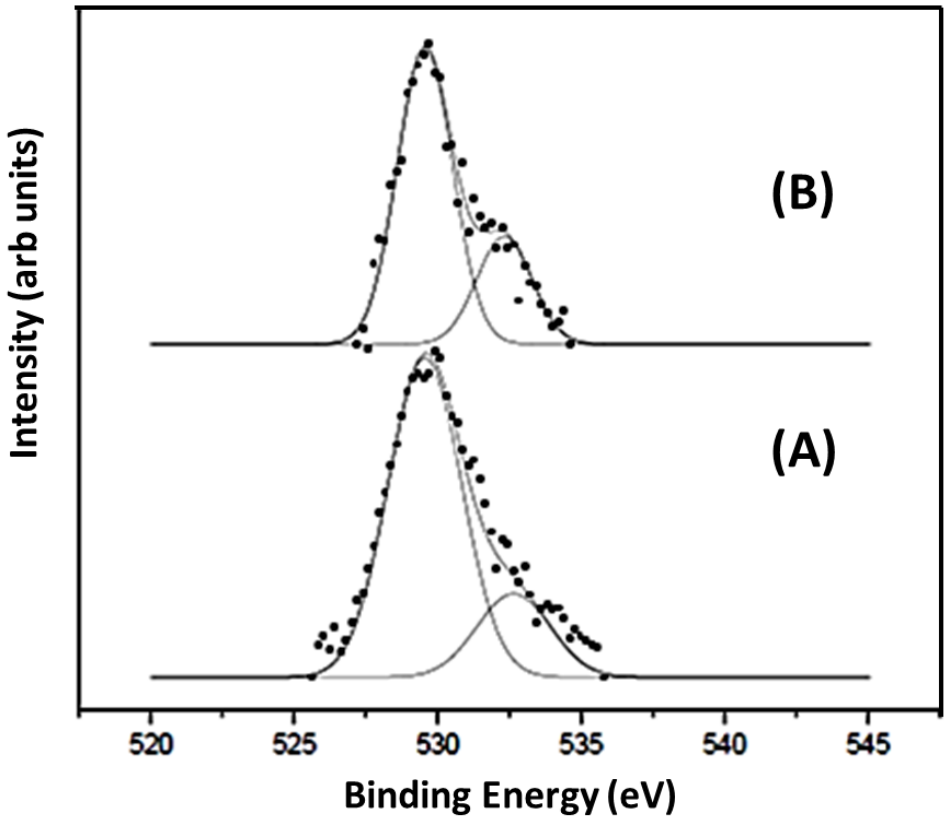


**Figure 5.7B:** O1s XPS data for (A) CTB34 and (B) CTB54

Two features can be resolved at binding energies around 530.0 and 532.5 eV that can be respectively assigned to lattice oxygen and oxygen associated with adsorbed hydroxyl or carbonate species [195]. Curve-fitting (as shown) allows the surface coverage to be estimated and this is consistent with around a monolayer of adventitious adsorption of these species. This is expected as the samples were exposed to the laboratory atmosphere for several hours. It this seems that terbia addition has little effect on the chemical activity of the samples and this was observed over the whole of the composition range.

## 5.6 Discussion and Conclusions

The effect of terbia doping of ceria on the chemical reactivity is somewhat different than that reported for lanthana and other lanthanide $Ce^{3+}$ ions [195, 210]. No enhanced ceria reduction was observed here and this is consistent with the work of Martínez-Arias *et al.* [184], Guo *et al.* [185] and Wang *et al.* [194]. The almost passive nature of terbia in this regard is partly explained by the fact that only about ¼ of the terbium cations are in the lower valence state. Even at the highest loadings used we saw no evidence for bulk uptake of adsorbed species. Further, we saw no XPS evidence for formation of significant $Ce^{3+}$ formation (from either anion vacancy formation or compound formation) even when the ceria is the minor component of the solid solution. It should also be said that vacancies are in some way associated with terbium ions and the ion is largely in the reduced form. The terbium cation is predominantly $Tb^{4+}$ and the ratio of the two valence states (3:1) is not very different from that measured in terbia only samples. Whilst the passive effect of terbia addition probably requires detailed study, it can be tentatively suggested that this could be due to preparation rather than complex co-operative effects. It is well known that basic conditions favour Ce4+ formation over $Ce^{3+}$ and the higher basicity of $Tb^{3+}$ in the synthesis favours the higher oxidation state because of the well-known decrease in ionic radius with atomic number for this series of elements.

The amount present as $Tb^{3+}$ is significantly more than seen by other authors including Martínez-Arias *et al.* [184], Guo *et al.* [185] and Wang *et al.* [194]. Wang *et al.* [194] have also claimed that there is a variation in the relative amount of the oxidation terbium states with composition whereas this work suggests it is invariant. However, their conclusion was based on a limited number of samples and analysis of $L_{III}$ edge XANES spectra whose form, variation and dependence on structure complex. Chatzichristodoulou *et al.* [193] also suggest a variation in behaviour with composition with the relative concentration of $Tb^{4+}$ increasing with concentration.

However, since the major evidence for the terbium ion oxidation state is measurement of the lattice parameter, it is suggested that the differences in the literature (on the variation and the magnitude of changes) probably arise from crystallite size effects. The crystallite sizes are strongly dependent on temperature and composition and, as reported herein, the lattice parameter is very dependent on crystallite size.

Finally, the decrease of lattice parameter as crystallite size is reduced should be carefully addressed. Definitive assignment of either lattice expansion or contraction has proved difficult [175]. It is suggested that this is due to three main reasons [175]. The ratio of $Ce^{4+}$ to $Ce^{3+}$ (anion vacancies and or trivalent compounds) in small crystallites is highly dependent of synthesis conditions as well as their thermal treatment and ambient exposure. Thus, the lattice parameter measured is sensitive to pre-treatment and history. The stability of these samples where significant surface or bulk $Ce^{3+}$ species were never observed should allow more complete analysis of the variation in lattice dimensions with crystallite size. It is shown here that there is a clear lattice contraction at small dimension consistent with surface tension effects. This is a significant result and suggests that, in general, this lattice contraction should be expected in the absence of other effects. Authors have suggested that lattice expansion at small crystallite dimensions suggests that $Ce^{3+}$ is the more stable state at the surface of small crystallites and nanoparticles. This work suggests this is not a general explanation and if vacancies do exist they are formed and maintained only in carefully controlled environments.

# 6 Chapter 6 - Size-Related Lattice Parameter Changes and Surface Defects in Ceria Nanocrystals

This chapter is based on a paper which has been published in the Journal of Physical Chemistry C, 114 (2010) 12909.

## 6.1 Abstract

Ceria ($CeO_2$) has many important applications, notably in catalysis. Many of its uses rely on generating nanodimensioned particles. Ceria has important redox chemistry where $Ce^{4+}$ cations can be reversibly reduced to $Ce^{3+}$ cations and associated anion vacancies. The significantly larger size of $Ce^{3+}$ (compared with $Ce^{4+}$) has been shown to result in lattice expansion. Many authors have observed lattice expansion in nanodimensioned crystals (nanocrystals), and these have been attributed to the presence of stabilized $Ce^{3+}$ -anion vacancy combinations in these systems. Experimental results presented here show (i) that significant, but complex, changes in the lattice parameter with size can occur in 2-500 nm crystallites, (ii) that there is a definitive relationship between defect chemistry and the lattice parameter in ceria nanocrystals, and (iii) that the stabilizing mechanism for the $Ce^{3+}$ -anion vacancy defects at the surface of ceria nanocrystals is determined by the size, the surface status, and the analysis conditions. In this work, both lattice expansion and a more unusual lattice contraction in ultrafine nanocrystals are observed. The lattice deformations seen can be defined as a function of both the anion vacancy (hydroxyl) concentration in the nanocrystal and the intensity of the additional pressure imposed by the surface tension on the crystal. The expansion of lattice parameters in ceria nanocrystals is attributed to a number of factors, most notably, the presence of any hydroxyl moieties in the materials. Thus, a very careful understanding of the synthesis combined with characterization is required to understand the surface chemistry of

ceria nanocrystals.

## 6.2 Introduction

Cerium dioxide (ceria) nanoparticles have been the subject of intense research. Ceria has a host of applications, but academic interest largely stems from its use in the modern automotive catalyst. [211] It is also of significance because of many other application areas, notably, as the abrasive in the chemical-mechanical planarization of silicon substrates. [212] Recently, ceria has been the focus of research investigating health effects of nanoparticles,[213, 214, 215] and importantly, the role of nonstoichiometry in ceria nanoparticles is implicated in their biochemistry [215]. Ceria has well-understood nonstoichiometry resulting from the formation of anion vacancies [216] that, at some well-defined concentrations, form ordered superstructures based around the fluorite lattice structure exhibited by stoichiometric ceria. [217] This defect chemistry is also often defined in terms of $Ce^{3+}$ states (not strictly correct, as discussed below) that have a larger ionic radii than $Ce^{4+}$ states, and therefore, this nonstoichiometry defect chemistry in $CeO_{2-x}$ has been associated with a lattice expansion compared to stoichiometric $CeO_2$.6 Greater defect chemistry complexity is suggested by more recent work. Morris *et al.*, [218] Esch *et al.*, [219] and Namia [220] and co-workers have shown that the vacancies are mobile and this, combined with the interactions energy between the defects, may result in vacancy clustering.

Ceria in nanoparticulate form is of particular interest because of its high chemical activity and surface area. The sensitivity of the cerium electronic band structure to the environment would suggest that changes in the properties of ceria nanocrystals/particles at very small dimensions might be expected. It is rare to see ceria in anything other than a crystalline form, and it is, therefore, more appropriate to discuss the chemistry in terms of nanocrystals that may aggregate into nanoparticles.

Clearly, lattice expansion would be a property of the nanocrystals. Notably, many authors report a lattice expansion with reducing nanocrystal size (largely confined to sub-10 nm range). Most authors follow Tsunekawa and co-workers [221, 222, 223] and assign increased lattice dimensions to the presence of surface stable $Ce^{3+}$ -anion vacancy sites within a surface layer at low nanoparticle dimensions. However, there are a number of conflicting findings in the literature. A detailed understanding of these systems has yet to be attained, and their full and quantitative characterization offers serious challenges.

In this work, the results of a series of chemical preparations chosen to produce nanocrystals of different chemical nature were investigated. Indeed, we see little evidence of a consistent model emerging to explain lattice parameter changes with nanocrystal size. On the basis of these results and a review of the literature, it is worthwhile asking (a) if a model of surface enhanced defect concentration is consistent with known cerium/cerium oxide chemistries, (b) whether this is applicable to a range of different synthesis methods, and (c) if a more consistent description is possible. Herein, a novel model based on the known and the newly obtained experimental results is proposed that incorporates the possibility of forming new surface chemistries as well as nonstoichiometric surface structures together with a fundamental relationship of the lattice parameter with nanocrystal dimensions.

## 6.3 Experimental Procedure

### 6.3.1 Preparation

Three ceria synthesis methods were used in this work in order to compare a range of surface chemistries resulting from common preparation methods. Briefly, after each preparation, samples were calcined at different temperatures to produce samples of different crystallite sizes.

#### 6.3.1.1 Method One: Simple Reverse Precipitation

In the first method, a *simple reverse precipitation* was used involving the addition of aqueous solutions of $Ce(NO_3)_3$ to $NH_4OH$ solutions (large base excess so that the final concentration ratio of $OH^-$ to $Ce^{3+}$ was at least 10:1). These reverse precipitation conditions gave the smallest particulates and narrowest size dispersion. After the addition was complete, the final solution was stirred for 30 min and the precipitate recovered by filtration. In all cases, the as-formed precipitate was a pale yellow color throughout the reaction and after recovery. The recovered powder was dried overnight at 60 °C. To minimize aggregation, the product was resuspended in water by dropwise addition of concentrated nitric acid. The suspended material was recovered by filtration and dried at 80°C for 12 h. Samples were calcined at various temperatures to effect conversion of the precipitate to $CeO_2$ as well as allow variation of nanocrystal size.

#### 6.3.1.2 Method Two: Microemulsion (micelle mediated precipitation)

This is based around a *microemulsion* (*micelle mediated precipitation*) method designed to limit aggregation and the size of the ceria nanocrystals as prepared through formation of a reverse micelle structure (this is described as a micelle templated reaction). Two microemulsions were prepared by sonication using an octane oil phase and cetyltrimethylammonium bromide together with butanol as cosurfactants. Stoichiometric amounts of aqueous cerium(III) nitrate and ammonia hydroxide where added to one of the emulsions. These were mixed under stirring for 1 h. The solid was recovered as in method 1, but note that the as-formed precipitate was a purple color (typical of $Ce(OH)_3$ or $Ce_2O_3$) that slowly turned yellow on stirring.

#### 6.3.1.3 Method Three: Liquid phase direct precipitation (LPDP)

This is based around a novel *liquid phase direct precipitation* (LPDP) technique developed in our laboratory that provides a means to control the oxidation state and stoichiometry of the product. [224] Very briefly, ultradry nonaqueous solvents (methanol in this case) are used, and a reaction proceeds directly between a metal cation (from addition of the chosen metal salt, here, $CeCl_3$) and $O^{2-}$ anions (from "dissolved" $Na_2O$) to directly yield the metal oxide. In anaerobic conditions and provided that stoichiometric quantities are used, no oxidation/reduction is possible and the oxide product has the oxidation state of the initial metal salts in this case, $Ce_2O_3$. Briefly, two solutions of methanol each containing either the metal salt or $Na_2O$ were prepared separately, mixed, and stirred at room temperature for about an hour. The oxide product (a strong purple color until recovered and exposed to air) was collected by precipitation, followed by washing in methanol. For preparation of reduced materials (i.e., $CeO_{2-x}$), the filtration and washing were carried out under argon to minimize air oxidation.

## 6.4 Analyses

Powder X-ray diffraction (XRD) data were collected using a Philips X'Pert diffractometer with Cu KR radiation (anode current of 40 mA and an accelerating voltage of 40 kV) in standard $\theta$-$2\theta$ mode. For accuracy in measurement of very small lattice shifts, all measurements were internally referenced to zirconia reflections from small amounts of $ZrO_2$ (calcined at 1200 °C for 24 h) added to the sample as a fine powder. Lattice parameters were measured by a least-squares method from reflections in the 20-70° $2\theta$ range. [225] This very exact approach is a necessary prerequisite to obtaining an adequate accuracy of results. $N_2$ adsorption-desorption experiments were performed using a Micromeritics Gemini 2375 volumetric analyzer. The samples were pretreated at 100 °C for 4 h, and the specific surface area of the samples was determined using the Brunauer-Emmett-Teller (BET) method. The pore volume and pore size distribution were derived from the adsorption profiles of the isotherms using

the Barrett-Joyner-Halanda (BJH) method. Transmission electron microscopy (TEM) micrographs were collected using a JEOL JEM-200 FX or a JEOL 2010 TEM microscope operated at 200 kV. The samples were dispersed in ultradry methanol, sonicated, and dropped onto copper grids coated with a holey carbon film. Thermogravimetric (TGA) and differential thermal analysis (DTA) data were collected on a Labsys TG-DTA Instruments using a heating rate of 5 °C $min^{-1}$. Temperature-programmed desorption (TPD) analysis was performed via heating (heating rate of 15 °C $min^{-1}$) of 0.2 g of the sample in a packed stainless shell tube in flowing helium (25 mL $min^{-1}$), the products being analyzed using a quadrupole mass spectrometer. X-ray photoelectron spectroscopy (XPS) studies were carried out on a VSW system using Al KR radiation and a pass energy of 50 eV. Samples were exposed to X-rays for as brief a period as possible to avoid X-ray/electron induced reduction. No change in the Ce 3d spectra from the beginning to the end of the collection period was observed in all cases. Samples were pressed into 1 cm disks at 10 t pressure per cm-2 and mounted onto stainless steel stubs held on using tantalum wires. Samples were heated to 110 °C for 8 h in the UHV chamber for 8 h to remove any adventitious water in the samples. Binding energies were referenced to a C 1s signal at 285.0 eV.

## 6.5 Results

Typical XRD profiles are shown in Figure 6.1 from synthesis via the *simple reverse precipitation* method (method 1). All the profiles are consistent with the fluorite phase expected of $CeO_2$ (JCPDS file No. 04-0593). The plot shows the effect of calcination on the as-synthesized, harvested, and dried product. As can be seen, the broad peaks demonstrated by the as synthesized and dried sample narrow as a function of heating, typical of crystallite growth and increased order within the sample. Crystallite sizes were calculated using the Scherrer formulism.

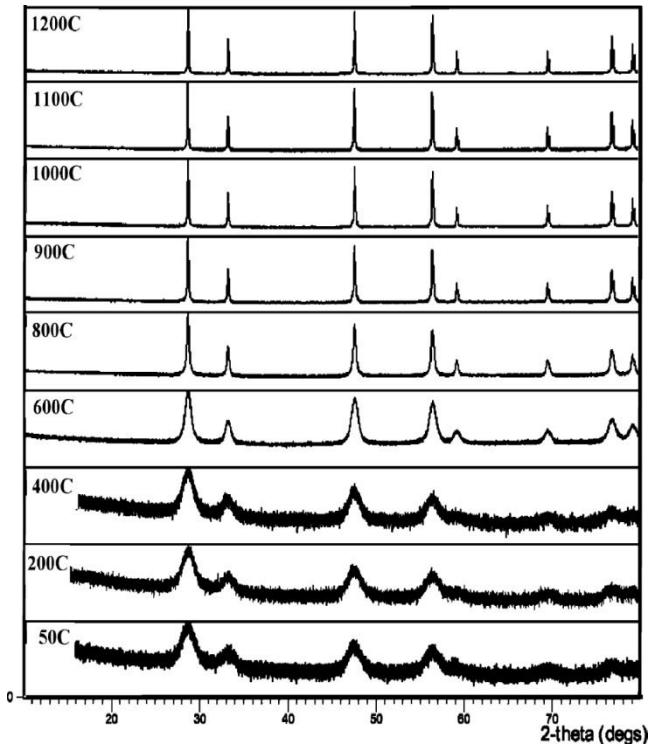


**Figure 6.1**: Powder X-ray diffraction patterns of CeO2 nanocrystals synthesized by the reverse precipitation method (method 1) as a function of calcination temperature (C denotes °C) after precipitate recovery and drying.

The XRD calculated crystallite sizes of the samples after calcination agree well with the measurement of crystallite size by TEM (see below, Figure 6.4). The reason for this agreement is probably because the product of the simple salt plus base reactions (methods 1 and 2) appears to be almost exclusively dense nanocrystals that are highly crystalline with little amorphous or porous character. This is further demonstrated in Figure 6.2 where the surface area calculated from the estimated Scherrer-derived crystallite size (assuming spherical and 100% dense material) is compared to BET-derived surface areas for the *microemulsion* preparation route. The agreement is reasonable through the heating temperature range and within experimental errors after a 400 °C treatment. The small increased surface area from BET compared with Scherrer estimates may reflect shape anisotropy of the crystallites (relatively small, see below), limited porosity, or the presence of some very small crystallites/amorphous particles not observed in XRD. These results do suggest that these *simple precipitation* reactions do form relatively stable, well-ordered $CeO_2$

nanocrystals.

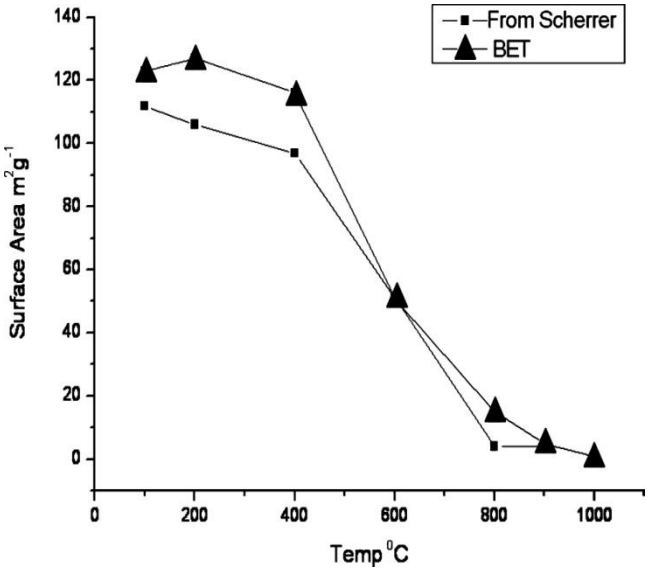


**Figure 6.2:** Relationship between the overall surface area of CeO2 crystals and the calcination temperature as estimated by BET (prepared by method 2) and Scherrer analyses (prepared by method 1).

As can be seen in Figure 6.2, the surface area of the nanocrystals (and also their size) changes quite slowly on heating between room temperature (RT) and 400 °C but then dramatically decreases between 400 and 600 °C. The surface area always shows a small increase on heating to around 100 °C. DTA/TGA data show that these changes are due to changes in material composition. Data for a precipitated and dried sample are shown in Figure 6.3A. The first significant weight loss (1.7%) and associated endotherm are seen between 80 and 110 °C. This can be readily assigned to dehydration and loss of weakly adsorbed water. The second major weight loss (2.66%) and endotherm are observed in the 300-600 °C temperature range with a peak around 414 °C. This weight loss and endotherm are associated with the loss of

water-derived species from the material, as is confirmed by TPD where, desorption features typical of water are observed at around the same temperature (Figure 6.3B).

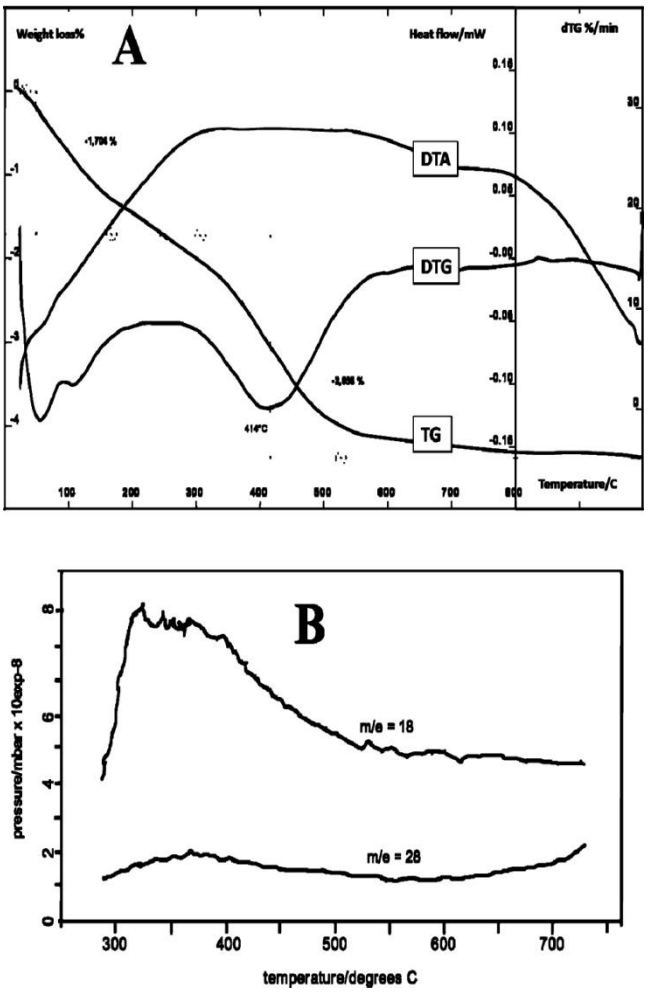


**Figure 6.3**: **(A)** Thermal analysis data, including weight loss (TG), its differential (DTG), and differential thermal analysis (DTA), from an as-dried ceria nanoparticulate sample; weight losses as indicated.

**(B)** Temperature-programmed desorption (TPD) data from a similar sample. Data for *m*/*e*) [18] are shown. The *m*/*e*) [28] data are given and are indicative of background desorption.

Note that the peak temperature observed for desorption in TPD (360 °C) is somewhat lower than that for weight loss seen in TGA (414 °C). This is directly attributable to the higher heating rate used in the TPD experiments. In this way, the rapid loss of surface area (Figure 6.2) can be related to the decomposition of a hydrous material. Similar thermal analysis data were observed for $La(OH)_3$, and it can be suggested that these data are consistent with the decomposition of stable hydroxyl species (see below), such as $Ce(OH)_3$, $Ce(OH)_4$, or $CeO_2 \cdot 2H_2O$ (or similar, as these phases may not be existent in these simple stoichiometric formulas, as discussed further below). This de-hydroxylation of the samples could be partially verified using infrared spectroscopy, but this was largely non-quantitative because of rapid reaction of water on ambient exposure. It is important to emphasize that the weight losses observed are relatively small. Assuming a spherical and dense nanocrystal shape (the particle porosity is small, as evidenced above and in TEM data below) and that four water molecules are adsorbed per surface unit cell (equating to one $H_2O$ molecule per surface oxygen or two per surface cerium ion), a 4-5% weight loss would be observed by a 6-7 nm nanocrystal losing water from the surface. The crystallite size (as determined by the Scherrer formulizm) measured after 400 °C calcination for this *simple precipitated* sample is 5.6 nm. It would, thus, seem that these nanocrystals are essentially dense $CeO_2$ with a hydroxylated surface. Similar data and agreement were obtained for microemulsion prepared samples.

Confirmation of this description of the samples can be gained from TEM micrographs. Typical data are shown for simple precipitated material in Figure 6.4A (includes an indexed Fourier transformation pattern) and Figure 6.4B from samples calcined at 350 and 650 °C, respectively. Figure 6.4C shows a typical darkfield image of the ceria nanocrystals and suggests highly crystalline centers, many of which are single grains rather than being polycrystalline in nature. The high-resolution images shown are indeed typical of highly crystalline $CeO_2$ and are seen throughout the calcination temperature range used. The nanocrystals are polyhedra displaying (111) and (200) facets as indicated. The effect of the higher temperature calcination is

crystallite growth and extension of the facets. A feature to note is that, at the surface of the facets, a “fuzzy” layer can be observed (white arrows in Figure 6.4A and 6.4B)

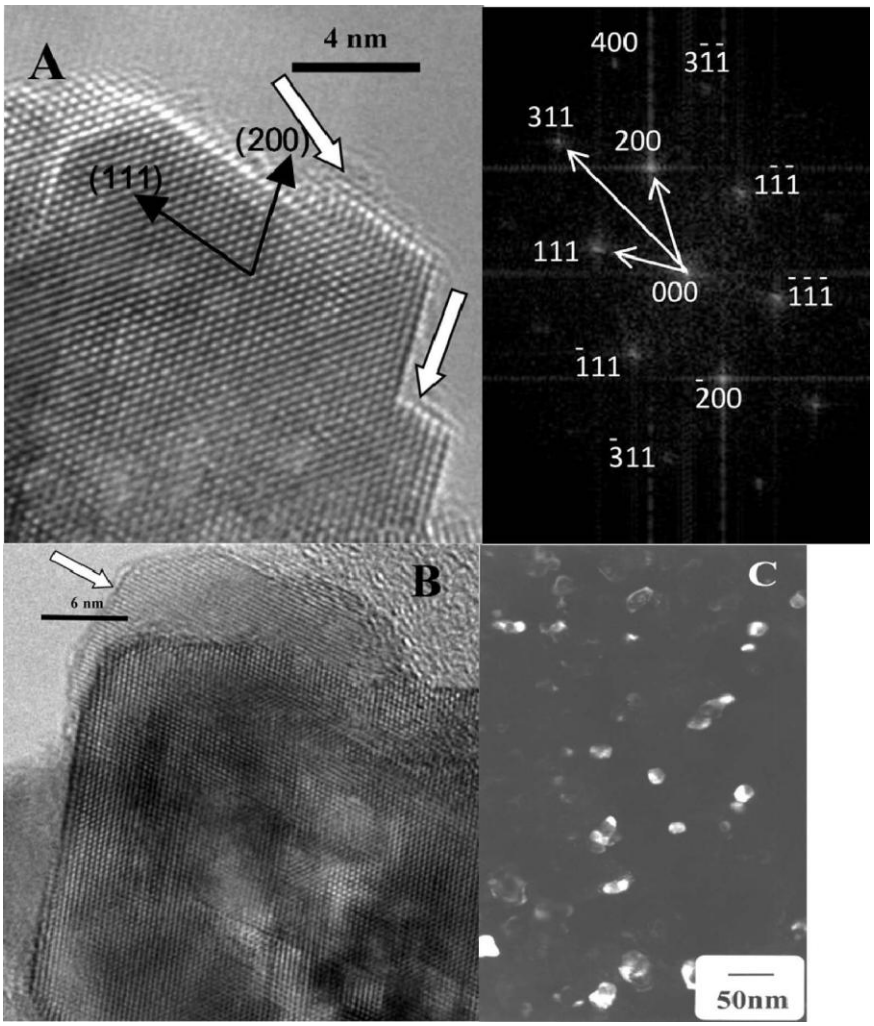


**Figure 6.4:** Typical transmission electron micrographs of $CeO_2$ nanocrystals synthesized from method 1.

**(A)** High-resolution TEM image (left) of the simple precipitated sample calcined at 350 °C and its corresponding Fourier transformation (right), with the zone axis along the [011] direction.

**(B)** High-resolution TEM image of the simple precipitated sample calcined at 650 °C.

**(C)** Dark-field image.

Together with the TPD/TGA evidence, it is suggested these are a thin layer of amorphous hydrous oxide at the surface. Similar data were observed from product from the microemulsion reaction route. On the basis of these data together with the

BET and XRD evidence, we would suggest that these reactions proceed to form well-ordered, small nanocrystals exhibiting the $CeO_2$ fluorite structure. The surface of these nanocrystals has significant amounts of water present as a hydroxide or related chemical species.

It might be thought that these very well structurally defined nanocrystals offer an ideal means of studying changes in structure and properties that might occur as the crystallite size is reduced. The $CeO_2$ system appears intrinsically simple as there seems little evidence for polymorphism and the nanocrystals have little porosity or dislocation chemistry to introduce significant amounts of strain. However, there has been little consistency in the XRD analysis of the products, particularly in terms of how the lattice parameter varies as a function of size at low dimensions. This is apparent, as illustrated by comparison of data for the simple precipitation reaction and the micelle mediated precipitation. Typical data from the micelle and precipitation reactions are shown in Figure 6.5. For the micelle templated reaction, there is a small expansion of the lattice parameter at small nanocrystal sizes (~0.15% of the value at larger crystallites). However, there is a significantly greater contraction (~0.32%) in the lattice parameter for the precipitated materials. The variation with crystallite size also differs: a small variation over a large range of sizes for the micelle template reaction, whereas a rapid variation of the lattice parameter over a much smaller crystallite size range is observed for the precipitated materials.

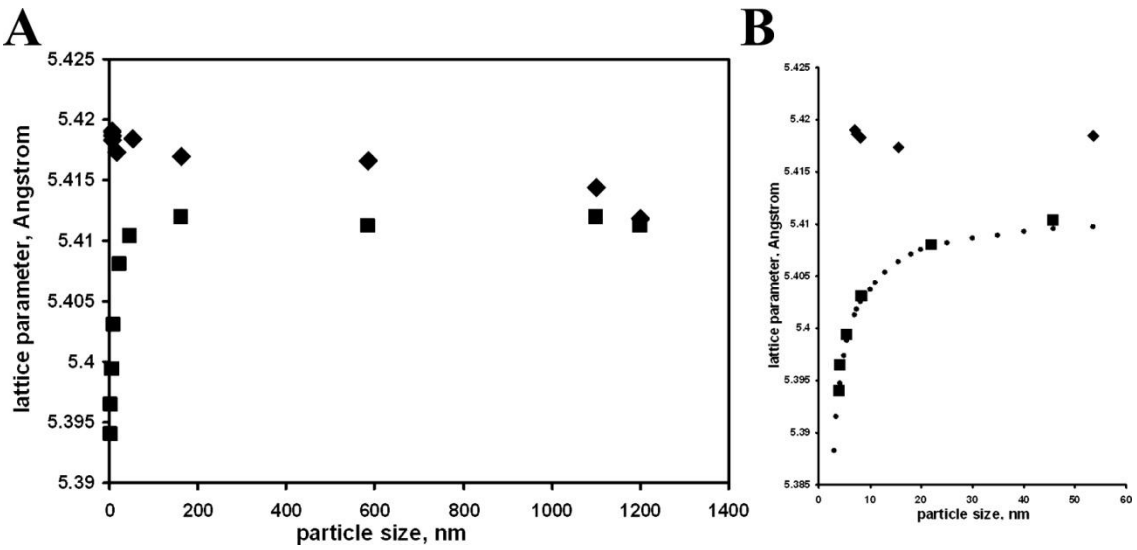


**Figure 6.5:** Plots show the variation in lattice parameter as a function of crystallite size for micelle templated (♦) and simple precipitated (■) samples. Panel **A** is the full range of data, and panel **B** is an expanded range around small crystallite sizes. The (•) points in B are calculated data from the surface area-to-volume ratio (see text).

The lattice expansion at small crystallite sizes is similar to other data reported in the literature, and the relatively small magnitude of expansion noted is broadly similar to results reported by various authors (0.1-0.5%). [226, 227, 228, 229, 230, 231] However, work by Tsunekawa *et al.* [221, 222, 223] and Wu *et al.* [232] shows a much more dramatic lattice expansion at small particle sizes (2.5-3.5%), and Hailston *et al.* [233] observes a lattice expansion of almost 7% in a 1 nm size. The lattice contraction at small crystallite sizes for the precipitated samples is a novel finding. These conflicting results of lattice expansion and contraction require careful consideration of cerium oxide solid-state chemistry. To understand the relationship between the lattice parameter and the presence of reduced ceria materials further, samples prepared via the LPDP method (method 3) were investigated as this provides a convenient method to produce materials with controllable 3+ valence. Figures 6.6 and 6.7 describe data summarizing studies of ceria nanocrystals formed by the LPDP method. Because the reaction is carried out in nonaqueous (and in the absence of air or $CO_2$) conditions and involves the direct reaction of the dissolved metal cation with

anions, the valence of the cation is maintained through the preparation. In this case where

$$2Ce_{(sol)}^{3+} + 3O_{(sol)}^{2-} \rightarrow Ce_2O_{3(s)}\downarrow \qquad \text{Eq. 6.1}$$

(sol) indicates solution, (s) indicates solid, and ↓ indicates the formation of a precipitate.

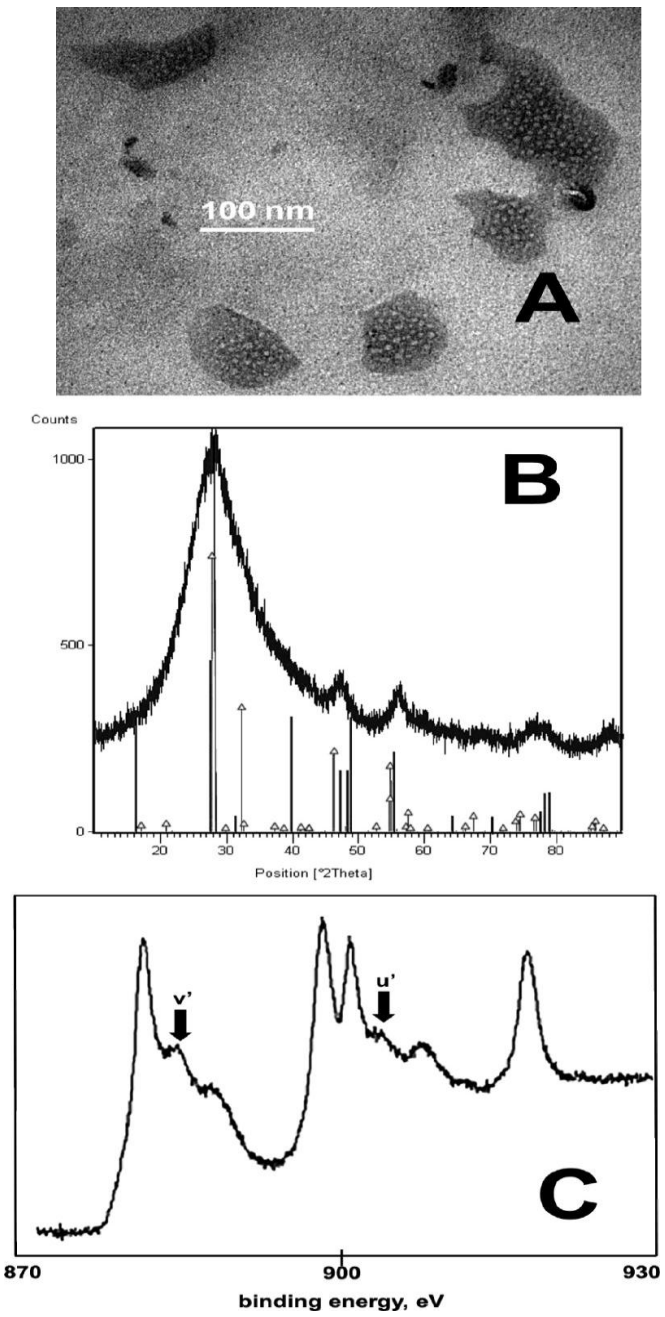


**Figure 6.6:** Characterization of ceria nanocrystals synthesized by the direct precipitation method. These were freshly synthesized and dried before rapid transfer to characterization equipment. **(A)** TEM micrographs. **(B)** XRD pattern. Lines marked with triangles are from JCPDS file 71-0567 $Ce_7O_{12}$ and unmarked lines from $Ce(OH)_3$ and JCPDS file set 19-0284. **(C)** XPS data.

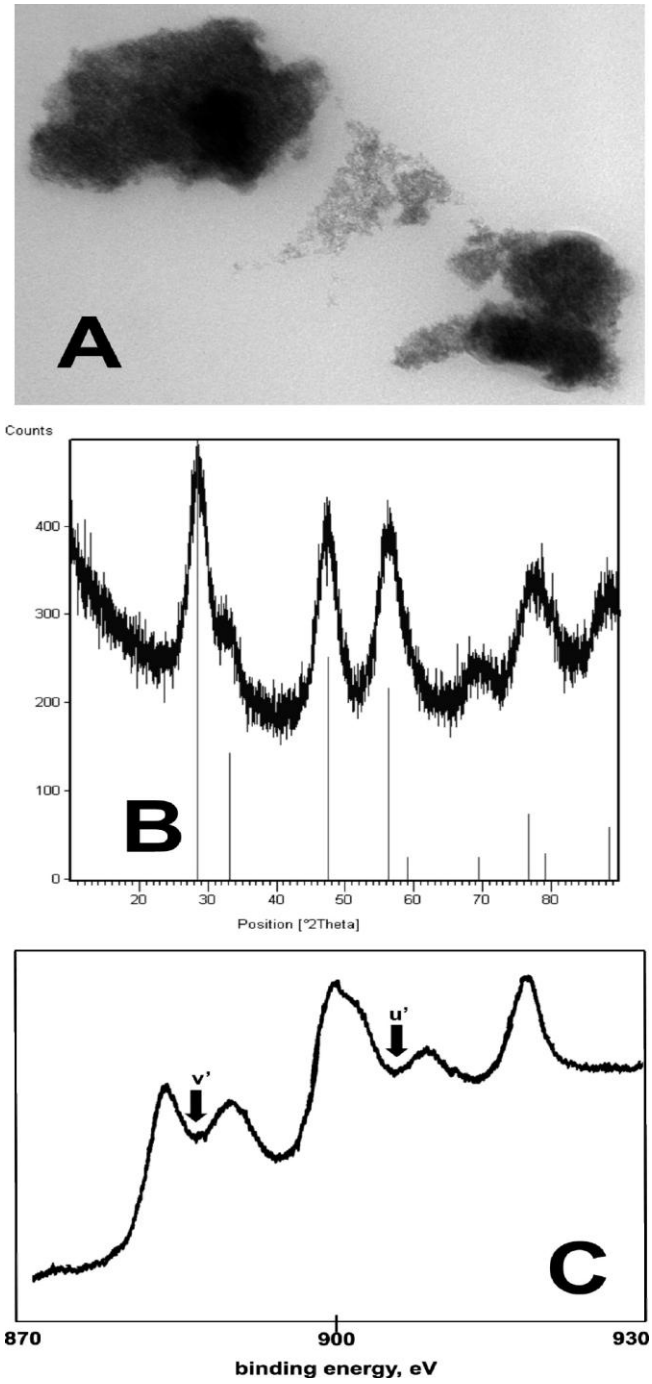


**Figure 6.7:** Characterization of $CeO_2$ nanocrystals synthesized by the direct precipitation method. These were as described in Figure 6.6 but exposed to ambient for a further 4 h prior to characterization. **(A)** TEM image of the nanocrystals (the scale bar is 100 nm), **(B)** XRD pattern, and **(C)** XPS data. See text for further details.

The product in solution is a violet precipitate and is stable in the solution (provided it is not exposed to air) for several days. This is quite different from the other synthesis strategies where the product is yellow-white (precipitation, method 1) or purple but turns yellow-white after a few minutes (micelle mediated, method 2). A violet precipitate is associated with formation of $Ce^{3+}$ products, as described below. If the product is collected, it has a quite different morphology compared with that described by the products of methods 1 and 2. The TEM is shown in Figure 6.6A. The product consists of small particulates (around 4-7 nm in size) within a larger volume (around 100 nm) of less dense amorphous material. XRD provides little information on the particles (Figure 6.66B). These data were collected as quickly as possible after harvesting the precipitate (within 1 h). The diffraction profile is unusual compared with the other materials prepared here, being dominated by a broad reflection around 28-29° 2$\theta$ with weaker reflections at higher angles. The peak widths (via the Scherrer formulizm) are in agreement with TEM, suggesting crystallite sizes of about 6 nm. Absolute assignment of these features to a known crystal structure is not possible. In Figure 6.6B, JCPDS data from $Ce_7O_{12}$ (JCPDS 71-0567) and $Ce(OH)_3$ (JCPDS 19-0284) are included, which provide a reasonable match to the data. Although significant amounts of $Ce(OH)_3$ are unlikely in this preparation, it may be formed by air exposure during characterization when samples are exposed to ambient. Strong hydroxyl peaks were observed by infrared spectroscopy, but this was true of all of the nanocrystals as the surface rapidly forms hydroxyls on exposure to ambient. However, it is clear that the XRD profile is not typical of the $CeO_2$ fluorite structure in terms of either the reflection position or the overall peak intensity envelope. As might be expected from the preparation, the data suggest the formation $Ce^{3+}$ -containing products. It should be noticed that, if the position of the large feature is taken as the usual $CeO_2$ (111) reflection around the same position, the data would indicate a rather large lattice expansion to around 0.551 nm. This is consistent with the lattice parameter of ceria doped with around 70 metal mol % lanthanum cations and suggests an equivalent amount of $Ce^{3+}$ would be present. [216] Further evidence for the reduced (i.e., $Ce^{3+}$/anion vacancy) nature of this material is provided by XPS studies

(Figure 6.6C). The Ce 3d spectra show the normal complex form due to shake-down satellites from an O 1s-to-Ce 4f electron transfer (see below), but two features marked u′ and v′ are present, which are taken to be evidence for the presence of anion defects and $Ce^{3+}$ [234, 235] The resolution of the data is comparable to metal samples and coupled to the fact that no binding energy correction was needed suggests that little sample charging is occurring, and this is consistent with vacancy/electron mobility expected for reduced $CeO_2$. [211]

If the material is analyzed after a further 4 h of exposure to ambient, extensive oxidation has taken place. The sample is now a homogeneous pale yellow color, and the TEM micrographs show the presence of small nanocrystals and aggregations thereof (Figure 6.7A). There is little sign of the ill-defined amorphous structure seen in Figure 6.6A. The XRD profile (Figure 6.6B) has evolved into that expected of the $CeO_2$ fluorite structure, and peak positions (giving a cubic lattice parameter) 0.54106 nm) and peak intensity ratios match precisely with expected values (JCPDS file 04-0593). The crystallite size has also increased to about 11 nm, which is similar to that seen in the TEM data (Figure 6.7A). This may be related to the thermodynamic driving force for producing $CeO_2$ crystallites (as above) and/or the thermal energy generated by the oxidation process. The XPS data also show considerable changes (Figure 6.7C), and its shape is typical of stoichiometric $CeO_2$. [234, 235] As shown, the contributions of the u′ and v′ features can no longer be detected. Further, the Ce 3d peaks have broadened and a sample charge correction of around 5 eV needed to be applied. This is consistent with an insulating sample and stoichiometric $CeO_2$. In this way, data show that, although $Ce^{3+}$ -type states can be produced during synthesis, it is unlikely that they are other than transitory in nature in ambient conditions. The results would suggest that forming stable defect-containing ceria surfaces is unlikely, despite reports to the contrary.

## 6.6 Discussion

The data presented in this paper show that observation of a $CeO_2$ lattice expansion is highly dependent on preparation and is difficult to rationalize in terms of a simple model and, further, that reduced ceria surfaces are not stable on ambient exposure. These are results that differ from literature reports, and it is worthwhile to explore these differences in depth. In the first instance, it is worthwhile to review the defect chemistry of ceria and assess whether or not the observations made are consistent with what is known about ceria bulk and surface chemistry.

The defect chemistry of ceria is well-known, and in Kroger-Vink notation, it is written as:

$$2Ce_{Ce}^{*} + 3O_{O}^{*} \leftrightarrow 2Ce'_{Ce} + V_{ö} + 1/2O_{2\,(g)} \qquad \text{Eq.6.2}$$

where $V_{ö}$ represents the anion vacancy and $Ce'_{Ce}$ the "reduced" $Ce^{3+}$ cation formed by interaction of $Ce^{4+}$ cations with the electrons at the anion vacancy to form small polaron states. Reduction of bulk ceria single crystals results in a series of ordered oxygen deficient phases with increasing lattice parameter (the $Ce^{3+}$ cation is considerably larger than $Ce^{4+)}$ as the oxygen content decreases. [217] Whether ceria can be completely reduced to a cubic sesquioxide structure is controversial, and a limiting stoichiometry of around $CeO_{1.66}$ is probably the lowest that can be achieved by chemical or thermal reduction. [236] This is an important point; ceria is not easily reduced, and many hours of high-temperature thermal treatment (~1000 °C) in chemically reducing atmospheres are required to affect significant bulk reduction. Theoretical measurements suggest that the defect formation energy in the bulk is around 4 eV, [237] and this is around the value measured by thermogravimetry. [238] Such high defect formation energies would suggest very low equilibrium defect contributions in ambient or moderate conditions.

However, reduction at the surface is somewhat easier than in the bulk, and theory suggests values of 2-3 eV for the defect formation energy depending on the crystal plane and defect concentration. [237, 239] Xiao *et al.* showed that heating in ultrahigh vacuum (UHV) at around 700 °C is apparently enough to reduce metal-supported thin $CeO_2$ layers to $Ce_2O_3$, although the role of the support and the stoichiometry of the film are not well-defined. [240] On single-crystal $CeO_2$(111) surfaces, the reduction of the surface in UHV is significant at the higher temperature of 900 °C. [240] It can be seen from these and other reported data that surface reduction still requires very significant thermal input even in non-oxidizing atmospheres. [219] Some authors have suggested unusually low defect formation energies at the surface of nanocrystals. Such behaviour may relate to the fact that nanocrystals may show a distribution of surface planes that differs considerable from that of larger crystallites, and it is accepted that the $CeO_2$(110) and (100) planes are significantly easier to reduce than the more thermodynamically stable $CeO_2$(111) plane. [237] It is clear from previous high-resolution microscopy studies of ceria nanocrystallites that the preparation method has profound effects on the ceria habit; nanocrystal morphologies exhibiting largely (111) facets are commonly reported. [226] Other authors have shown (100) facet dominated nanocrystals [241] and, still, more workers show mixed plane faceted crystallites. [242] Complex and amorphous surfaces have been suggested by various workers. [229, 232] An alternative explanation for anomalously low defect formation energies at nanocrystals might be higher concentrations of structurally defective sites compared with larger crystals. [243] These structural defects can include point defects, dislocations, steps, twins, and adsorbate sites. It would, thus, appear reasonable to assume that the increases in lattice parameters for nanocrystals compared with bulk stoichiometric $CeO_2$ can be associated with the presence of anion vacancies as many authors have indeed assumed. [221, 222, 223, 226, 229, 230, 232, 244]

However, despite this wealth of experimental data, few studies have considered

whether the presence of reasonable concentrations (i.e., measurable by relatively insensitive techniques, such as XRD or XPS) of anion vacancies on ceria nanocrystal surfaces in ambient atmospheres is credible. This is a necessary question because, in most reports, it can be concluded that ambient conditions are present during characterization or during transfer between synthetic reactors and analysis equipment. Oxidation thermodynamics of reduced ceria surfaces suggests anion vacancies should be below measurable concentrations in ambient atmospheres. Measured oxidation enthalpies for 3+ states are estimated at between 5 and 7.5 eV (depending on the extent of reduction), and the oxidation kinetics are also fast. [245] Careful measurements of the stoichiometry of nanocrystalline ceria suggest that anion vacancy concentrations are below physical quantification by techniques, such as powder X-ray diffraction, at room temperature in reasonable oxygen partial pressures. [246] It must also be remembered that the kinetics of reoxidation are fast. Various authors report data that oxidation of $Ce_2O_3$ films and powders occurs with high initial sticking probabilities. [234, 240] The fast kinetics of the oxidation of $Ce_2O_3$ are described in XPS data shown in Figure 6.8. Peak assignment is discussed below. Briefly, $Ce_2O_3$ (Figure 6.8, spectrum D) can be formed by $Ar^+$ bombardment of an oxidized cerium foil (thickness of the oxide film is around 500 nm) at room temperature and in ultrahigh vacuum. Small amounts of 4+ in the reduced film can be observed, but this is probably a result of trace oxygen during the argon ion reduction method used. This $Ce_2O_3$ film is completely converted to $CeO_2$, within the depth of analysis, by exposure to only 1300 L of oxygen at room temperature (Figure 6.8, spectrum E). Considering the very narrow radius of a ceria nanocrystal (i.e. in a 5 nm diameter nanoparticle, the bulk is only about five lattice units from the surface), any surface to bulk mass transport effects are probably negligible, and it is, therefore, highly unlikely that significant concentrations of anion vacancies will survive air exposure unless stabilizing anions or ligands are present.

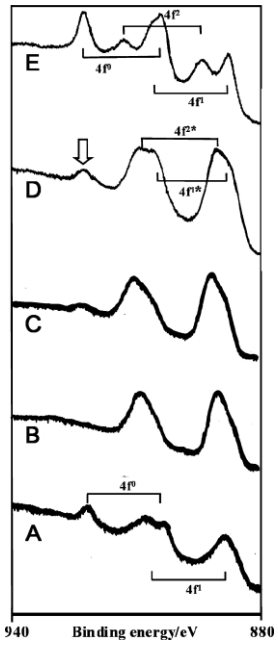


**Figure 6.8:** XPS data from cerium compounds: **(A)** Data from $Ce(SO_4)_2$ following vacuum dehydration, **(B)** data from $Ce_2(SO_4)_3$, and **(C)** the same material after exposure to X-rays in the vacuum chamber for 1 h. Spectra **D** and **E** are data from a cerium foil. Spectrum D represents a cerium foil following oxidation and argon ion reduction to produce $Ce^{3+}$ at the surface. **(E)** The same foil following oxidation by oxygen exposure as described in the text.

With such small changes in lattice parameters being measured, it is worthwhile to assess the validity of these measurements. An apparent increase of lattice parameters at low dimensions may not be definitive proof of the presence of vacancies, and an explanation based on high dislocation densities causing the lattice expansion may be more applicable in very low dimension nanocrystals. [247] Further, measurements of very small peak position shifts (here, 0.05 and 0.1° $2\theta$ are typical) in powder X-ray diffraction are fraught with difficulties and represent a challenge instrumentally. Reproducibility of the position and height of the samples is absolutely critical, and the apparatus must be almost ideally set up (sample height and goniometer position, etc.). Also, there is a sample limitation because of the small crystal sizes that give rise to

broad and low intensity reflections (e.g., Figure 6.1). It is clear therefore, that experimental accuracy is a concern and necessitated the use of an internal zirconia reference (described above) to measure shifts as accurately as possible in this work.

Because of these difficulties, complementary evidence for defect formation at nanocrystal ceria surfaces is often obtained from XPS studies. The first major problem with this and related spectroscopies is the sensitivity of $CeO_2$ to irradiation with X-rays, [248, 249] local heating, [250] electron interactions, [251] and ion bombardment, [252] which can bring about substantial reduction. [232, 234, 240] For example, Zhang *et al.* correctly point out that X-ray irradiation and quantification difficulties can lead to a significant overestimation of the $Ce^{3+}/Ce^{4+}$ ratio determined by XPS. [249] Further, considering the transfer of samples from synthesis to a vacuum chamber, the possibility of the characterized sample being different from the as-synthesized version is considerable. The previous analysis manner of the cerium XPS data in terms of the presence of $Ce^{3+}$ is somewhat overly facile. The XPS spectra of $CeO_2$ and $Ce_2O_3$ have been well understood [42] for many years, following the first detailed studies by Burroughs *et al.* [235] XPS observed Ce 3d (and other photoelectron features) have a complex series of shake-down satellites originating from an O 2p-to-Ce 4f electron transfer in the final state (nominal electron configurations $4f^0$, $4f^1$, and $4f^2$). [235] Because the data are so complex on high backgrounds and prone to changes during lengthy analysis, quantifiable interpretation in terms of simple "valence signatures" and actual stoichiometry is a serious challenge. Results are illustrated in Figure 6.8. A somewhat simplified assignment of features observed for $CeO_2$ following Iijima *et al.* [253] is shown in Figure 6.8, spectrum E. $Ce_2O_3$ (Figure 6.6D) also displays a more complex structure than can be expected resulting from a mixture of 4f1 and 4f2 states,25 and these are labelled as $4f^{1*}$ and $4f^{2*}$ states to differentiate them in the figure. The Ce2O3-derived $4f^{1*}$ state is very closely related in peak shape and position to the $CeO_2$-derived $4f^1$ state, although the $4f^{2*}$ and $4f^2$ states are quite different.

The assumption that the $Ce^{4+}/Ce^{3+}$ ratio and the corresponding anion vacancy in a sample can be extracted by curve-fitting Ce 3d XPS spectra calculated from that is fundamentally flawed for two reasons. First, this method titrates the number of $Ce^{3+}$ ions not the number of anion vacancies. For example, in Figure 6.8, the spectral envelope and peak positions for $Ar^{+}$ ion produced $Ce_2O_3$ and $Ce_2(SO_4)_3$ are very similar. Thus, $Ce^{3+}$ states might be produced by surface species originating in sample preparation or adventitious adsorption rather than the presence of any anion vacancy defect structure. It is also worth noting that $Ce_2(SO_4)_3$ can be oxidized in the analysis, as shown by the additional feature appearing in Figure 6.8, spectrum C. The second important factor to consider is whether, in this sort of complex system, XPS data from a $4^{+}$ (or a $3^{+}$) state is independent of the chemical environment, and the chemical environment at the surface is likely to be complex for chemically synthesized and/or air exposed samples. For cerium, the simple assignment of 3d peak shape and position to a $4^{+}$ or a $3^{+}$ valence is not possible. Illustrative data are seen in Figure 6.8, spectrum A, where the Ce 3d photoelectron spectra of $Ce(SO_4)_2$ is displayed. The spectrum has a profile typical of neither $CeO_2$ nor $Ce_2O_3$. The peak positions are very similar to those of the $4f^1$ and $4f^0$ states seen for $CeO_2$, but the expected $4f^2$ states are apparently absent. It is, therefore, clear that, because of structural or band changes (in cerium (IV) sulfate compared to $CeO_2$), transfer of O 2p electrons to form the $4f^2$ state is not possible. In this way, XPS spectral changes may not be due to changes in valence at all but may indicate a changing structural arrangement and/or electronic structure alteration.

On the basis of this evidence coupled to our understanding of the defect chemistry of cerium oxides, the simple association of lattice expansion with anion vacancy defect formation in much of the reported literature is not reliable. Further, there is little definitive evidence that nanocrystal surfaces can sustain thermodynamically or kinetically stable anion vacancy defect structures. Instead, we favor a model where, in general, the presence of other species at nanocrystal surfaces (as opposed to oxide anion nonstoichiometry) results in the apparent observation of lattice expansion and

$Ce^{3+}$ states. It should be emphasized that high-temperature preparation routes (such as that used by Wu *et al.* [232]) do probably produce nonstoichiometric cerium oxides, and with very careful experimental procedures, these may be transferred into vacuum chambers for analysis. Indeed, Wu *et al.* emphasize the nonequilibrium nature of the thermal evaporation method used. However, for chemical methods, differences in lattice parameter variation reported in the literature probably reflect preparation variables rather than any inherent properties associated with small dimensions.

The studies of Hirano and co-workers, [254] Chen and Chen, [255] Hirano and Inagaki, [256] and Djuricˇic´ and Pickering [257] help provide a framework for understanding chemical synthesis of ceria nanocrystals, but there is little quantitative evidence for the mechanism and the intermediate species proposed besides gravimetric measurements of poorly defined reaction products. A general reaction scheme (assuming a trivalent cerium precursor is added to a basic solution) can be described: [258]

$$Ce_{(sol)}^{3+} + 3OH_{(sol)}^{-} \rightarrow Ce(OH)_{3(s)}\downarrow \qquad \text{Eq. 6.3}$$

The exact nature of the precipitate (written here as $Ce(OH)_{3(s)}$) is unknown but is probably a complex oxy-hydroxide material containing species, such as CeOOH and $CeOOH(OH_2)$. The moieties are probably ill-defined and exist as largely small amorphous particulates that can be densified and crystallized to form the fluorite structure in oxidizing conditions. These solid precipitates can be oxidized in excess base or an oxidizing atmosphere: [255]

$$2Ce(OH)_{3(s)} + 1/2O_2 + H_2O \rightarrow 2Ce(OH)_{4(s)} \qquad \text{Eq. 6.4}$$

The oxidation is indicated by a change in color from purple to yellow.18,48 The Ce(OH)4 species is probably more accurately written as a series of species, such as $[Ce(OH)_x(H2O)_y]^{(4-x)+}$. [255] Although $Ce(OH)_4$ can be inferred from fundamental

chemistry, evidence for its presence is somewhat harder to obtain. Thermogravimetric evidence is suggestive, [258] but XRD is less conclusive. It is generally thought to have a largely amorphous structure, and two XRD reports [259, 260] detail a broad peak envelope from this material similar to that of the ceria fluorite structure but shifted to slightly lower angles and so an apparent increased lattice parameter compared with CeO2. These XRD results might be over interpreted, but combined with X-ray absorption studies [49] that show chemical and structural similarities of $Ce(OH)_4$ to $CeO_2$, they provide reliable evidence that $Ce(OH)_4$ can be essentially described as an hydroxylated amorphous form of ceria, $CeO_2 \cdot 2H_2O$, and that dehydration and crystallization result in crystalline $CeO_2$ formation. It might be argued that the presence of this phase may lead to the observation of apparent lattice expansion in some of the previous studies. It might also be reasonably argued that the formation of a $CeO_2 \cdot 2H_2O$ phase as a direct precursor to the fluorite phase is the reason why very well ordered crystalline phases of very small ceria particles are so frequently observed (as here in Figure 6.4). On this basis, it might be concluded that very well defined stoichiometric crystallites of cerium dioxide can be formed in high pH conditions (as in our simple precipitation method). The amorphous or disordered surface layer seen in the work and elsewhere [229] described here is an outer layer of $CeO_2 \cdot 2H_2O$ that is stable initially at the liquid-solid interface and then at the air-solid interface. Alternatively, in low pH conditions (as in the micelle method used herein), the product would be a $Ce^{3+}$ -type material and formation of a highly crystalline product is less likely and would only occur on heating/exposure to oxygen. This was noted in the purple-yellow color change seen on stirring. It might also be concluded that the products formed would be sensitive to the pH (or $OH^-$ concentration in method 1).

Experimental support for these suggestions has been found. Data are shown in Figure 6.9 where the measured lattice parameter is plotted against nanocrystal size for a series of solutions of differing $[OH^-]:[Ce^{3+}]$ ratios (prepared as defined in method 1, but controlling the amount of $NH_4OH$ used). In all measurements, the nanocrystals

show a significant lattice contraction at small sizes. It is suggested that lattice contractions may not have been observed in earlier studies simply because it is more usual to use bulk $CeO_2$ crystallite as a baseline to evaluate the lattice parameter change where the surface status (defect and vacancy concentration) of bulk materials is different with those prepared by the different methods.

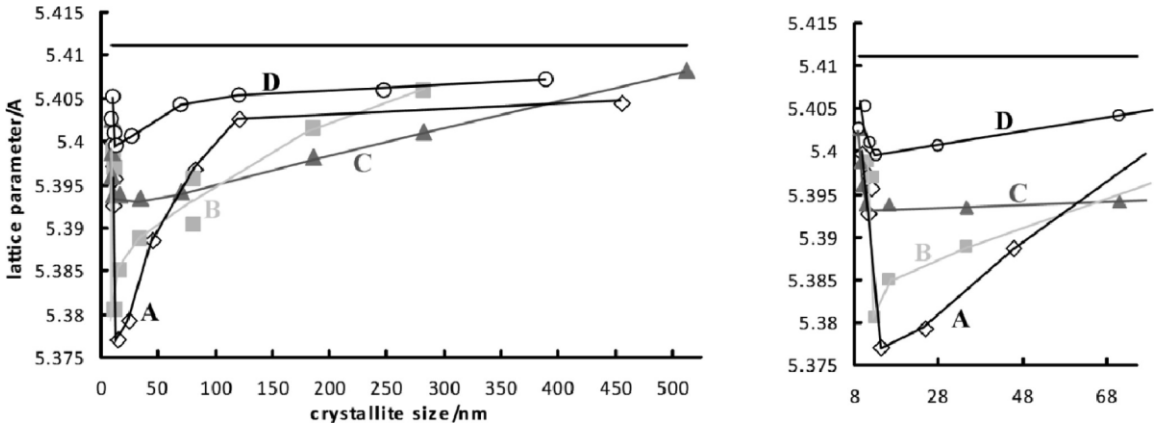


**Figure 6.9:** Lattice parameter of ceria nanocrystals versus crystallite size as a function of the initial ratio of molar concentrations of hydroxyl and cerium ions. Plots A-D represent $[OH^-]/[Ce^{3+/4+}]$ concentration ratios of 6:1, 3:1, 1:1, and 1:3, respectively. An expansion of the data for low crystallite sizes is shown on the right. The solid lines indicate the bulk lattice parameter

Therefore, for a given-sized ceria crystallite, the lattice parameter may show either expansion or contraction compared with the bulk one. Systematic investigation of ceria crystallites with different sizes in a broad range under comparable conditions is necessary. A series of experiments shown in Figure 6.9 crosses a size range from 2 to 500 nm under the same synthesis conditions. In the data shown in Figure 6.9, distinct minima in the lattice parameter can be seen at a nanocrystal size of about 15 nm when the crystallite changes from either end of the size range. We can conclude that the lattice undergoes contraction with the decrease of crystallite size from 500 to 15 nm,

whereas it expands following the same trend when the crystallite size decreases down from 15 nm. The value of this minimum lattice parameter decreases with increasing hydroxyl concentration. We suggest that the minima in the curves are caused by two opposing effects overlapping -an apparent lattice expansion caused by the presence of either $Ce^{3+}$ -containing species (from the preparation) or other defect-related strains and a lattice contraction caused by the additional pressure derived of surface tension between the crystallite and its ambient atmosphere. The additional intensity distribution of pressure over the volume of a sphere-shaped particle is a linear function of its radius curvature, $1/r$, and is proportional to its surface area-to-volume ratio ($S/V$). Therefore, the additional intensity of pressure for a smaller crystallite is significantly higher than a large one, and the lattice contracts dramatically when the crystallite size decreases from ~$10^3$ to ~$10^1$ nm. Indeed, the lattice contraction for the simple precipitated samples perfectly matches the surface area-to-volume ratio curve, as shown in Figure 6.5B. The lattice contraction can be relaxed when the materials are analyzed under vacuum. Therefore, it should not be a surprise if the lattice expansion analyzed under high vacuum conditions, for example, by TEM/SAD, is significantly larger than those analyzed under ambient conditions, for example, by XRD. Some interesting results obtained from previous papers on the lattice expansion supports the conclusion. Hailstone *et al.* [221, 222, 223, 232, 233] have observed a 2.5-7% lattice expansion by TEM, whereas Zhang *et al.* [226, 227, 229, 231, 261] have obtained a 0.24-0.45% lattice expansion by XRD. The lattice expansion under the vacuum is 10 times higher than that in the ambient conditions. Defects or anion vacancies are most likely formed on the surface of a ceria crystallite where the vacancies produced on the surface diffuse continuously into the crystallite at a very slow rate at low temperatures, especially for large ceria crystals, for example, bulk materials. The diffusion rate of the anion vacancies along the radial direction accelerates dramatically when the ambient temperature is elevated or the crystal size is reduced to a great extent. For a given crystallite, the vacancy concentration inside the crystallite will reach to an equilibrium state after a period, where the period depends on the crystallite size and the bigger the size, the longer the period is. For a smaller ceria

nanocrystal, the surface vacancies diffuse inside the crystal faster and more $Ce^{4+}$ ions are reduced to $Ce^{3+}$ ones in a detectable region, and therefore, the observed lattice is bigger. $OH^-$ or $H_2O$, like other stabilizing agents, is easy to be absorbed on the anion vacancy sites on the surface of a ceria crystallite, where a similar phenomenon was observed by Xu *et al.*, [261] and they attributed it to the formation of surface superoxide-like species. The effectual vacancy concentration on a crystallite surface decreases with the increase of the absorbed $OH^-$, and the higher the $OH^-$ concentration, the lower the vacancy concentration on either the surface or inside the crystallite and the smaller the lattice expansion is. At the lowest $[OH^-]$:$[Ce^{3+}]$ ratios, more anion vacancies (more $Ce^{3+}$ species) are preserved and the observed lattice contraction is smallest due to the expansion effect offsetting the contraction one to a great extent, as seen in Figure 6.9 (plot D). At the highest $[OH^-]$: $[Ce^{3+}]$ ratios, $Ce^{3+}$ species have a much smaller concentration and lattice contraction is maximized as the expansion effect is minimized, as seen in Figure 6.9 (plot A). It seems that a high concentration of surface $OH^-$ ($H_2O$) eases the lattice expansion. The origin of these lattice contractions agrees with theoretical calculations using density functional theory [262] and molecular dynamics simulations, [263] which predict small lattice contractions for $CeO_2$ (111) surfaces due to reduced bonding potentials at the surface. Similar lattice contractions/expansions have been seen for other systems. [264, 265] The lattice contraction observed in this work is around 0.5%, and this is consistent with these estimates and previous observations by XRD. Our experimental data closely follow models where the lattice deformation in oxide systems can be written as: [264]

$$\Delta L = (\Delta C)_s + (\Delta E)_d \qquad \text{Eq. 6.5}$$

where $\Delta L$ is the deviation value of lattice parameter ($L$) from the equilibrium state. $(\Delta C)_s$ is the contraction ($C$) value from the equilibrium state induced by the surface tension between a nanocrystal and the surrounding atmosphere, and $(\Delta C)_s$ is proportional to ($r^{-1}$) (where $r$ is the radius of a nanocrystal); $(\Delta E)_d$ is the expansion

determined by the cation ($Ce^{3+}/Ce^{4+}$) ratio due to the nonstoichiometry of the material or other chemistries, as described above. Figure 6.10 illustrates these effects schematically. It is expected that, as the size of a nanocrystal decreases, lattice contraction caused by surface tension increases, as seen in other metal nanocrystal systems. [264] However, at very small nanocrystal sizes, the ratio of surface to bulk atoms increases markedly and the contribution of surface $Ce^{3+}$ or anion defect sites becomes increasingly important and an overall lattice expansion is observed.

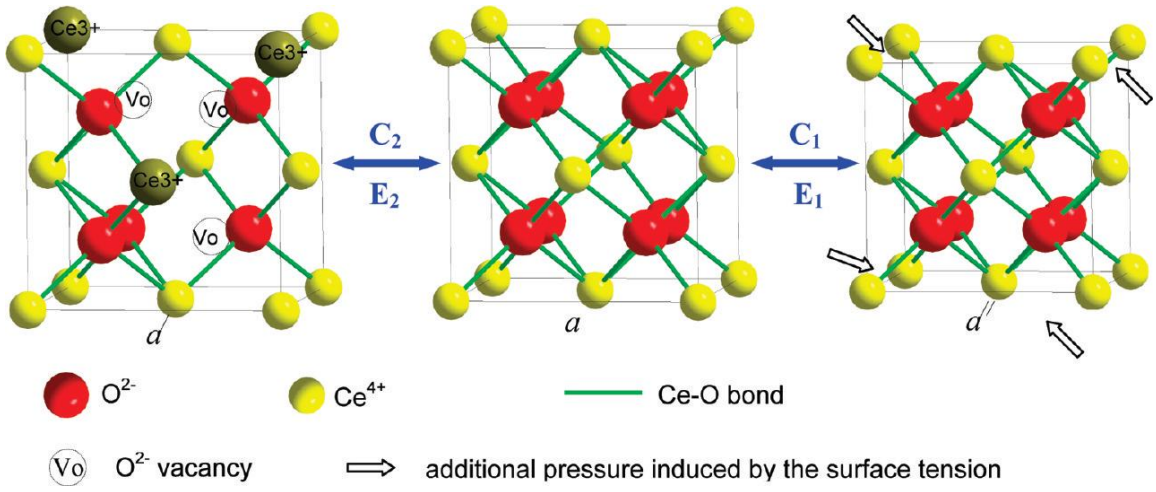


**Figure 6.10:** Schematic representation of a reversible lattice deformation in a cubic CeO2 unit cell. "C" denotes lattice contraction, whereas "E" indicates lattice expansion. The subscript number "1" indicates that the deformation (contraction or expansion) of the lattice is caused by the additional surface tension in an air-solid system, and "2" implies that the deformation is derived from nonstoichiometry (as illustrated) or other surface chemistries caused by the anion (vacancies) defects in the cell. The lattice parameter decreases in the order $a' > a > a''$.

## 6.7 Conclusions

The work presented here and careful consideration of the data provided, suggest the following:

1. The lattice change of ceria NCs is closely related to the crystallite size, the vacancy defect concentration in a detectable region, and the analysis conditions (under vacuum or ambient atmosphere), where the vacancy concentration has a linear relationship with the lattice change; that is to say, more vacancies result in lattice expansion, whereas the crystallite size has a more complex effect on the lattice change.

2. The vacancy concentration in a ceria NC is controlled by two factors: one is the surface status (with or without a surface stabilizing agent), and another is the vacancy diffusion rate. The vacancies can be refilled by the surface absorbance of the stabilizing agent, for example, $OH^-$ or $H_2O$, on the vacancy sites or diffused inside the crystallite by the vacancy thermal movement.

3. The lattice expansion of a ceria NC can be offset by its lattice contraction due to the additional pressure caused by the surface tension between the crystallite and the ambient atmosphere. The smaller the crystallite size, the more intense the incurred additional pressure and the larger the resulting lattice contraction is.

4. Both the expansion and the contraction effects are positively correlated functions of $1/r$ and increase with the decrease of the crystallite radius, $r$. The contraction effect surpasses the expansion one when the crystallite size reduces from the bulk level to 15 nm, whereas a reverse trend is observed

when the size decreases down from 15 to 2 nm. Therefore, a minimized lattice contraction point at 15 nm is, for the first time, observed in ceria nanocrystalline materials.

5. The analysis conditions also have a significant influence on the observed lattice change. The relative lattice expansion obtained under vacuum, for example, by electron diffraction (TEM), is ~10 times larger than that obtained by ambient analysis, for example, by XRD.

This work also generally shows how difficult it is to characterize nanocrystals without a comprehensive understanding of the synthesis chemistry and the changes this can cause in the composition and structure of the nanocrystals. Even in the case of ceria, which exists in only one polymorph and has a strong tendency to produce highly crystalline materials, providing a definitive understanding of the system requires very careful characterization and study.

# 7 Chapter 7 - Outlook and Conclusion

## 7.1 Summary of Lattice Constant Dependence on Particle Size for Ceria prepared from an acid precipitation-peptisation gel.

The reason for lattice contraction observed is considered at small particles sizes for citric acid produced samples. Results obtained from PXRD analysis suggest that at higher temperatures, defects are being produced which result in lattice expansion as might be expected for small particles. However, below a critical size, lattice contraction maybe observed. These results strongly indicate that surface tension plays a major role in determining the lattice parameter. This is further supported by the decrease in particle size as temperature decreases as measured by TEM and HREM presented herein. The data suggests that anion vacancy defects are not created to any major extent in this work at these small particles. It is difficult to rationalise a reason for the differences in behaviour of citric acid compared to the mineral acids. It may simply be related to the size of the particles produced i.e. citric < oxalic < nitric and this small particle size allows more efficient oxidation in air thereby forming $4^+$ rather than $3^+$ Ce ions. This investigation of lattice parameter changes versus particle size, coupled to very careful synthesis methods, provides a deeper understanding of cerium oxide particle nanoscience.

## 7.2 Summary of Comparison of the preparation of nanocrystalline cerium oxide nanoparticles by forward and reverse precipitation

Forward and reverse precipitation gives markedly different products. Pourbaix diagrams show that $Ce^{3+}$ is stable in solution at normal pH values and that a minimum pH value of 4-6 must be reached before formation of $Ce(OH)_3$ occurs [266].

However, the $Ce(OH)_3$ formed has some solubility to a pH of about 10 when precipitation of the hydroxide is rapid. As the pH is raised further, the formation of $Ce^{4+}$ ($Ce(OH)_4$ or $CeO_2.2H_2O$) products becomes more likely, consistent with the reaction model given above in Eq. 1 – Eq.5. It thus seems that the reverse precipitation, where the pH through the process is uniformly high, is likely to give a $CeO_2$ type product whilst the forward precipitation process is more likely to give $Ce^{3+}$ precipitates particularly during the early stages of the process where the pH changes from acidic through to alkaline. This suggestion is apparently borne out by both the colour changes observed during synthesis and the lattice dimensions measured by XRD as well as previous XPS measurements [140].

What is also important is that the products of the precipitation are smaller and have lower size dispersions. This is also partly explained by the Pourbaix diagrams as the entire precipitation process occurs at a pH value where solubility is limited and thus nucleation, re-solution and the size related thermodynamic stability [267] of the particles has a much lesser effect and the statistical nature of the particle growth process is limited. Zhou *et al.* offer a detailed rationale for the size homogeneity of the product [149]. These authors point out that the solutions with high pH are highly supersaturated and this provides conditions for homogeneous nucleation. It should also be noted that growth of large particles is reliant on two processes; the normal Ostwald Ripening and also orientated attachment [157]. Orientated attachment is enhanced by surface hydroxyl groups ($Ce(OH)_3$) and so will tend to form larger particles. It is also interesting to note that the orientated attachment mechanism promotes formation of cubic [157] and linear [141] crystallite morphologies. It can, therefore, be reasonably asserted that this is the cause of the cubic and platelet structures seen for the forward precipitation route (Figure 4.7) and supports the higher $Ce(OH)_3$ content suggested by experimental evidence presented here for this preparation route. It might be thought that the oriented attachment is limited for $CeO_2$ type products because of the lower surface hydroxyl densities and thus the truncated octahedral shape is maintained.

From this work, it is suggested that reverse precipitation, which is often ignored as a

synthesis method, can provide a useful methodology to produce small particles producing a more size homogenous product and smaller particle sizes/higher surface areas. However, the products can have markedly different crystallite shapes and surface chemistries. They are likely to be more 'passive' to particle-particle attachment and also contain lower defect densities as they consist of single crystallites following homogeneous precipitation.

## 7.3 Summary of the Structure and Defect Chemistry of Ceria-Terbia Solid Solutions

The effect of terbia doping of ceria on the chemical reactivity is somewhat different than that reported for lanthana and other lanthanide $Ce^{3+}$ ions [195, 268]. No enhanced ceria reduction was observed here and this is consistent with the work of Martínez-Arias *et al.* [184], Guo *et al.* [185] and Wang *et al.* [194]. The almost passive nature of terbia in this regard is partly explained by the fact that only about ¼ of the terbium cations are in the lower valence state. Even at the highest loadings used we saw no evidence for bulk uptake of adsorbed species. Further, we saw no XPS evidence for formation of significant $Ce^{3+}$ formation (from either anion vacancy formation or compound formation) even when the ceria is the minor component of the solid solution. It should also be said that vacancies are in some way associated with terbium ions and the ion is largely in the reduced form. The terbium cation is predominantly $Tb^{4+}$ and the ratio of the two valence states (3:1) is not very different from that measured in terbia only samples. Whilst the passive effect of terbia addition probably requires detailed study, it can be tentatively suggested that this could be due to preparation rather than complex co-operative effects. It is well known that basic conditions favour Ce4+ formation over $Ce^{3+}$ and the higher basicity of $Tb^{3+}$ in the synthesis favours the higher oxidation state because of the well-known decrease in ionic radius with atomic number for this series of elements.

The amount present as $Tb^{3+}$ is significantly more than seen by other authors including Martínez-Arias *et al.* [184], Guo *et al.* [185] and Wang *et al.* [194]. Wang *et al.* [194] have also claimed that there is a variation in the relative amount of the oxidation terbium states with composition whereas this work suggests it is invariant. However, their conclusion was based on a limited number of samples and analysis of $L_{III}$ edge XANES spectra whose form, variation and dependence on structure complex. Chatzichristodoulou *et al.* [193] also suggest a variation in behaviour with composition with the relative concentration of $Tb^{4+}$ increasing with concentration. However, since the major evidence for the terbium ion oxidation state is measurement of the lattice parameter, it is suggested that the differences in the literature (on the variation and the magnitude of changes) probably arise from crystallite size effects. The crystallite sizes are strongly dependent on temperature and composition and, as reported herein, the lattice parameter is very dependent on crystallite size.

Finally, the decrease of lattice parameter as crystallite size is reduced should be carefully addressed. Definitive assignment of either lattice expansion or contraction has proved difficult [175]. It is suggested that this is due to three main reasons [175]. The ratio of $Ce^{4+}$ to $Ce^{3+}$ (anion vacancies and or trivalent compounds) in small crystallites is highly dependent of synthesis conditions as well as their thermal treatment and ambient exposure. Thus, the lattice parameter measured is sensitive to pre-treatment and history. The stability of these samples where significant surface or bulk $Ce^{3+}$ species were never observed should allow more complete analysis of the variation in lattice dimensions with crystallite size. It is shown here that there is a clear lattice contraction at small dimension consistent with surface tension effects. This is a significant result and suggests that, in general, this lattice contraction should be expected in the absence of other effects. Authors have suggested that lattice expansion at small crystallite dimensions suggests that $Ce^{3+}$ is the more stable state at the surface of small crystallites and nanoparticles. This work suggests this is not a general explanation and if vacancies do exist they are formed and maintained only in carefully controlled environments.

## 7.4 Summary of Size-Related Lattice Parameter Changes and Surface Defects in Ceria Nanocrystals

The work presented here and careful consideration of the data provided, suggest the following:

1. The lattice change of ceria NCs is closely related to the crystallite size, the vacancy defect concentration in a detectable region, and the analysis conditions (under vacuum or ambient atmosphere), where the vacancy concentration has a linear relationship with the lattice change; that is to say, more vacancies result in lattice expansion, whereas the crystallite size has a more complex effect on the lattice change.

2. The vacancy concentration in a ceria NC is controlled by two factors: one is the surface status (with or without a surface stabilizing agent), and another is the vacancy diffusion rate. The vacancies can be refilled by the surface absorbance of the stabilizing agent, for example, $OH^-$ or $H_2O$, on the vacancy sites or diffused inside the crystallite by the vacancy thermal movement.

3. The lattice expansion of a ceria NC can be offset by its lattice contraction due to the additional pressure caused by the surface tension between the crystallite and the ambient atmosphere. The smaller the crystallite size, the more intense the incurred additional pressure and the larger the resulting lattice contraction is.

4. Both the expansion and the contraction effects are positively correlated functions of $1/r$ and increase with the decrease of the crystallite radius, $r$. The

contraction effect surpasses the expansion one when the crystallite size reduces from the bulk level to 15 nm, whereas a reverse trend is observed when the size decreases down from 15 to 2 nm. Therefore, a minimized lattice contraction point at 15 nm is, for the first time, observed in ceria nanocrystalline materials.

5. The analysis conditions also have a significant influence on the observed lattice change. The relative lattice expansion obtained under vacuum, for example, by electron diffraction (TEM), is ~10 times larger than that obtained by ambient analysis, for example, by XRD.

This work also generally shows how difficult it is to characterize nanocrystals without a comprehensive understanding of the synthesis chemistry and the changes this can cause in the composition and structure of the nanocrystals. Even in the case of ceria, which exists in only one polymorph and has a strong tendency to produce highly crystalline materials, providing a definitive understanding of the system requires very careful characterization and study.

## 7.5 Closing Remarks and Future Outlook

This work has reported a detailed investigation of ceria nanoparticles in both doped and undoped form. The work has largely centred on understanding how the defect chemistry of these systems changes at small dimensions. The work has emphasised that proper characterisation of these materials is a challenge. Part of the problem in delivering a proper understanding is due to changes that might occur during analysis (XPS), the inability of the technique to provide definitive information (i.e. structural analysis using XRD) and an inability to produce 'standard' materials (i.e. uniformly sized particles of controlled bulk and surface composition). These characterisation challenges have caused confusion in the literature and it is clear that further study and

technique development is required to provide definitive understanding.

However for cerium oxide, despite the limitations described above, it is generally accepted that there is a change in many fundamental material properties below a critical dimension size (of the order of a few nanometre); this change is beyond that expected from the expected increase in the ratio of surface to bulk atoms as particle size decreases. Ceria, like many other inorganic materials displays a number of other effects in addition to these simple volume related effects. These changes include:-

a) The presence of surface strains and energies existing at the exterior and internal interfaces.

b) Quantum confinement effects arising from the presence of atom-like electronic states resulting from the solid boundary conditions being of the same order as electronic wavelengths. This can for example, increase the number of defects that exist at the surface.

c) Another electronic effect in ionic crystals arising from an absence of long range effects in the Madelung field. Again this may affect defect densities.

Many materials applications are entering dimension regimes described by the terms nanotechnology or nanoscience. This is well known in electronics particularly concerning the continued miniaturisation of silicon transistors. Catalysis has long been concerned with changes in chemical activity with particle size the most striking example shown by gold catalysts. It is becoming more obvious that size effects are important in oxide systems as well as elemental systems and authors such as Coey have demonstrated highly unusual magnetic effects in small dielectric oxides. It is less clear in these oxide systems that property changes are related to true dimensional effects and electron confinement. This lack of clarity is based on less well-developed theoretical models (compared to elemental systems), difficulties in preparing representative samples and also the development of suitable characterisation methods (e.g. large size single crystals are generally not available for

band state mapping). Thus, in order to produce a fundamental understanding of oxide nanoparticles it is necessary to design coherent research programmes and there has been a paucity of such work. As such there is an opportunity to generate important publications in respected journals.

Besides the requirement for detailed scientific study, there is also a commercial reason for carrying out this work. It might be expected that detailed fundamental knowledge would assist in the industrial processing of oxide nanoparticles and their applications. This is particularly true for the relationship of preparation to physical property which underlines this project. It should be emphasized that oxide nano-materials are commercially very important and leading the so-called nano-revolution. There is considerable scope for developing commercial applications within Ireland and companies that already use these materials. It is also true that oxide materials are likely to have a growing and significant interest to the Irish electronics industry.

In general, oxide nanoparticles are finding applications in the following areas:-

a) Ceramics with advanced mechanical properties such as superplastically formed zirconia which has advantages in terms of transparency and hardness as well as processability because of the nanodimensioned nature of the powder precursor.

b) Pigments and colorants and of relevance here is the use of titania and ceria as UVA/B filters.

c) Biomedical applications such as biocompatible coatings, tissue scaffolds and membranes.

d) Electronic and magnetic applications including high dielectric constant gate materials, resistors, piezoelectrics, LEDs, optoelectronics and sensor materials.

CeO2 is an important material in areas such as dielectrics, solid electrolytes, electrochromic materials, gas sensors and capacitor/battery devices.

However, their use will be limited in these areas due to the following:

a) Preparation of uniform sizes – scale up of lab methods and cost of manufacture

To fully realise the economic benefits of nanomaterials, a robust understanding of the fundamental scientific principles operating at the nanoscale level is required. Such an understanding will unlock the ability to synthesie and scale-up production of nanomaterials and allow producers to focus on designing with application in mind. Currently, production of nanoparticles generally falls into three categories: solid phase particles size reduction, liquid phase synthesis and gas phase synthesis. The main barriers for the success of nanoparticles production can be considered the high price and certain technical barriers. Each process suffers from limitations ranging from poor property control to introduction of outside contaminants into the product. Lack of appropriate equipment and environmental problems are also a barrier in limited cases. For example, the transistor is a basic building block for microelectronic devices, however, it is not clear what the (three-terminal) element of a nanoelectronic device will be. Likewise, a well-defined architecture required to process data has yet to be established.

b) Health and safety of nanoparticle manufacture

Of all the areas of nanotechnology, nanoparticles have generated by far the greatest concerns. The 2004 Royal Society report on ethical, health, safety and social issue (www.nanotec.org.uk) recommended that nnoparticulate forms of well-known materials be treated as a new chemical because of the novel ways that can interact with biological systems (for instance their ability to enter cells) and uncertainty about persistence in the environment. Much research remains to be done in understanding these interactions. According to authors, concerns and uncertainties raised, related to health and safety aspects, result in a slower adoption of nanomaterials by the industry. Thus, " *Companies need to understand and clarify the current trends in both toxicology and regulation in order to ensure that they can reap the rewards of nanotechnology while avoiding the risks, and*

*this needs o be done immediately*."

c) Costs of lanthanide materials and availability

New demand has recently strained supply, and there is growing concern that the world may soon face a shortage of the rare earths. In several years from 2009, worldwide demand for rare earth elements is expected to exceed supply by 40,000 tonnes annually unless major new sources are developed. These concerns have intensified due to the actions of China, the predominant supplier. Specifically, China has announced regulations on exports and a crackdown on smuggling. As a result of the increased demand and tightening restrictions on exports of the metals from China, some countries are stockpiling rare earth resources.

Despite the disadvantages described here, ceria and the other lanthanides offer considerable property advantages. The challenge is translating laboratory synthesis methods to the industrial scale. The preparations used must be reliable, reproducible and have minimal environmental impact. Solvent and energy recovery are required. The technique described here for reverse precipitation warrants study and efforts to scale up. It promises advantage in terms of size and potentially may be scaled for rapid production but this is likely to be a continual process whereas lab studies are done as batch. It will require significant chemical engineering to develop on the industrial scale but might enable new products and applications for commercial exploitation.

# 8 References.


[1] Trovarelli A, de Leiterburg C., Boaro M. and Dolcetti G., 1 *Catal. Today* 50

[2] Waller D., Lane J. A., Kilner J. A. and Steele B. C. H., *Solid State Ion*. 86 (1996) 767 and references therein

[3] Stefanik T. S. and Tuller H. L., *J. Eur. Ceram.* Soc. 21 (1967)

[4] Tsoga A., Gupta A., Naoumidis A. and Nikolopoulos P., *Acta. Mater*. 48 (2000) 4709

[5] Morris B. C., Flavell W. R., Mackrodt W.C., Morris M.A., *J. Mat. Chem*., 3 (1993) 1007

[6] Kümmerle E. A. and Heger G., *J. Sol. State Chem*., 147 (1999) 485

[7] O'Neill W.M. and Morris M.A., *Chemical Physics Letters*, 305 (1999) 389

[8] Esch F., Fabris S., Zhou L., Montini T., Africh C., Fornasiero P., Comelli G. and Posei R., Science, 309 (2005) 752

[9] Namia Y., Fukai K.I. and Iwasawa Y., *Catal. Today*, 85 (2003) 79

[10] Fornasiero P., di Monte R., Rao G. R., Kaspan J., Meriani S., Trovarelli A., Grazizni M., *J. Catal.* 151 (1995) 168

[11] Mays C. W., Vermaak J. S., Kuhlmann-Wilsdorf D., *Surf. Sci.* 12 (1968) 134

[12] Tsunekawa S., Sahara R., Kawazoe Y., Ishikawa K., 1999, *Appl. Surf. Sci*. 152 (1999) 53; Tsunekawa S., Ishikawa K., Li Z. Q., Kawazoe Y., Kasuya Y., *Phys. Rev. Lett*. 85 (2000) 3440

[13] Purkayastha P., Nanotechnology: The Genie is Out of The Bottle, www.delhiscienceforum.com (August 2003)

[14] ETC Group, Occasional Paper Series, 7 (1) (2003)

[15] Suryanarayana C., *Nanocrystalline Materials*. International Materials Reviews, 40(2) (1995) 41-64

[16] Law, M., Goldberger J. and Yang, P.D., *Semiconductor nanowires and nanotubes*. Annual Review of Materials Research, 34 (2004) 83-122

[17] Tiny Materials, Enormous Innovation, www.nanoscale.com (2003)

[18] Morgan N. , Nano Particle Dynamics

[19] Li P., Chen I-W, Penner-Hahn J. E., and Tien T. Y., *J. Am. Ceram. Soc*., 74 (5) (1991) 958-67

[20] Trovarelli A., *Catal. Rev. Sci. Eng* 38 (1996) 439-520

[21] Ricken M. , Nolting J., and Reiss I., *J. Solid State Chem*., 54 (1984) 89

[22] Korner R. , Ricken M., Nolting J., and Reiss I., *J. Solid Chem*., 78 (1989) 136

[23] Sorenson O. T. (ed.)., Non-Stoichiometric Oxides, Academic Press, New York, (1981)

[24] Laachir A., Perichon V., Badri A., Lamotte J., *J. Chem. Soc*. Faraday Trans., 87 (1991) 1601

[25] Badri A., Lamotte J., Laachir A., Perichon V., Eur. *J. Solid State Inorg. Chem*., 28 (1991) 445

[26] Duplan J. L. and Praliand H., *Appl. Catal*., 67 (1991) 325

[27] Yao H. C., and Yao Y. F. Y., *J. Catal*. 89 **(**1984) 254

[28] Johnson M. F. L., and Mooi J., *J. Catal*. 103 (1987) 502

[29] Padeste C,, Cant N. W. and Trimm L., *Catal. Lett*. 18 (1993) 305

[30] Harrison B., Diwell A. F. and Hallett C., *Platinum Metals Rev*. 32 (1988) 73

[31] Bernal S., Blanco F., Botana J., Gatica J. M. and Perez Omil J. A. *J. Alloys Compounds* 207 (1994) 196

[32] Logan A. D. and Shelef M. *J. Mater. Res* 9 (1994) 468

[33] Mackrodt W. C., Fowles M. and Morris M. A. *Euro. Pat* 913716.5 (1991)

[34] Zamar F., Trovarelli A., de Leitenburg C. and Dolcetti G., *J. Chem. Soc., Chem Com.* (1995) 965

[35] Trovarelli A., Boaro M., Rocchini E., de Leitenburg C., Dolcetti G., *J. Alloys & Cmpds*., 323-324 (2001) 584

[36] Bowker M., *The Basis and Applications of Heterogeneous Catalysis*, Oxford Chemistry Primers #53, Oxford University Press (1998)

[37] Gandhi H. S., Piken A. G., Shelef M., Delossh R. G., *SAE 760201* (1976)

[38] Kaspar J., Fornasiero P., Graziani M., *Catal Today*, 50 (1999) 285-298

[39] Taylor K. C., in: Anderson J. R., Boudart M., Eds, *Catalysis Science & Technology*, Springer, Berlin, 5 (1984) 120

[40] Molycorp, Inc., Cerium: A Guide to its Role in Technology (1995)

[41] How They Work, www.fce.com

[42] M. Alifanti, B. Baps, N. Blangenois, J. Naud, P. Grange, B. Delmon, *Chem Mater*., 15 (2003) 395-396

[43] Trovarelli A., Zamar F., Llorca J., de Leitenburg C., Dolcetti G., Kiss J. T., *J. Catal.*, 139 (1997) 161

[44] Trovarelli A., de Leitenburg C., Dolcetti G., *Chemtech*, 27 (1997) 32

[45] Steele B. C. H., Solid State Ionics 12 (1984) 391

[46] Zhang F., Chan S-W., Spanier J. E., Apak E., Jin Q., Robinson R. D., Herman I. P., *Appl. Phys. Lett*., 80 (1) (2002) 127-129

[47] Swanson and Fuyat, *NBS Circular*, Vol. 3 (1953) 539

[48] Felsche, Naturwiss., 212 (1969) 56

[49] Wolf R. and Hoppe R., Z. Anorg. *Allg. Chim*., 61 (1985) 529

[50] Willer and Daire, *Bull. Soc. Fr. Min. Crist*., 33 (1969) 92

[51] Leger J. M., Yacoubi N. and Loriers J., *J. Solid State Chem*., 261 (1981) 36

[52] Kilbourn B. T., *J. Less-Common Metals*, 126 (1986) 101

[53] Treux T. J. at al in "*Catalysis and Automotive Pollution Control*", Elsevier, Amsterdam 77 (2) (1991) 175

[54] Breysse M., Guenin M., Claudel B., Veron J., *J. Catal*., 28 (1973) 54

[55] Yao H.C. and Yu Yao Y.F., *J. Catal*., 86 (1987) 254

[56] Diwell A. F., Rajaram R., Shaw H. A., Treux T. J., *Catalysis and Automotive Control*, 11 (1991) 139-152,

[57] Cunningham J., Cullinane D., Farrell F., O'Driscoll J. P., and Morris M. A., *J Mat. Chem.*, 5 (1995) 1027

[58] Yahiro H., Eguchi K. and Arai H., *Solid State Ionics*, 36 (1989) 71

[59] Diwell A. F., Rajaram R. R., Shaw H. A. and Treux T. *J., Cat. And Auto. Pol. Control,* 11 (1991) 139

[60] Zhang J., Kang Z. C. and Eyring L., *J. Alloys and Cmpds*., 192 (1993) 57

[61] Greenwood N. N. and Earnshaw A., *Chemistry of the Elements*, Pergamon Press, (1986)

[62] Morss L. R., *J. Phys. Chem*. 75 (1971) 392

[63] Faktor M. M. and Hanks R., *J. Inorg. Nucl. Chem*., 31 (1968) 1649-59

[64] Morss L. R., *Chem Revs*., 76 (1976) 827

[65] Chandra S., *Super Ionic Solids, Principles & Applications*. North-Holland Publishing Co., New York (1981) 101

[66] Etsell T. H. and Flengas S. N., "The Electrical Properties of Solid Oxide Electrolytes" *Chem. Rev*., 70 (1970) 339

[67] Shannon R. D. and Prewitt C. T., "Effective Ionic Radii in Oxides and Flourides", *Acta Crystallogr*., B25 (1969) 925

[68] Shannon R. D., "Revised Effective Ionic Radii and Systematic Studies of Interatomic Distances in Halides and Chalcogenides", *Acta. Crystallogr*., A32 (1976) 751

[69] Kudo T. and Obayashi H., "Oxygen Ion Conduction of the Flourite-Type $Ce_{1-x}Ln_xO_{2-x/2}$ (Ln = Lanthanide Element)", *J. Electrochem. Soc*., 126 (1979) 264

[70] Minervini L., Zacate M. O. and Grimes R. W. *Solid State Ion.* 116 (1999) 339

[71] Mamontov E. and Egami T. *J. Phys. Chem. Solids* 61 (2000) 1345

[72] Fu Q., Saltsburg H., Flytzani-Stephanopoulous M. *M. Science* 301 (2003) 935

[73] Ferna´ndez-Garcı´a, M.; Martı´nez-Arias, A.; Guerrero-Ruiz, A.; Conesa, J. C.; Soria, J. *J. Catal.*, 211 (2002) 326.

[74] Vlaic, G.; Di Monte, R.; Fornasiero, P.; Fonda, E.; Kasˇpar, J.; Graziani, M. *J. Catal*., 182 (1999) 378.

[75] Liu, W.; Wadia, C.; Flytzani-Stephanopoulos, M. *Catal. Today,* 28 (1996) 391

[76] Rodriguez, J. A.; Jirsak, T.; Freitag, A.; Hanson, J. C.; Larese, J. Z.; Chaturvedi, S. *Catal. Lett*., 62 (1999) 113

[77] Fu, Q.; Weber, A.; Flytzani-Stephanopoulos, M. *Catal. Lett*., 77 (2001) 87.

[78] Schermanz, K. in Catalysis by Ceria and Related Materials; Trovarelli, A., Ed.; World Scientific: London; Chapter 1 (2002)

[79] Hungrıa, A. B.; Martı´nez-Arias, A.; Ferna´ndez-Garcı´a, M.; Iglesias-Juez, A.; Guerrero-Ruiz, A.; Calvino, J. J.; Conesa, J. C.; Soria, *J. Chem. Mater*., 15 (2003) 4309

[80] Wang, X.; Hanson, J. C.; Rodriguez, J. A.; Iglesias-Juez, A.; Ferna´ndez-Garcı´a, M., 121 (11) (2004) 5434

[81] Bernal, S.; Blanco, G.; Cifredo, G. A.; Delgado, J. J.; Finol, D.; Gatica, J. M.; Rodrı´guez-Izquierdo, J. M.; Vidal, H. *Chem. Mater*., 14 (2002) 844.

[82] Schwarz J.A., Contescu C., Contescu A., *Chem. Rev*., 95 (1995) 477

[83] Avila D. M., Muccillo E. N. S., *Thermochimica Acta*., 256 (1995) 391

[84] Roy D. M., Roy R., *Am. Mineral*, 39 (1954) 957

[85] Roy R. J., *J. Am. Ceram. Soc*., 39 (1956) 145

[86] Roy R. J., *J. Am. Ceram. Soc*., 52 (1969) 52

[87] Hench L. L., West J. K., *Chem. Rev*., 90 (1990) 33

[88] Yoldas B. E., *J. Non-Cryst. Solids*, 63 (1984) 145

[89] Prassas M., Hench L. L., *Ultrastructure Processing of Ceramics, Glasses and composites*; Hench L. L., Ulrich D. R., Eds., Wiley, New York (1984)

[90] Orcel G., Hench L. L., Artaki I., Jones J., Zerda T. W., *J. Non-Cryst. Solids*, 105 (1988**)** 223

[91] Deganello F., Martorana A., *J. Solid State Chem*., 163 (2002) 527

[92] Settu T., *Ceram Int*., 26 (2000) 517

[93] Ll J. G., Ikegami J., Lee H., Mori T., *Acta Mater*. 49 (2001) 419

[94] Evans, W. J., Deming T. J., Olofsen J. M., Ziller J. W., *Inorg. Chem*. 28 (1989) 4207

[95] Djuričič B., Pickering S., *J. Euro. Ceram. Soc*., 19 (1999) 1925

[96] Muccilo E. N. S., Muccilo R., Avila D. M., *Materials Science Forum*, 299-300, (1999) 70

[97] Rasmussen M. D., Jordan G. W., Akinc M., Hunyer O. Jr., Berard M. F., *Ceram. Intern*., 9 (1983) 59

[98] Vidmar, P.; Fornasiero, P.; Kašpar, J.; Gubitosa, G.; Graziani, M.; *J. Catal.*, 171 (1997) 160

[99] Bensale, A.; Bozon-Verduraz, F.; Delamar, M.; Bugli, G.; *Appl. Catal. A: General,* 121 (1995) 81

[100] Rocchini, E.; Trovareli, A.; Llorca, J.; Graham, G.W.; Weber, W.H.; Maciejewski, M.; Baiker, A.; *J. Catal.*, 194 (2000) 461

[101] Zamar, F.; Trovarelli, A.; de Leitenburg, C.; Dolcetti, G.; *Stud. Surf. Sci. Catal.*, 101 (1996) 1283

[102] Pijolat, M.; Prin, M.; Soustelle, M.; Touret, O.; Nortier, P.; J. *Chem. Soc.*, 91 (1995) 3941

[103] Duh, J.G.; Dai, H.T.; Chiou, B.S.; *J. Am. Ceram. Soc.*, 71 (1988) 813

[104] Langford J. I., Louer D., *Powder diffraction, Rep. Prog. Phys*., 59 (1996) 131-234

[105] JCPDS International Centre for Diffraction Data – Powder diffraction files

[106] Kisi E. H., *Materials Forum*, 18 (1994) 135

[107] Rietveld H. M., *J. Appl. Crystallogr*., 2 (1969) 65

[108 ] Alov, N.V., Fifty Years of X-Ray photoelectron spectroscopy, *Journal of Analytical Chemistry*, 60 (3) (2005) 297-300

[109] Annotated Handbooks of Monochromatic XPS Spectra, PDF of Volumes 1 and 2, Crist B. V., published by XPS International LLC, (2005), Mountain View, CA, USA Handbooks of Monochromatic XPS Spectra, Volumes 1-5, Crist B. V., published by XPS International LLC, (2004), Mountain View, CA, USA http://en.wikipedia.org/wiki/X-ray_photoelectron_spectroscopy

[110] http://www.eaglabs.com/documents/analytical-resolution-versus-detection-limit-BR004.pdf

[111] Chescoe D., Goodhew P.J., *The operation of transmission and scanning electron microscopes*, No. 20, Royal Microscopical society microscopy handbooks, Oxford University Press, (1990)

[112] Gareth T., Goringe M. J., *Transmission electron microscopy of materials*, John Wiley & Sons, New York, (1979)

[113] Fryer J. R., *The chemical applications of Transmission Electron Microscopy*, Academic Press Inc., New York, (1979)

[114] Thomas G., *The Impact of Electron Microscope on Materials Research*, Rickerby D.G., Valdre G., Eds., Klucuer, (1999)

[115] Tucker P. A., Rochow T. G., *Introduction to microscopy by means of light, electrons, X-Rays or acoustics*, 2nd Edition, Plenum Press, N.Y. & London (1994)

[116] Sing, K.S.W., *Reporting Physisorption Data for Gas Solid Systems - with Special Reference to the Determination of Surface-Area and Porosity*. *Pure and Applied Chemistry*, 54(11) (1982) 2201

[117] Brunauer, S., Emmett P. H., and Teller E., *Adsorption of gases in multimolecular layers*, *Journal of the American Chemical Society*, 60(2) (1938) 309

[118] Barrett, E.P., Joyner L. G., and Halenda P. P., *The Determination of Pore Volume and Area Distributions in Porous Substances .1. Computations from*

*Nitrogen Isotherms, Journal of the American Chemical Society*, 73(1) (1951) 373

[119] Trovarelli A., de Leiterburg C., Boaro M. and Dolcetti G., *Catal. Today* 50 (1999) 353 and references therein

[120] Waller D., Lane J. A., Kilner J. A. and Steele B. C. H., *Solid State Ion*. 86 (1996) 767 and references therein

[121] Stefanik T. S. and Tuller H. L., *J. Eur. Ceram.* Soc. 21 (1967)

[122] Tsoga A., Gupta A., Naoumidis A. and Nikolopoulos P., *Acta. Mater*. 48 (2000) 4709

[123] Fornasiero P., di Monte R., Rao G. R., Kaspan J., Meriani S., Trovarelli A., Grazizni M., *J. Catal.* 151 (1995) 168

[124] Mirervini L., Zacate M. O., Grimes R. W., *Solid State Ion*. 116 (1999) 339

[125] Mamonto E., Egami T., *J. Phys. Chem. Solids* 61 (2000) 1345

[126] Mays C. W., Vermaak J. S., Kuhlmann-Wilsdorf D., *Surf. Sci.* 12 (1968) 134

[127] Tsunekawa S., Sahara R., Kawazoe Y., Ishikawa K., *Appl. Surf. Sci*. 152 (1999) 53; Tsunekawa S., Ishikawa K., Li Z. Q., Kawazoe Y., Kasuya Y., *Phys. Rev. Lett*. 85 (2000) 3440

[128] Wycoff R. W. G., *Crystal Structures*, 2nd Ed., Vol 1, Interscience Publishers, New York, (1963)

[129] Bertaux S., Reynders P., Heintz J. M., Thin Solid Films, 473 (2005) 80

[130] Ghosh S., Damodaran D., Kottayilpadi C. Sreeremya R. & T. S., Journal of Nanoparticle Research 12 (5) (2010) 1905

[131] Liu X., Zhou K., Wang L., Wang B., Li Y., *J. Am. Chem. Soc*., 131 (9) (2009) 3140

[132] Tsunekawa S., Fukuda T. , Kasuya A., *J. Appl. Phys*. 87 (2000) 1318

[133] Trovarelli A., Leitenburg C., Boaro M., Dolcetti G., *Catal. Today*, 50 (1999) 353

[134] Spanier J., Robinson R., Zhang F., Chan S., Herman I., *Physical Review B*, 64, (2001) 245407-1.

[135] Tsunekawa S., Sahara R., Kawazoe Y., Kasuya A., *Mater. Trans*., 41 (2000) 1104

[136] Bekyarova E., Fornasiero P., Kaspar J., Graziani M., *Catal. Today*, 45 (1998) 179

[137] Yahiro H., Baba Y., Eguchi K., Arai H., *J. Electrochem. Soc*., 135 (1988) 2077

[138] Izu N., Shin W., Murayama N., Kanaki S., *Sensor. Actuat. B- Chem*., 87 (2002) 95

[139] Chen L., Fleming P., Morris V., et al., *J. Phys. Chem. C*, 114 (2010) 12909; D. Lyons K., Ryan M. and Morris M. A., *J. Materials Chemistry*, 12 (2002) 1207

[140] Chen L., Fleming P., Morris V., et al., *J. Phys. Chem. C*, 114 (2010) 12909

[141] Ivanov V. K., Polezhaeva O. S., Tret'yakov Yu D., Russian Journal of General Chemistry, 80 (3) (2010) 604

[142] Chen P. and Chen I., *J. Am. Ceram. Soc*. 76 (6) (1993) 1577

[143] Chu X., Chung W. I., Schmidt L. D., *J. Am. Ceram. Soc*., 76 (1993) 2115

[144] Makishima A., Kubo H., Wada K, Kitami Y., Shimohira T., *J. Am. Ceram. Soc.*, 69 (1986) c.127

[145] Dong X., Hong G., Yu D., J. Mater. Sci. Technol., 13 (1997) 113-116

[146] Masui T., Fujiwara K., Machida K. I., Adachi G. Y., Chem. Mater., 9 (1997) 2197

[147] Hsu W. P., L. Ronnquist, E. Matijevic, *Langmuir*, 4 (1988) 31

[148] Djuricic B., Pickering S., *J. Eur. Ceram. Soc.*, 19 (1999) 1925

[149] Zhou X. D., Huebner W., Anderson H. U., *Appl. Phys Lett*., 80 (2002) 814

[150] Zhou X. D., Huebner W., Anderson H. U., *Appl. Phys Lett*., 80 (2002) 814

[151] Hassanzadeh-Tabrizi S. A., Mazahere M., Aminzare M. and Sadrnezhaad S. K., *J Alloys and Compounds*, 491 (2010) 499

[152] Jalilpour M., Fathalilou M., International Journal of the Physical Sciences 7 (2012) 944

[153] Fleming P.G., Holmes J. D., Otway D. J., et al, *Journal of Solid State Chemistry* 184 (2011) 2595

[154] Taniguchi T., Katsumata K. –I., Omata S. et al, *Cryst. Growth Des*. 11, (2011) 3754

[155] Fleming P.G., Holmes J. D., Otway D. J., et al, *Journal of Solid State Chemistry* 184 (2011) 2595

[156] Taniguchi T., Katsumata K. –I., Omata S. et al, *Cryst. Growth Des*. 11, (2011) 3754

[157] Zhou X. D., Huebner W. , Anderson H. U., Chem. Mater., 15 (2) (2003) 378

[158] Wycoff R. W. G., Crystal Structures, 2nd Ed., Vol 1, Interscience Publishers, New York, (1963)

[159] Rouquerol J., Avnir D., Fairbridge C. W. et al, "Recommendations for the characterization of porous solids", *Pure and Applied Chemistry* 66, (1994) 1739

[160] Wang Z. Lin, and Feng X., *J. Phys. Chem. B*, 107 (2003) 13563

[161] Mai H-X., Sun L-D., Zhang Y-W., Si R., Feng W., Zhang H-P., Liu H-C. and Yan C-H., *J Phys. Chem., B* 109 (2005) 24385

[162] Wang Z. L., "Transmission electron microscopy of shape-controlled nanocrystals and their assemblies", *J. Phys. Chem. B,* 104 (2000) 1153

[163] Zhang J., Ohara S., Umetsu M., Naka T., Hatakeyama Y., and Adschiri T., *Advanced Mater*., 19 (2007) 203

[164] Niesz K., Reji C., Nielson J. R., Vargas R. C. and Morse D. E., *Crystal Growth and Design,* 10 (2010) 4485

[165] O'Keefe T., Yu P., Hayes S., Williams A., O'Keefe M., 'Fundamental Evaluation of the Deposition of Cerium Oxide For Conversion Coating Applications, Office of the Dept. of Defence, DOD Corrosion Policy and Oversight, Washington, DC, 2004

[166] Dirksen J. A. and Ring T. A., *Chem. Eng. Sci*. 46 (1991) 2389

[167] Trovarelli A., *Catalysis Reviews* 38 (1996) 439-520

[168] Trovarelli A., 'Catalysis by ceria and related materials', Catalytic Science Series, Vol. 2, *World Scientific Publishing Co, Imperial College Press*, London, 2002

[169] Abe H., 'Current Status and Future of the Car Exhaust Catalyst', Quarterly Review, 39, National Institute of Science and Technology Policy, Government of Japan, 2011

[170] O'Connell M., Morris M.A., *Catalysis Today* 59 (2000) 387-393

[171] Lee S-H., Lu Z., Babu S. V., Matijević E., *J. Materials Research*, 17 (2002) 2744-2749

[172] Ghenciu A. F., *Current Opinion in Solid State and Materials Science*, 6 (2002) 389-399

[173] Swartz S. L., Matter P. H., Arkenberg G. B., Holcomband F. H., Josefik N. M., *J. of Power Sources*, 188 (2009) 515-520

[174] Smith D. M., 'The defect chemistry of metal oxides', *Oxford University Press, New York*, 2000

[175] Chen L., Fleming P., Morris V., Holmes J. D., Morris M. A., *J. Phys. Chem. C*, 114 (2010) 12909-12919

[176] Yashima M., Kobayashi S., Yasui T., *Solid State Ionics*, 177 (2006) 211-215

[177] Ryan K. M., McGrath J. P., Farrell R. A., O'Neill, W. M., Barnes C. J., Morris M. A., *J. Phys.: Condens. Matter* 15 (2003) L49-L58

[178] O'Neill W. M., Morris M.A., *Chemical Physics Letters*, 305 (1999) 389-394

[179] Harrison P. G., Creaser D. C., Wolfindale B. A., Morris M. A., *Specialist periodical Reports of The Chem. Soc., Catalysis*, 11 (1994) 326-334

[180] Morris B. C., Flavell W. R., Mackrodt W. C., Morris M. A., *Journal Mat. Chem.*, 3 (1993) 1007-1013

[181] Khartona V. V., Marquesa F. M. B., Atkinson A., *Solid State Ionics*, 174 (2004) 135-149

[182] Morris M. A., Fowles M., Mackrodt W. C., *US Patent, 'Oxidation Catalysts'*, US5567667, 1996

[183] Cotton S., 'Lanthanide and actinide chemistry', *J. Wiley and Sons, Oxford*, 2006

[184] Martínez-Arias A., Hungría A. B., Fernández-García M., Iglesias-Juez A., Conesa J. C., Mather G. C., Munuera G., *J Power Sources*, 151 (2005) 43-51

[185] Guo M., Lu J., Bi Q., Luo M., *Chem Phys Chem*., 11 (2010) 1693-1699

[186] Reddy B. M., Thrimurthulu G., Katta L., *Catal. Letts*, 141 (2011) 572-581

[187] Reddy B. M., Saikia P., Bharali P., Yamada Y., Kobayashi T., Muhler M., Grűnert W., *J. Phys. Chem. C*, 112 (2008) 16393-16399

[188] Ye F., Mori T., Ou D. R., Zou J., Drennan *J., Mater. Research Bull*., 42 (2007) 943-949

[189] Ye F., Mori T., Ou D. R., Zou J., Auchterlonie G., Drennan J., *J. Appl. Phys*., 101 (2007) 113528 (pp 1-5)

[190] Reddy B. M., Saikia P., Bharali P., Park S.-E., Muhler M., Grűnert W., *J. Phys. Chem. C*, 113 (2009) 2452-2462

[191] Reddy B. M., Thrimurthulu G., Katta L., *Chinese J. Catal*., 32 (2011) 800-806

[192] Guo M., Lu J., Wu Y., Wang Y., Luo M., *Langmuir*, 27 (2011) 3872-3877

[193] Chatzichristodoulou C., Hendriksen P. V., Hagen A., *J. Electrochem. Soc*., 157 (2010) B299-B307

[194] Wang W., Hanson J. C., Liu G., Rodriguez J. A., Iglesias-Juez A., Fernández-García M., *J. Chem. Phys*., 121 (2004) 5434-5444

[195] Fleming P., Ramirez S., Holmes J. D., Morris M. A., *Chem. Phys. Letts*., 509 (2011) 51-57

[196] Morris V. N., Farrell, R. A. Sexton A. M., Morris M. A., *J. Phys.: Conf. Ser*., 26 (2006) 119-122

[197] Fleming P. G., Holmes J. D., Otway D. J., Morris M. A., *J. Solid State Chemistry*, 184 (2011) 2595-2600

[198] Gruen D. M., Koehler W. C., Katz J. J., *J. Amer. Chem. Soc*., 73 (1951) 1475-1479

[199] Gutly E. D., Eyring L., *J. Amer. Chem. Soc*., 76 (1954) 5242-5247

[200] Eyring R. T., *J. Sol. State Chem*., 41 (1982) 75-79

[201] Vickery R. C., Ruben A., *Journal of Chemical Society*, (1959) 510-513

[202] Knopf K. , Waschkowski W., *Zeitschrift Physik*, A357 (1997) 297-302

[203] Tuenge R. T., Eyring R. T., *J. Solid State Chem*., 41 (1982) 75-89

[204] Pijolat M., Prin M., Soustell M., *Solid State Ionics*, 63-65 (1993) 789-793

[205] Tsunekawa S., Sahara R., Kawazoe Y., Ishikawa K., *Appl. Surf. Sci*., 152 (1999) 53-56

[206] Perrichon V., Laachir A., Bergeret G., Frety R., Tournayan L., Touret O., J. *Journal of Chemical Society, Faraday Transactions*, 90 (1994) 773-781

[207] Xu X., Saghi Z., Gay R., Möbus G., *Nanotechnology*, 18 (2007) 225501-225508

[208] Fleming P., Farrell R. A., Holmes J. D., Morris M. A., *J. Amer. Ceramic Soc*, 93 (2010) 1187-1194

[209] Burroughs P., Hamnett A., Orchard A. F., Thornton G., *J. Chem. Soc. - Dalton Trans*. (1976) 1686-1690

[210] O'Connell M., Morris M. A., *Catalysis Today*, 59 (2000) 387-393

[211] Trovarelli, A.; de Leitenburg, C.; Boaro, M.; Dolcetti, G. *Catal. Today* **1999**, *50*, 353.

[212] Treichel, H.; Frausto, R.; Srivatsan, S.; Withers, B.; Meyer, T.; Morishige, R. *J. Vac. Sci. Technol., A* **1999**, *17*, 1160.

[213] Schubert, D.; Dargusch, R.; Raitano, J.; Chan, S. W. *Biochem. Biophys. Res. Commun.* **2006**, *342*, 86

[214] Brunner, T. J.; Wick, P.; Manser, P.; Spohn, P.; Grass, R. N.; Limbach, L. K.; Bruinink, A.; Stark, W. J. *En*V*iron. Sci. Technol.* **2006**, *40*, 4374.

[215] Das, M.; Patil, S.; Bhargava, N.; Kang, J. F.; Riedel, L. M.; Seal, S.; Hickman, J. J. *Biomaterials* **2007**, *28*, 1918.

[216 ] Morris, B. C.; Flavell, W. R.; Mackrodt, W. C.; Morris, M. A. *J.*

*Mater. Chem.* **1993**, *3*, 1007

[217] Kummerle, E. A.; Heger, G. *J. Solid State Chem.* **1999**, *147*, 485.

[218] O'Neill, W. M.; Morris, M. A. *Chem. Phys. Lett.* **1999**, *305*, 389.

[219] Esch, F.; Fabris, S.; Zhou, L.; Montini, T.; Africh, C.; Fornasiero, P.; Comelli, G.; Rosei, R. *Science* **2005**, *309*, 752.

[220] Namai, Y.; Fukui, K. I.; Iwasawa, Y. *Catal. Today* **2003**, *85*, 79.

[221] Tsunekawa, S.; Ito, S.; Kawazoe, Y. *Appl. Phys. Lett.* **2004**, *85*, 3845.

[222] Tsunekawa, S.; Sivamohan, R.; Ito, S.; Kasuya, A.; Fukuda, T. *Nanostruct. Mater.* **1999**, *11*, 141.

[223] Tsunekawa, S.; Sahara, R.; Kawazoe, Y.; Ishikawa, K. *Appl. Surf. Sci.* **1999**, *152*, 53.

[224] Chen, L.; Xu, J.; Tanner, D. A.; Phelan, R.; Van der Meulen, M.; Holmes, J. D.; Morris, M. A. *Chem.*s*Eur. J.* **2009**, *15*, 440.

[225] Cullity, B. D. *Elements of x-ray Diffraction*, 2nd ed.; Addison-Wesley Publishing Co.: Reading, MA, 1978; p xii.

[226] Zhang, F.; Chan, S. W.; Spanier, J. E.; Apak, E.; Jin, Q.; Robinson, R. D.; Herman, I. P. *Appl. Phys. Lett.* **2002**, *80*, 127.

[227] Chen, H. I.; Chang, H. Y. *Ceram. Int.* **2005**, *31*, 795.

[228] Chang, H. Y.; Chen, H. I. *J. Cryst. Growth* **2005**, *283*, 457.

[229] Zhou, X. D.; Huebner, W. *Appl. Phys. Lett.* **2001**, *79*, 3512

[230] Kamruddin, M.; Ajikumar, P. K.; Nithya, R.; Tyagi, A. K.; Raj, B. *Scr. Mater.* **2004**, *50*, 417.

[231] Tok, A. I. Y.; Du, S. W.; Boey, F. Y. C.; Chong, W. K. *Mater. Sci. Eng., A* **2007**, *466*, 223

[232] Wu, L. J.; Wiesmann, H. J.; Moodenbaugh, A. R.; Klie, R. F.; Zhu, Y. M.; Welch, D. O.; Suenaga, M. *Phys. Re*V. *B* **2004**, *69*, 125415.

[233] Hailstone, R. K.; DiFrancesco, A. G.; Leong, J. G.; Allston, T. D.; Reed, K. J. *J. Phys. Chem. C* **2009**, *113*, 15155.

[234] Creaser, D. A.; Harrison, P. G.; Morris, M. A.; Wolfindale, B. A. *Catal. Lett.* **1994**, *23*, 13.

[235] Burroughs, P.; Hamnett, A.; Orchard, A. F.; Thornton, G. *J. Chem. Soc., Dalton Trans.* **1976**, 1686.

[236] Vasiliu, F.; Parvulescu, V.; Sarbu, C. *J. Mater. Sci.* **1994**, *29*, 2095

[237] Ganduglia-Pirovano, M. V.; Hofmann, A.; Sauer, J. *Surf. Sci. Rep.* **2007**, *62*, 219.

[238] Chiang, Y. M.; Lavik, E. B.; Blom, D. A. *Nanostruct. Mater.* **1997**, *9*, 633.

[239] Nolan, M.; Fearon, J. E.; Watson, G. W. *Solid State Ionics* **2006**, *177*, 3069.

[240] Xiao, W. D.; Guo, Q. L.; Wang, E. G. *Chem. Phys. Lett.* **2003**, *368*, 527.

[241] Yang, S. W.; Gao, L. *J. Am. Chem. Soc.* **2006**, *128*, 9330.

[242] Feng, X. D.; Sayle, D. C.; Wang, Z. L.; Paras, M. S.; Santora, B.; Sutorik, A. C.; Sayle, T. X. T.; Yang, Y.; Ding, Y.; Wang, X. D.; Her, Y. S. *Science* **2006**, *312*, 1504.

[243] Mamontov, E.; Egami, T.; Brezny, R.; Koranne, M.; Tyagi, S. *J. Phys. Chem. B* **2000**, *104*, 11110.

[244] Dutta, P.; Pal, S.; Seehra, M. S.; Shi, Y.; Eyring, E. M.; Ernst, R. D. *Chem. Mater.* **2006**, *18*, 5144.

[245] Zhou, G.; Shah, P. R.; Montini, T.; Fornasiero, P.; Gorte, R. J. *Surf. Sci.* **2007**, *601*, 2512.

[246] Kim, S.; Merkle, R.; Maier, J. *Surf. Sci.* **2004**, *549*, 196.

[247] Leoni, M.; Di Maggio, R.; Polizzi, S.; Scardi, P. *J. Am. Ceram. Soc.* **2004**, *87*, 1133.

[248] Paparazzo, E.; Ingo, G. M.; Zacchetti, N. *J. Vac. Sci. Technol., A* **1991**, *9*, 1416.

[249] Zhang, F.; Wang, P.; Koberstein, J.; Khalid, S.; Chan, S. W. *Surf.*

*Sci.* **2004**, *563*, 74.

[250] Paparazzo, E. *Surf. Sci.* **1990**, *234*, L253.

[251] Ramaker, D. E.; White, C. T.; Murday, J. S. *J. Vac. Sci. Technol.* **1981**, *18*, 748.

[252] Nakano, T.; Kotani, A.; Parlebas, J. C. *J. Phys. Soc. Jpn.* **1987**, *56*, 2201.

[253] Iijima, Y.; Muramoto, K.; Uemura, M.; Hiraoka, K. *Jpn J. Appl. Phys.* **1993**, *32*, 5080.

[254] Hirano, M.; Kato, E. *J. Am. Ceram. Soc.* **1996**, *79*, 777.

[255] Chen, P. L.; Chen, I. W. *J. Am. Ceram. Soc.* **1993**, *76*, 1577.

[256] Hirano, M.; Inagaki, M. *J. Mater. Chem.* **2000**, *10*, 473.

[257] Djuricic, B.; Pickering, S. *J. Eur. Ceram. Soc.* **1999**, *19*, 1925.

[258] Zhou, X. D.; Huebner, W.; Anderson, H. U. *Appl. Phys. Lett.* **2002**, *80*, 3814.

[259] Balasubramanian, M.; Melendres, C. A.; Mansour, A. N. *Thin Solid Films* **1999**, *347*, 178.

[260] Li, Y. X.; Zhou, X. Z.; Wang, Y.; You, X. Z. *Mater. Lett.* **2004**, *58*, 245.

[261] Xu, J. H.; Harmer, J.; Li, G. Q.; Chapman, T.; Collier, P.; Longworth, S.; Tsang, S. C. *Chem. Commun.* **2010**, 1887.

[262] Nolan, M.; Grigoleit, S.; Sayle, D. C.; Parker, S. C.; Watson, G. W. *Surf. Sci.* **2005**, *576*, 217.

[263] Baudin, M.; Wojcik, M.; Hermansson, K. *Surf. Sci.* **2000**, *468*, 51.

[264] Huang, Z. X.; Thomson, P.; Di, S. L. *J. Phys. Chem. Solids* **2007**, *68*, 530.

[265] Loschen, C.; Bromley, S. T.; Neyman, K. M.; Illas, F. *J. Phys. Chem. C* **2007**, *111*, 10142.

[266] T O'Keefe, P Yu, S Hayes, A Williams, M O'Keefe, 'Fundamental Evaluation of the Deposition of Cerium Oxide For Conversion Coating Applications, Office of the Dept. of Defence, DOD Corrosion Policy and Oversight, Washington, DC, 2004

[267] J A Dirksen and T A Ring, *Chem. Eng. Sci*. 46 (1991) 2389

[268] O'Connell M., Morris M. A., *Catalysis Today*, 59 (2000) 387-393